BASIC PROCESSES
OF
PLASMA PROPULSION

Herbert O. Schrade

Institut für Raumfahrtsysteme

Universität Stuttgart

Pfaffenwaldring 31

UNIVERSITÄT STUTTGART
INSTITUT FÜR RAUMFAHRTSYSTEME

IRS

Direktor: Prof. Dr. Ernst Messerschmid
Pfaffenwaldring 31 · 7000 Stuttgart 80 · Tel. (07 11) 6 85 23 75

BASIC PROCESSES
OF
PLASMA PROPULSION

Herbert O. Schrade

Institut für Raumfahrtsysteme

Universität Stuttgart

Pfaffenwaldring 31

D-7000 Stuttgart 80

Federal Republic of Germany

August 1987

ANNUAL
~~Interim~~ Scientific Report

for period covering 1 August 1986 – 31 July 1987

A192 117

REPORT DOCUMENTATION PAGE

Form Approved
OMB No. 0704-0188

1a REPORT SECURITY CLASSIFICATION	1b RESTRICTIVE MARKINGS
Unclassified	

2a SECURITY CLASSIFICATION AUTHORITY	3 DISTRIBUTION/AVAILABILITY OF REPORT
	Approved for public release;
2b DECLASSIFICATION/DOWNGRADING SCHEDULE	distribution is unlimited

4 PERFORMING ORGANIZATION REPORT NUMBER(S)	5 MONITORING ORGANIZATION REPORT NUMBER(S)
	AFOSR·TR· 88-0135

6a NAME OF PERFORMING ORGANIZATION	6b. OFFICE SYMBOL (If applicable)	7a. NAME OF MONITORING ORGANIZATION
Institut für Raumfahrtsysteme Universität Stuttgart		AFOSR/NA

6c ADDRESS (City, State, and ZIP Code)	7b. ADDRESS (City, State, and ZIP Code)
Pfaffenwaldring 31 7000 Stuttgart 80 West Germany	Building 410, Bolling AFB DC 20332-6448

8a NAME OF FUNDING/SPONSORING ORGANIZATION	8b OFFICE SYMBOL (If applicable)	9 PROCUREMENT INSTRUMENT IDENTIFICATION NUMBER
AFOSR/NA		AFOSR-86 0337

8c ADDRESS (City, State, and ZIP Code)	10 SOURCE OF FUNDING NUMBERS			
Building 410, Bolling AFB DC 20332-6448	PROGRAM ELEMENT NO. 61102F	PROJECT NO. 2308	TASK NO. A1	WORK UNIT ACCESSION NO.

11 TITLE (Include Security Classification)
(U) Basic Processes of Plasma Propulsion

12. PERSONAL AUTHOR(S) Herbert O. Schrade

13a. TYPE OF REPORT	13b. TIME COVERED	14. DATE OF REPORT (Year, Month, Day)	15. PAGE COUNT
Interim Scientific Rep.	FROM 1 Aug86 TO 31 Jul87	1 Sept 1987 Aug	55

16 SUPPLEMENTARY NOTATION

17. COSATI CODES			18. SUBJECT TERMS (Continue on reverse if necessary and identify by block number)
FIELD	GROUP	SUB-GROUP	Magnetoplasmadynamic Thruster, Electrode Phenomena, Flow Arc Discharge, Calculations, Onset.

19. ABSTRACT (Continue on reverse if necessary and identify by block number)

This report describes the research work on cathode phenomena and presents the development work and the results of several model calculations by means of which the performance of coaxial MPD thrusters can be predicted.
(cont. on reverse)

20. DISTRIBUTION/AVAILABILITY OF ABSTRACT	21. ABSTRACT SECURITY CLASSIFICATION
☒ UNCLASSIFIED/UNLIMITED ☒ SAME AS RPT. ☐ DTIC USERS	Unclassified

22a. NAME OF RESPONSIBLE INDIVIDUAL	22b. TELEPHONE (Include Area Code)	22c. OFFICE SYMBOL
Dr Mitat Birkan	(202) 767-4937	AFOSR/NA

DD Form 1473, JUN 86   Previous editions are obsolete.

Electrode effects like spot formation and spot motion can cause high erosion on the cathode and backplate of an MPD thruster. These effects are qualitatively and partially quantitatively explained by means of a unique theoretical approach. In conjunction with the theoretical work, experiments on a special electrode test apparatus are conducted in order to measure cathode erosion and to determine spot formation and motion and the attachment mode (spotty; diffuse thermionic) under various operating conditions.

Several numerical model calculations were developed which allow to determine the flow arc discharge region and the performance (thrust and specific impulse) of a nozzle type and a cylindrical MPD thruster as a function of mass flow rate and electric current. For the nozzle type thruster the heat flux at the nozzle throat was calculated for various currents and compared with experimental measurements.

By means of these performance calculations the onset conditions were calculated based on the fact that due to magnetic contraction (pinch effect) the plasma density becomes zero at the anode (onset theory of Hügel). The results of these calculations are in excellent agreement with those of the experiments.

Preface

The work described in this interim scientific report has been partially sponsored by the Air Force Office of Scientific Research through the European Office of Aerospace Research and Development, London, under Grant AFOSR 86-0337. The period covered herein is from 1 August 1986 to 31 July 1987.

Table of Contents

1. Summary

The objectives of this work are to investigate the still unknown effects on electrodes and to determine the acceleration mechanism and the stability behavior within the flow arc discharge region of a cylindrical and a nozzle-type MPD accelerator.

Electrode effects like spot formation and spot motion can cause high erosion on the cathode and backplate of an MPD thruster. These effects are qualitatively and partially quantitatively explained by means of a unique theoretical approach. In conjunction with the theoretical work, experiments on a special electrode test apparatus are conducted in order to measure cathode erosion and to determine spot formation and motion and the attachment mode (spotty; diffuse thermionic) under various operating conditions.

Several numerical model calculations were developed which allow to determine the flow arc discharge region and the performance (thrust and specific impulse) of a nozzle type and a cylindrical MPD thruster as a function of mass flow rate and electric current. For the nozzle type thruster the heat flux at the nozzle throat was calculated for various currents and compared with experimental measurements.

By means of these performance calculations the onset conditions were calculated based on the fact that due to magnetic contraction (pinch effect) the plasma density becomes zero at the anode (onset theory of Hügel). The results of these calculations are in excellent agreement with those of the experiments.

2. Electrode Investigation

2.1 General Remarks

The cathode attachment of an arc is either spotty and governed by field emission or (seemingly) diffuse and explainable by thermionic emission. While the first, spotty mechanism occurs on cold cathode surfaces of pulsed MPD thruster devices and during the starting phase of continuously running devices, the thermionic mode prevails when the cathode surface is extremely hot, i.e. reaches temperatures above at least 2000° K. In order to sustain such temperatures the cathode material must be of a highly refractory metal like tungsten or, what works best so far, an alloy of thoriated tungsten (2% ThO_2). Since the thorium oxide melts at about 200° K below the tungsten melting point and any stable, spotty discharge requires a molten, even evaporating area, one may conclude that also at so-called thermionically emitting cathodes many microspots are present which are highly nonstationary and evenly distributed over a larger hot surface. This conception is also in agreement with measured erosion rates of both attachment modes, both of which may be explained by one and the same spot mechanism:[1]   a) the diffuse attachment area which consists of many evenly distributed and highly nonstationary microspots, each of which carries a low current of a few tens of amperes and b) a typical spotty attachment presented by one or several hot spots, each of which has currents up to the tens and even hundreds of amperes. These latter bigger spots are likely the result of clustered microspots which are somehow hindered in spreading over a larger cathode area. One goal of this investigation was to understand and to predict the motion and behavior of these spots. It was shown[1] that the overall erosion rate of a cathode does depend on the spot current and not necessarily on the overall total current. It would therefore be advantageous to have many microspots, each carrying only a small current and all spread over a large area, than to have only one or a few larger ones (or many clustered smaller ones which stick together and build one or a few large spot sites) of fairly large currents.

[1] H. O. Schrade, M. Auweter-Kurtz and H. L. Kurtz, "Cathode Erosion Studies on MPD Thrusters", 18th International Electric Propulsion Conference, AIAA-85-2019, Alexandria, VA, 1985

2.2 Theory

Any active arc spot may be characterized by a crater-like pit with an inner molten layer, above which is located a high pressure plasma cloud. This high pressure plasma cloud, caused by ohmic heating and heavy evaporation of the electron emitting inner surface layer, expands out into the ambient lower pressure gas sphere and forms a plasma jet. This jet contains a current carrying channel which emanates from the high pressure plasma cloud of the crater and which electrically connects the low pressure interelectrode plasma and hence the anode with the cathode (see Fig. 1).

By means of a unique theory, the stability behavior of such a current carrying channel within an axial jet has been discussed and presented at the 19th International Electric Propulsion Conference in Colorado Springs, Colorado, May 11-13, 1987 (see Appendix II, Cathode Phenomena in Plasma Thrusters). It turns out that under certain conditions this channel becomes unstable with respect to small deviations off its straight configuration. The current carrying plasma channel then starts to bend more and more and eventually touches the cathode surface at a nearby area of the spot (see Fig. 2). This cathode surface area is heated up, melts and eventually a new spot is created.

Three cases shall be discussed: the spot discharge I) without an external magnetic field, II) with a magnetic field parallel to the cathode surface and III) in which the magnetic field is inclined with respect to the surface.

I) If no external magnetic field $\vec{B}_0$ is present, instability occurs when the dimensionless quantity

$$\varepsilon = \frac{8\pi}{\mu_0 I_s^2} \int_{A_z} \rho \, v_z^2 \, dA_z \; - \; [1 + f] \tag{1a}$$

$$\approx \frac{1}{\frac{\mu_0}{8\pi} I_s \bar{j}} (p_c - p_\infty) - 3.3 \tag{1b}$$
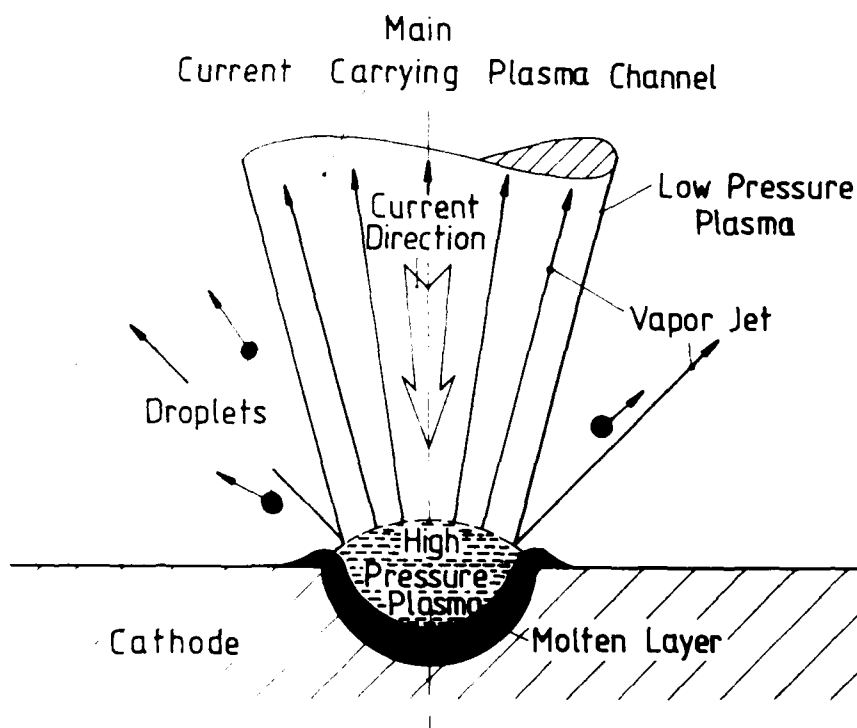
Fig. 1   Scheme of a Spot Discharge with a
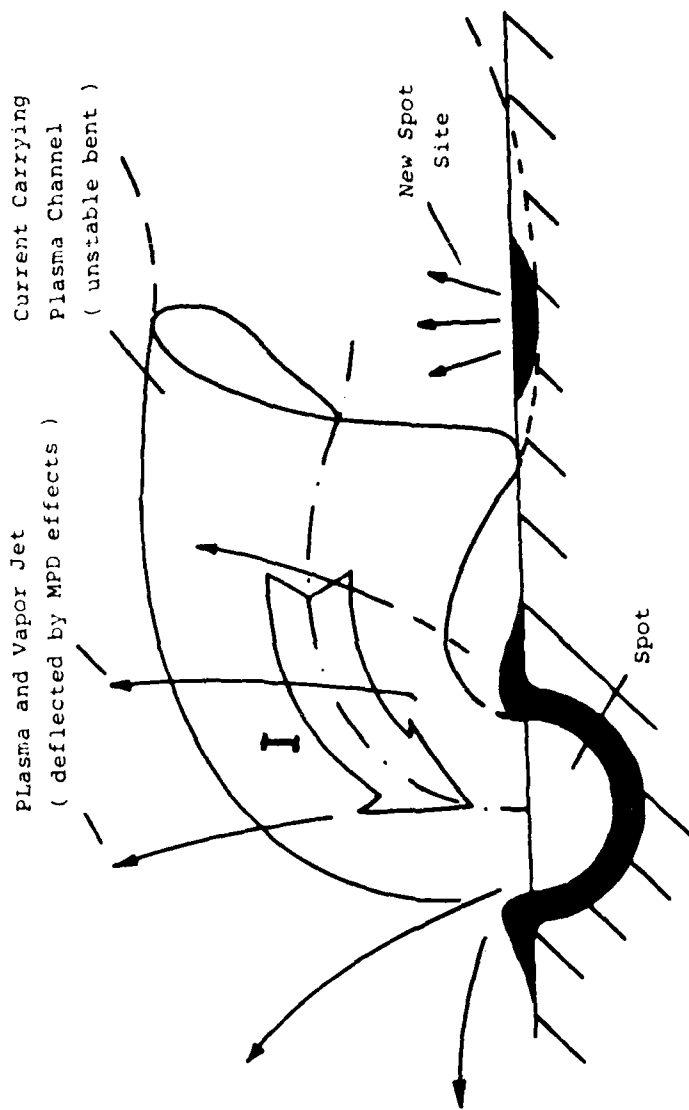   Straight Discharge Channel

- 5 -

Fig. 2   Unstable Spot Discharge

decreases below zero. Herein I_s is the current carried by the spot,
$$\int_{A_z} \rho \, v_z^2 \, dA_z$$
is the impulse transport along the channel axis and f is a factor of about 0.8 which weakly depends on the current density distribution over a cross sectional area (A_z) of the discharge channel. ϵ can also be approximated by the expression (1b) which depends on a) the pressure difference ($p_c - p_\infty$) between the high pressure (p_c) spot plasma and the ambient pressure (p_∞) (see Fig. 1) and which depends on b) the average magnetic pinch pressure
$$\frac{\mu_0}{8\pi} I_s \bar{j}$$
close to the crater orifice. The factor 3.3 is taken strictly as a slowly varying function depending on the crater shape and the current density distribution across the channel cross section just above the crater orifice; it can be well approximated by 3.3 ($\pm$ 15%). (See Appendix I.)

In order to keep the spot current down and hence the erosion rate, one therefore should try to get a spot unstable before it reaches a high current rate. According to our results this occurs earlier when the ambient pressure p_∞ (see eq. (1b) for ϵ) is larger than when it is smaller, which agrees with certain experimental findings (see below).

II) If a magnetic field parallel to the cathode surface is applied, one must distinguish between three discharge channel reactions (see Fig. 3): a) With respect to a small disturbance $\vec{\delta}$ the channel adjusts itself to one with a straight discharge axis; this reaction is called "straight stable". b) With respect to a small disturbance $\vec{\delta}$ the channel deviates even more from its original straight configuration but adjusts itself to a "curved-stable" configuration (i.e. any small deviation off this curved state would cause the channel to adjust to this curved configuration). c) With respect to a small disturbance $\vec{\delta}$ the discharge channel bends more and more and eventually touches the cathode surface at a nearby area as shown before; this last channel reaction is called "unstable".
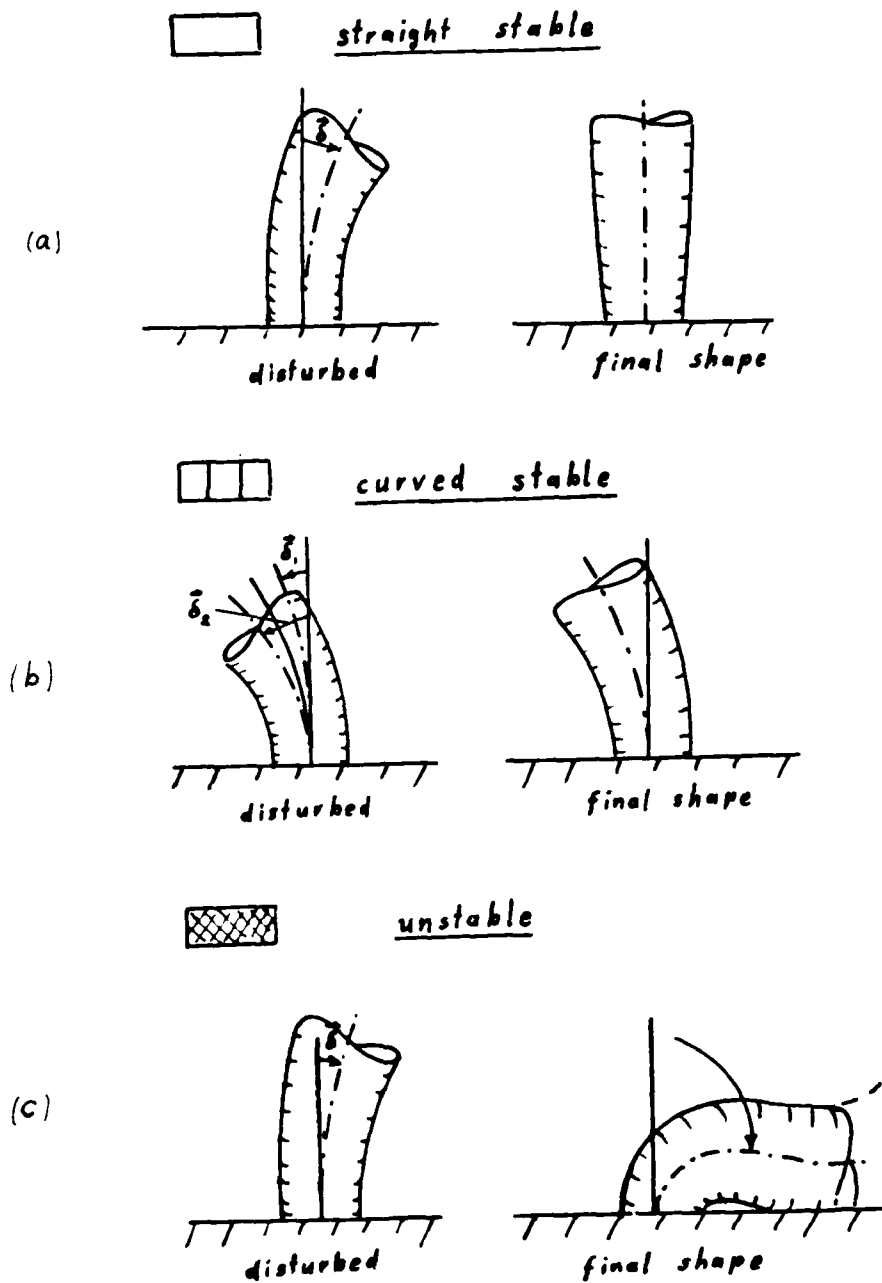
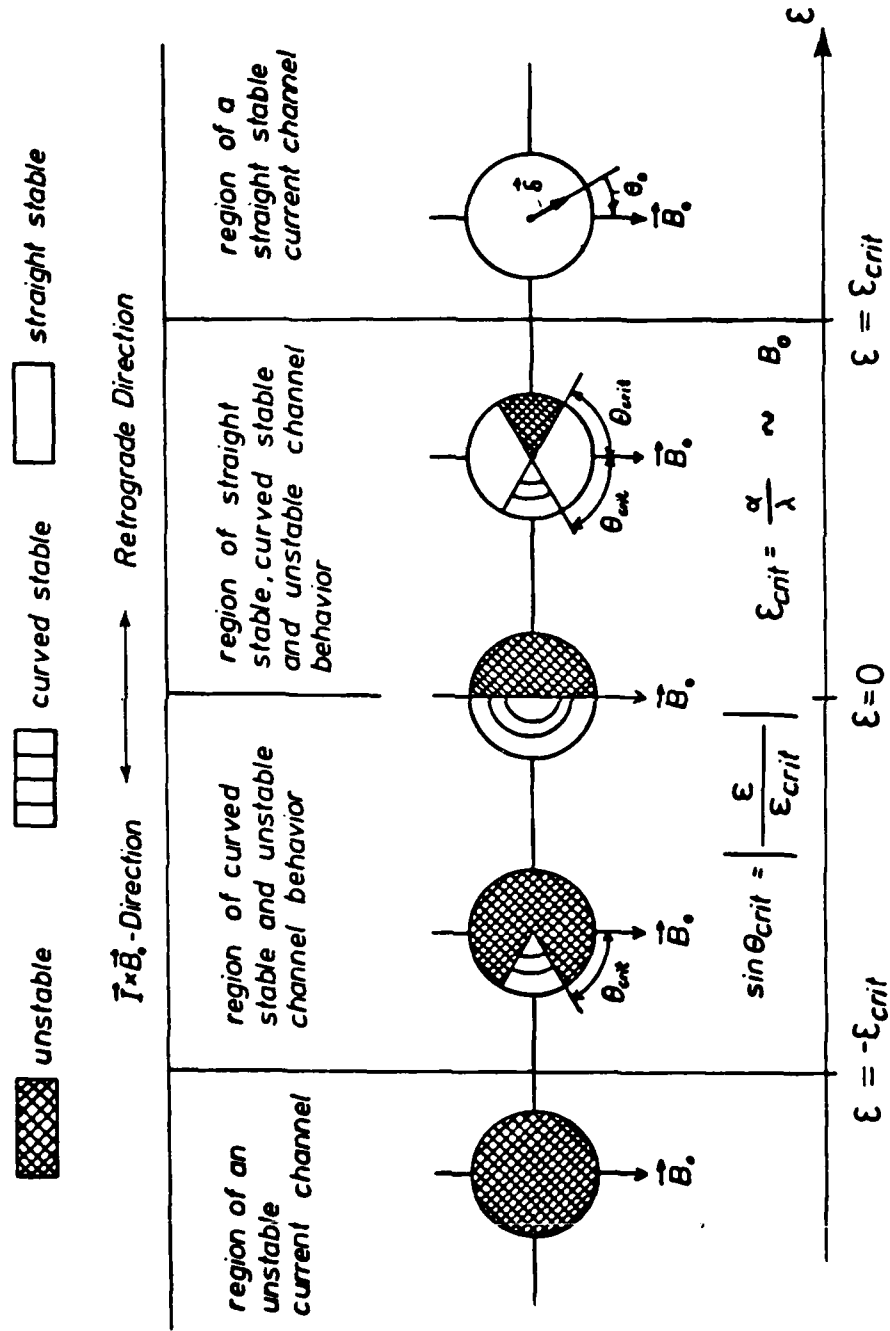Fig. 3 Possible reactions of a discharge channel with respect to a small disturbance.

Fig. 4 Stable and unstable channel behavior depending on ε and the direction of the disturbance δ⃗

Depending on the amouunt of ε given in eqs. (1a) and (1b) and on the direction of the disturbance $\vec{\delta}$, the discharge channel reaction can now vary between a) a straight stable, b) a curved stable and c) an unstable one (see Fig. 4).

$$\text{For} \qquad \varepsilon > \varepsilon_{crit} = \alpha \; \frac{8\pi}{\mu_0} \; \frac{r_0 B_0}{I_s} \qquad\qquad (2)$$

where α depends on the current density distribution (see Appendix II) and is expected to be smaller than about + 0.2, the discharge channel reaction is straight stable.

If ε falls in the range $0 < \varepsilon < +\varepsilon_{crit}$ the discharge channel can be stable, curved stable or unstable depending on the direction of the disturbance vector $\vec{\delta}$. For any small disturbance in the retrograde direction, i.e. opposite to $(\vec{j} \times \vec{B})$, the current channel is unstable; for any small disturbance in the amperian direction the channel will assume a curved stable configuration, and for disturbances parallel or anti-parallel to $\vec{B}_0$ the channel reacts in a stable fashion. The range of the azimuth angle $2\theta_{crit}$ $(-\theta_{crit} < \theta_0 < +\theta_{crit};$ where θ_0 determines the direction of the disturbance) at which the channel still reacts in a stable manner thereby decreases the more, the smaller ε becomes. Simultaneously the range in which any small disturbance leads to an unstable or curved stable channel behavior increases with decreasing ε. If ε equals zero, any small disturbance to the retrograde side leads to an unstable behavior of the discharge channel, and any disturbance to the amperian side leads to a curved stable reaction. If ε decreases further, even below zero, the angular range in which a disturbance leads to a curved stable channel behavior becomes smaller and smaller and finally ceases when ε reaches the negative critical value $-\varepsilon_{crit}$. For $\varepsilon < -\varepsilon_{crit}$ a small disturbance in any arbitrary direction causes an unstable channel reaction.

The consequence of this instability behavior of the discharge channel is the fact that when ε decreases below ε_{crit} the spots should preferably jump in the retrograde direction (see also Appendix II).

III) If the external magnetic field is inclined with respect to the cathode surface, this "retrograde spot motion" (discontinuous jumps) occurs preferably under a certain angle with respect to the retrograde direction (see Appendix II). This experimentally observed phenomenon, known as *Robson drift motion,*[2] like the phenomenon of retrograde motion is therefore explainable by one unique theoretical approach.

In a future step the behavior of the spot discharge will be considered in a magnetic field perpendicular to the surface of the cathode.

---

[2] A. E. Robson, "The Motion of an Arc in a Magnetic Field", Proceedings of the Fourth International Conference on Ionization Phenomena in Gases, Vol. IIb, p. 346, Aug. 1959

2.3 Experiment

The goal of these electrode experiments is to investigate the
cathode attachment mechanism and to determine erosion rates
under various operating conditions like cathode material, cath-
ode temperature, applied magnetic field, ambient pressure, over-
all current etc., and finally these experiments shall guide and
prove (or deny) the validity of the theory. The experimental
test rig as shown in Fig. 5 which has been explained in the
Final Scientific Report[3] served as an overall investigation on
cold and hot cathodes of different materials. The results so far
of erosion rate measurements for different materials and for
different current pulse numbers on cold cathodes are plotted in
Table 1. There is an indication that on polished surfaces the
erosion rates are slightly smaller than on unpolished ones.
After several shots of current pulses (duration 2 ms each),
however, any polished surface acquires a "sand blasted" look
which stems from a bombardment of arc spots leaving a field of
superimposed craters on the surface.

Therefore, as can be seen from Table 1, it is obvious that the
erosion rates measured between polished and unpolished materials
differ less, the higher the number of current pulses with the
same electrode sample. Interesting to note here is also the
somewhat higher erosion rate with pure tungsten than with thori-
ated tungsten electrodes.

Photomicrographs of the cathode surfaces which were exposed to
one single shot showed typical distinct craters and grooves, the
latter of which may be interpreted as an overlapping string of
craters (see Figs. 6 and 7). The main difference between both
figures is the width or size of the grooves and craters. At
higher ambient pressure (p_∞ = 0.5 mbar; see Fig. 7) the aver-
age size of the grooves (or craters) is smaller than at lower
ambient pressure (p_∞ = $5 \cdot 10^{-4}$ mbar; see Fig. 6). One also ob-
serves during the experiments that at higher pressure the arc

---

[3] H.O. Schrade, M. Auweter-Kurtz and H.L. Kurtz, "Basic Proc-
esses of Plasma Propulsion", Final Scientific Report, AFOSR
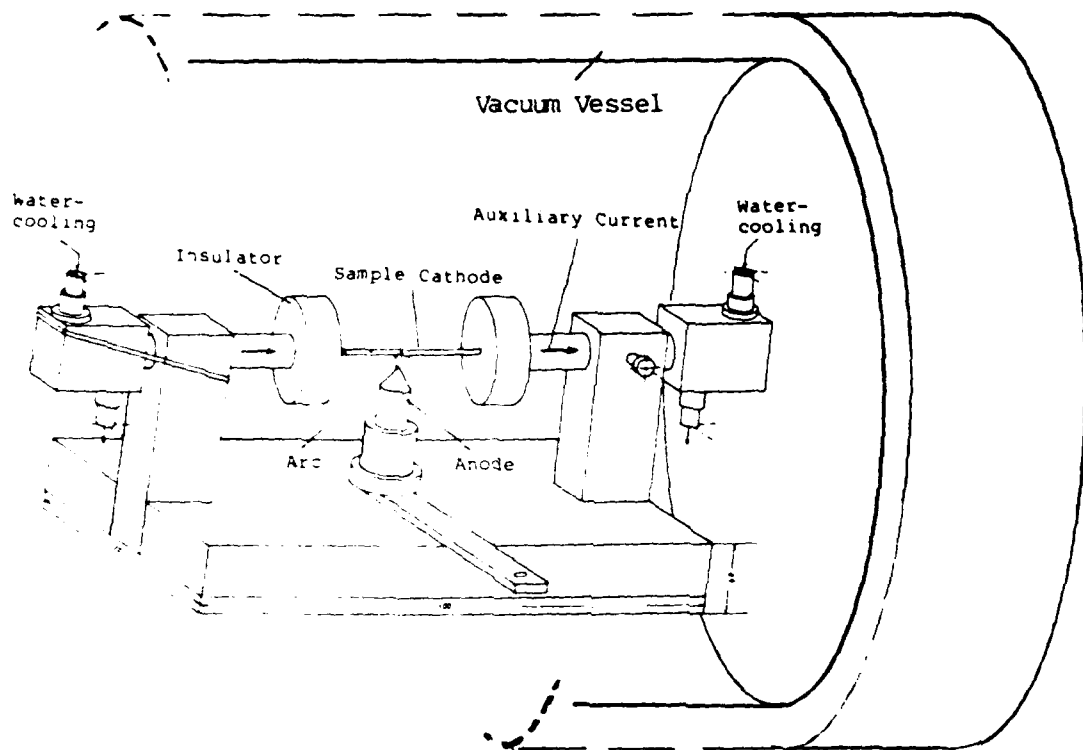Grant 82-0298, Jan. 1987

Fig. 5   Electrode Test Rig

Table 1 Erosion rates for different cathode surfaces.

	Number of Current Pulses	*Measured* Erosion Rate
Thoriated Tungsten (2% ThO$_2$) (not polished)	300 5000	35 µg/C 41 µg/C
Thoriated Tungsten (2% ThO$_2$) (polished)	100 500 6000	29 µg/C 34 µg/C 42 µg/C
Pure Tungsten (not polished)	100 500 5000	44 µg/C 50 µg/C 54 µg/C
Copper (not polished)	200 800	73 µg/C 77 µg/C
Copper (polished)	100 800	74 µg/C 75 µg/C
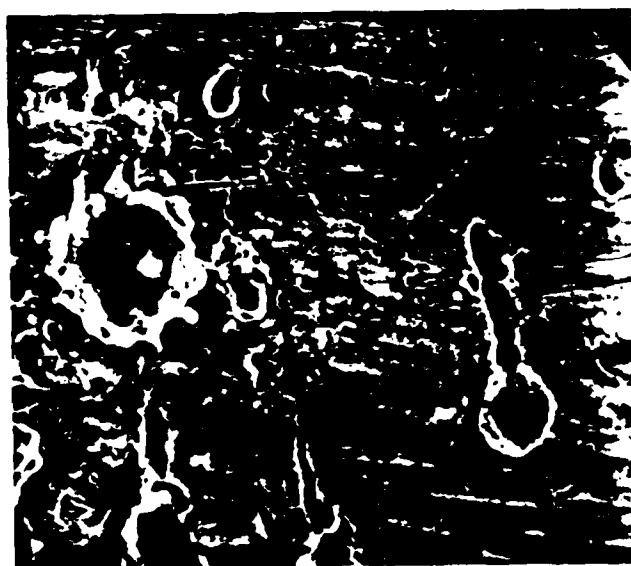
5000 : 1

2000 : 1

Fig. 6 Photomicrographs of the arc traces left on the surface of a cold thoriated tungsten cathode (rectangular current pulse I = 130 A, electric load Q = 0.26 Coul, $p_\infty = 5 \cdot 10^{-4}$ mbar).

5000 : 1

2000 : 1

Fig. 7   Photomicrographs of the arc traces left on the surface
of a cold thoriated tungsten cathode (rectangular cur-
rent pulse I = 144 A, electric load Q = 0.29 Coul,
p_∞ = 0,5 mbar).

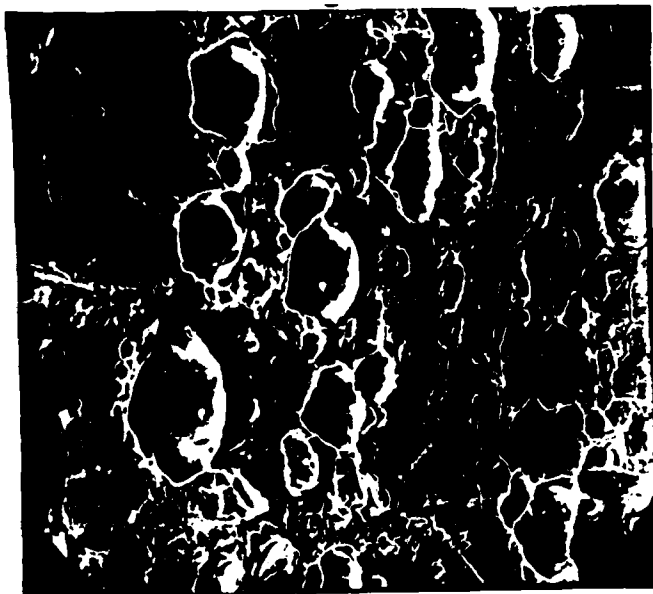1500 : 1

10000 : 1

Fig. 8 Photomicrographs of the arc traces left on the surface
of a hot thoriated tungsten cathode ($T = 2000^{\circ}$K, rectan-
gular current pulse $I = 360$ A, electric load $Q = 0.72$
As, $p_{\infty} = 5 \cdot 10^{-4}$ mbar).

spots spread more quickly from the original impact area close to the anode along the cathode rod than it is observed under the low pressure condition when the arc sticks more to the original impact area. This spot behavior is an indication that proves the theoretical result as discussed before, that at higher ambient pressure (p_∞) ε should become more quickly negative and therefore the discharge channel more quickly unstable and the spots more moveable. Nevertheless, this indication has to be checked more carefully and cannot simply be extrapolated to pressures above 10 and more mbar.

Experiments with hot cathodes again show spotty arc traces (see Fig. 8) but the craters look smoother than in the case of cold cathodes.

Reproducible and reliable erosion rate measurements on hot cathodes failed so far with the old test apparatus, despite several days of outgasing of the tank and improvements in the insulation material. Therefore a new electrode test apparatus is being designed and built.

3. MPD Thruster Performance Calculations

In order to predict MPD arc thruster performance, several model
calculations have been developed and are explained in Appendix
III, "Numerical Modeling of the Flow Discharge in MPD Thrust-
ers".[4] This paper was presented at the 19th International Elec-
tric Propulsion Conference in May 1987. The following section
therefore contains only more recent theoretical results concer-
ning the two MPD thruster types shown in Figs. 9 and 10. Both
thrusters are also experimentally tested in our institute, al-
lowing certain comparison checks between theory and experiment.

3.1 Nozzle Type Thruster

The flow discharge model calculations are based on a combination
of a steady state, one-dimensional MPD flow and a two-dimension-
al current coutour line treatment. The plasma within the nozzle
was assumed fully, singly ionized, whereby the expansion process
of the electrons was taken isothermally and that of the ions
adiabatically. Heat losses and friction were neglected. The cal-
culations were carried out for three different jet plume condi-
tions[4] as shown in Figs. 11a,b,c and 12a,b,c and for the follow-
ing two electrode conditions.

One time the electric field vector $\vec{E}$ and the other time the cur-
rent density vector $\vec{j}$ were taken perpendicularly to the elec-
trode surfaces. The results for both electrode conditions, how-
ever, differ only slightly as shown in Fig. 13a and b. Both cur-
rent contour line figures are based on the hyperbolic plume of
Fig. 11b.

The computer code for these semi-two-dimensional, steady state,
nozzle type thruster calculations were rewritten for the Cray II
computer which became available at the University of Stuttgart
about a year ago.

---

[4] H. O. Schrade, M. Auweter-Kurtz and H. L. Kurtz, "Basic
Processes of Plasma Propulsion", Final Scinetific Report, AFOSR
Grant 82-0298, Jan. 1987

insulator

neutral segments

anode

cathode

$\emptyset$ 74

$\emptyset$ 142

$\emptyset$ 14

probe outflow
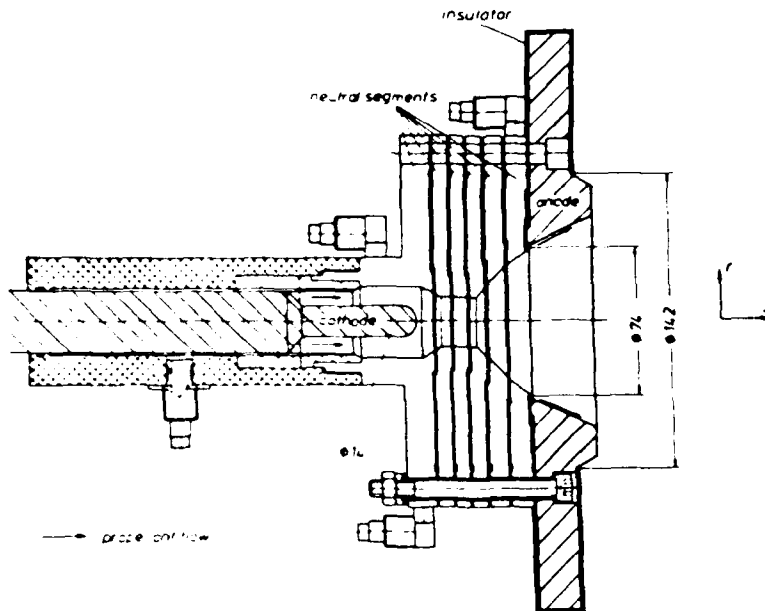
Fig. 9   SELF-FIELD NOZZLE-TYPE MPD THRUSTER DT2-IRS

Insulator | Insulator | Anode 3 | Anode 2 | Anode 1

displaceable cathode

Fig. 10   SELF-FIELD CYLINDRICAL MPD THRUSTER ZT1-IRS
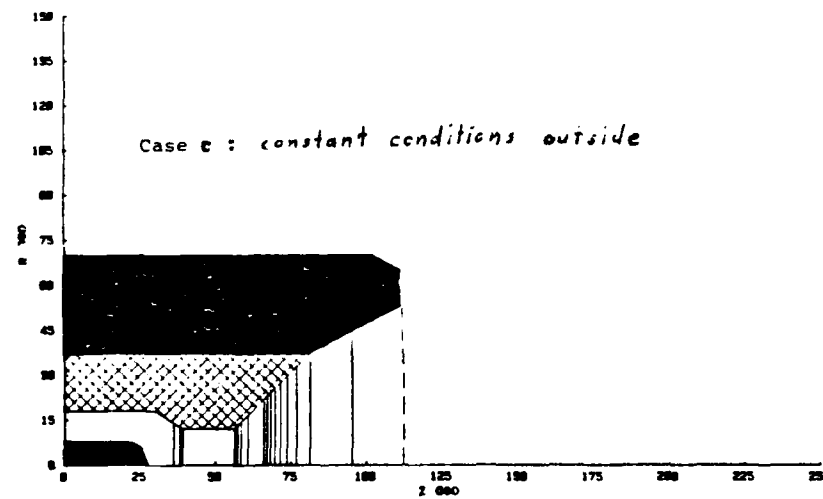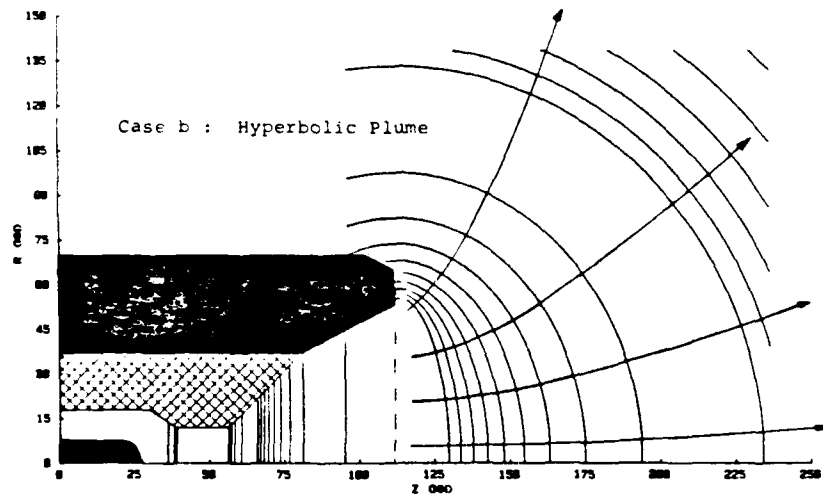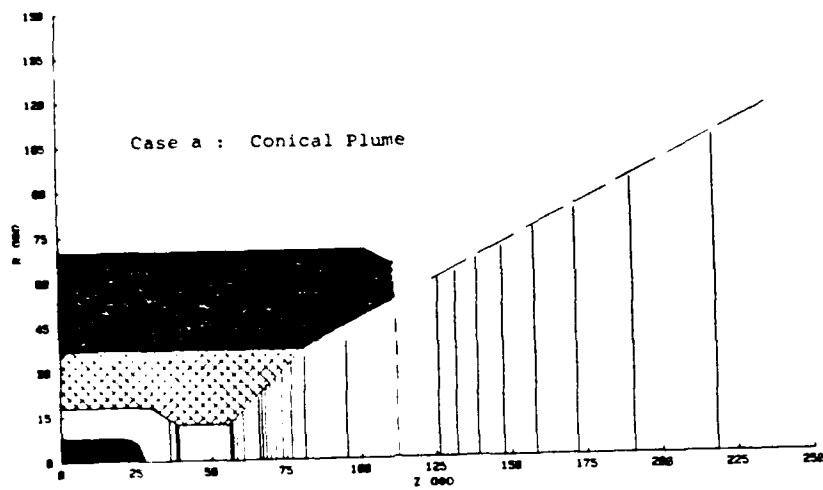
Fig. 11 Different plasma jet plume conditions.
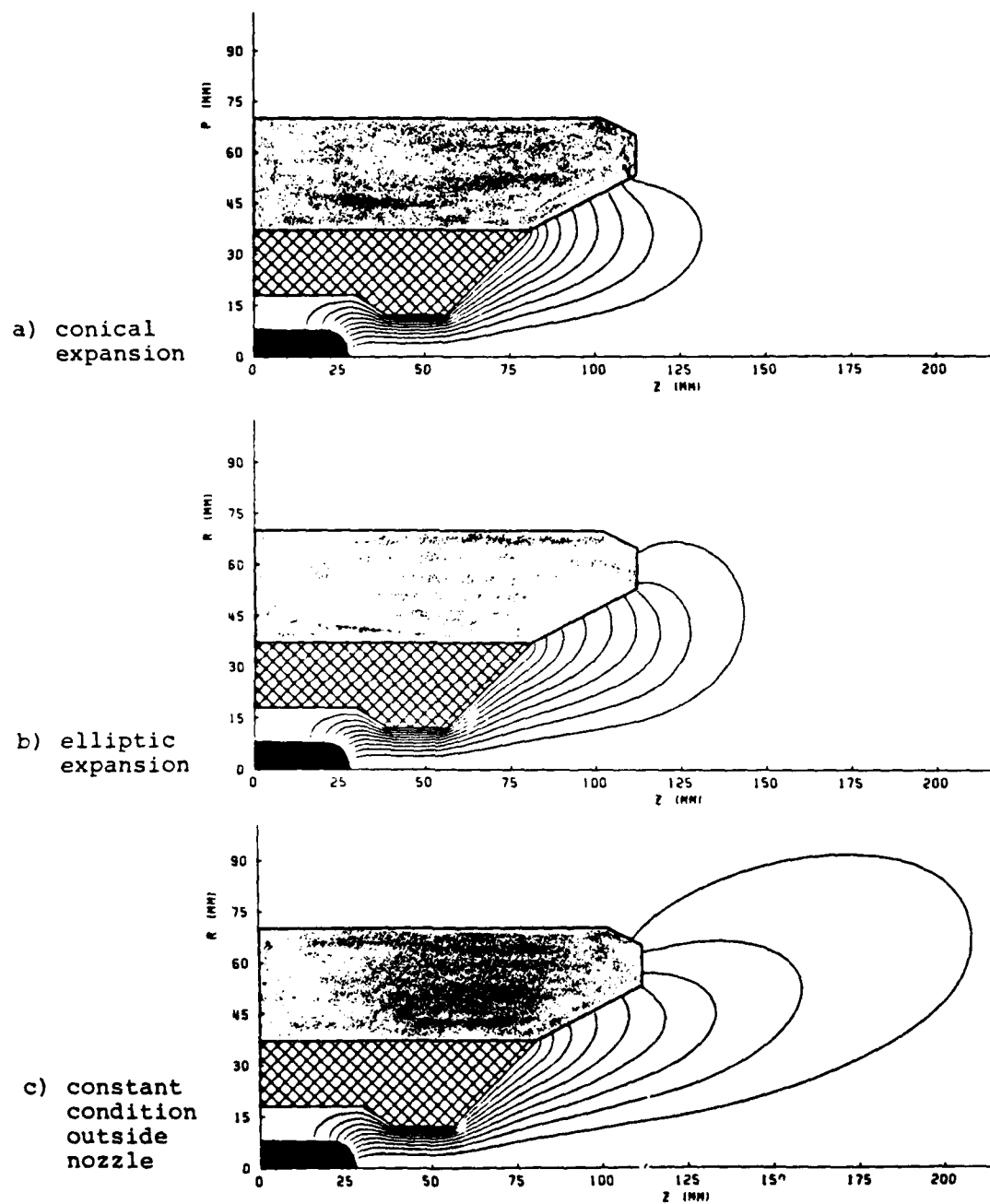
Fig. 12   current contour lines for different expansion models   (I=2000A, ṁ=0.8g/s)
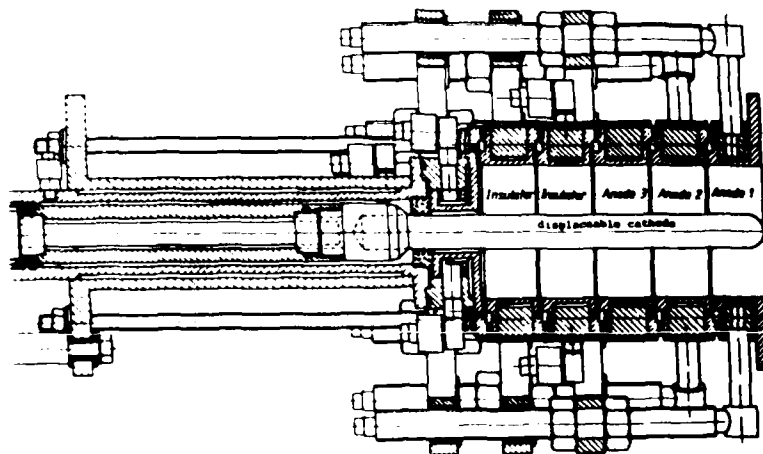
- 22 -

a) current density perpendicular to electrode surface

$\dot{m} = 0.0008$ [kg/s]
$I = 2000.$ [A]

b) electric field perpendicular to electrode surface
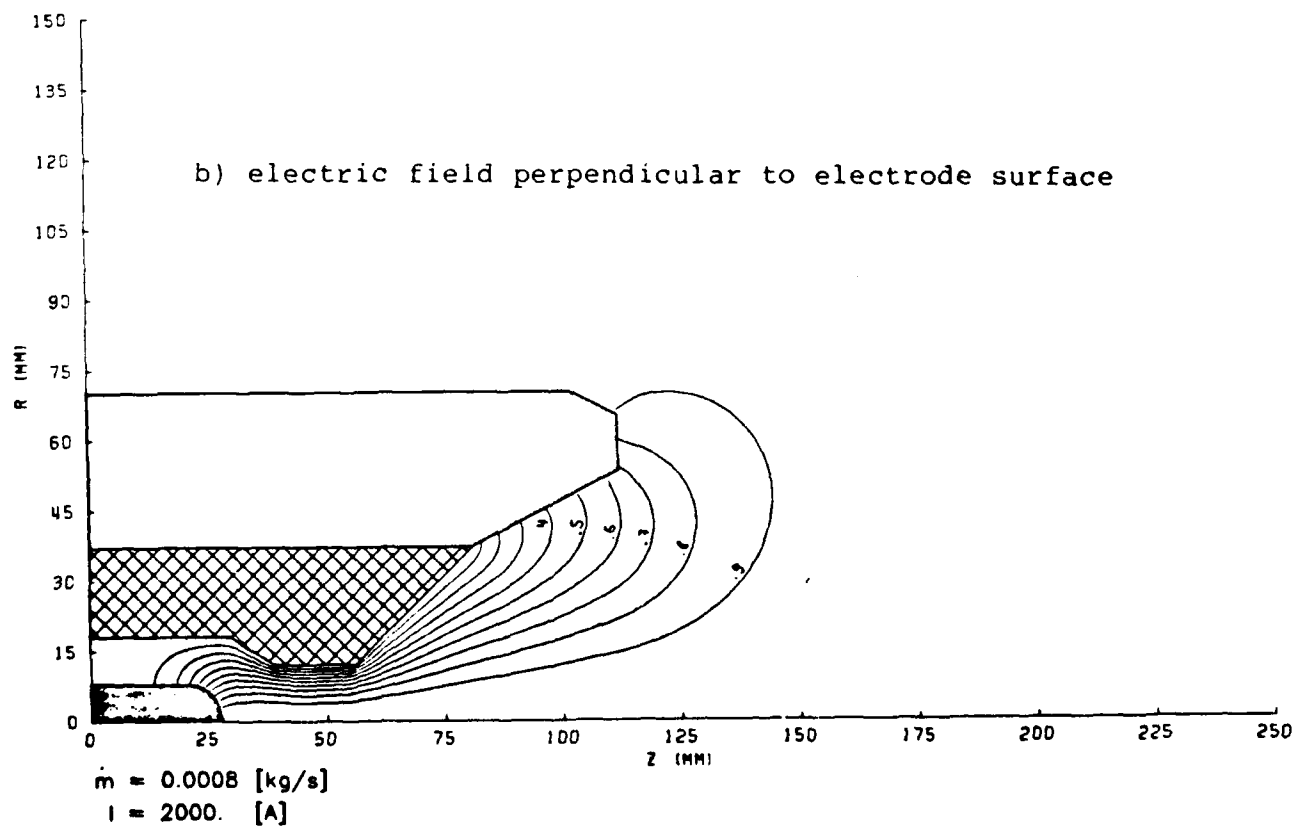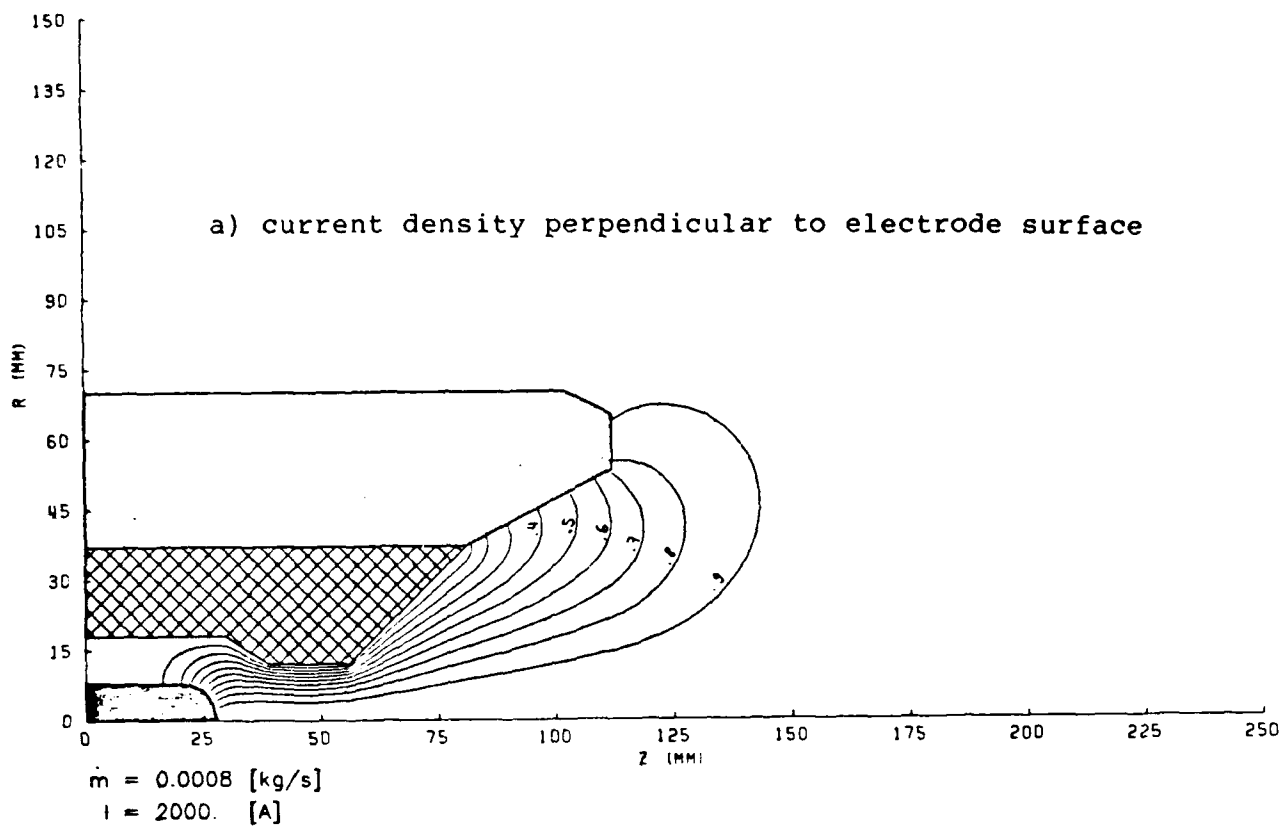
$\dot{m} = 0.0008$ [kg/s]
$I = 2000.$ [A]

Fig. 13   Current contour lines within a nozzle type thruster for
two different electrode conditions.

The nozzle throat conditions are based on the premise that the arc column fills the cross-sectional throat area and that only axial components of the velocity and current density vector are present ("fully developed arc"; see loc. cit.). Neglecting radiation and friction, the energy equation reduces then to

$$\frac{j^2}{\sigma} = - \frac{1}{r} \frac{d}{dr} \left(r \lambda \frac{dT}{dr} \right) \equiv + \frac{1}{r} \frac{d}{dr} \left(r \, q_r \right) \tag{3}$$

i.e. within the nozzle throat the radial heat conduction loss is balanced by ohmic heating. q_r is the radial heat flux vector, λ the heat conduction coefficient and σ the electric conductivity. The first integration of eq. (3) results in the heat flux per unit axis length given by

$$2 \pi r_0 \, q_r(r_0) = 2 \pi \int_0^{r_0} \frac{j^2}{\sigma} \, r \, dr \tag{4}$$

By modeling the current density distribution across the throat area (πr_0^2) through a paraboloid of grade n as

$$j = \hat{j} \left\{ 1 - \left(\frac{r}{r_0} \right)^n \right\} \tag{5}$$

where $\hat{j}$ is the current density maximum and j/σ is the voltage drop ($dU/dz = E_z$) or the electric field, one obtains, since E_z is constant over the cross sectional area of the throat and therefore also equals to $E_z = \hat{j}/\hat{\sigma}$,

$$2 \pi r_0 \, q_r(r_0) = \pi r_0^2 \frac{\hat{j}^2}{\sigma} \frac{n}{n + 2} = I \cdot E_z \tag{6}$$

Herein I is the arc current and $\hat{\sigma}$ is the maximum value of the electrical conductivity. Since for fully ionized plasmas σ can be approximated by

$$\sigma \approx \gamma \, T_e^{3/2}$$

where $\qquad \gamma \approx 1.55 \cdot 10^{-3} \left[\frac{A}{V \, m \, K^{3/2}} \right]$ [5]

[5] H. O. Schrade, M. Auweter-Kurtz and H. L. Kurtz, "Stability Problems in magneto Plasmadynamic Arc Thruster", AIAA 18th Fluid Dynamics and Plasmadynamics and Lasers Conference, AIAA-85-1633, Cincinnati, OH, July 1985

one obtains for the heat flux per unit length

$$2\pi r_0 \; q_r(r_0) = \frac{n+2}{n} \; \frac{0.65 \cdot 10^3}{T_e^{3/2}} \; \frac{I^2}{\pi r_0^2}$$

and if one replaces the maximum electron temperature by[3]

$$\hat{T}_e = 257 \; (\frac{n+4}{n})^{1/5} \; (\frac{I}{r_0})^{2/5}$$

it is

$$2\pi r_0 \; q_r(r_0) = \frac{1 + \frac{2}{n}}{(1 + \frac{4}{n})^{3/10}} \; 5.0 \cdot 10^{-2} \; (\frac{I}{r_0})^{7/5} \; [\frac{W}{m}] \qquad (7)$$

$$\equiv \frac{\dot{Q}}{l}$$

The results of the heat load measurements on the innermost seg-
ment of the nozzle throat (see Fig. 14) of the IRS DT2 thruster
with $r_0 = 1.2$ cm were now compared with that obtained by the
above equation (see Fig. 14). The agreement is very good at
higher currents ($\sim$ 4000 A) and deviates by a factor of about two
at low currents ($\sim$ 1000 A). At low currents the arc channel may
not fill the entire throat such that the radially transported
heat from the arc is partially carried away along the axis by a
cold gas layer. With increasing currents, however, the arc cross
section assumes more and more that of the throat, while the cold
gas layer diminishes and the radial heat losses of the arc col-
umn agree with the measured heat load to the inner throat walls.

---

[3] H.O. Schrade, M. Auweter-Kurtz and H.L. Kurtz, "Basic
Processes of Plasma Propulsion", Final Scientific Report, AFOSR
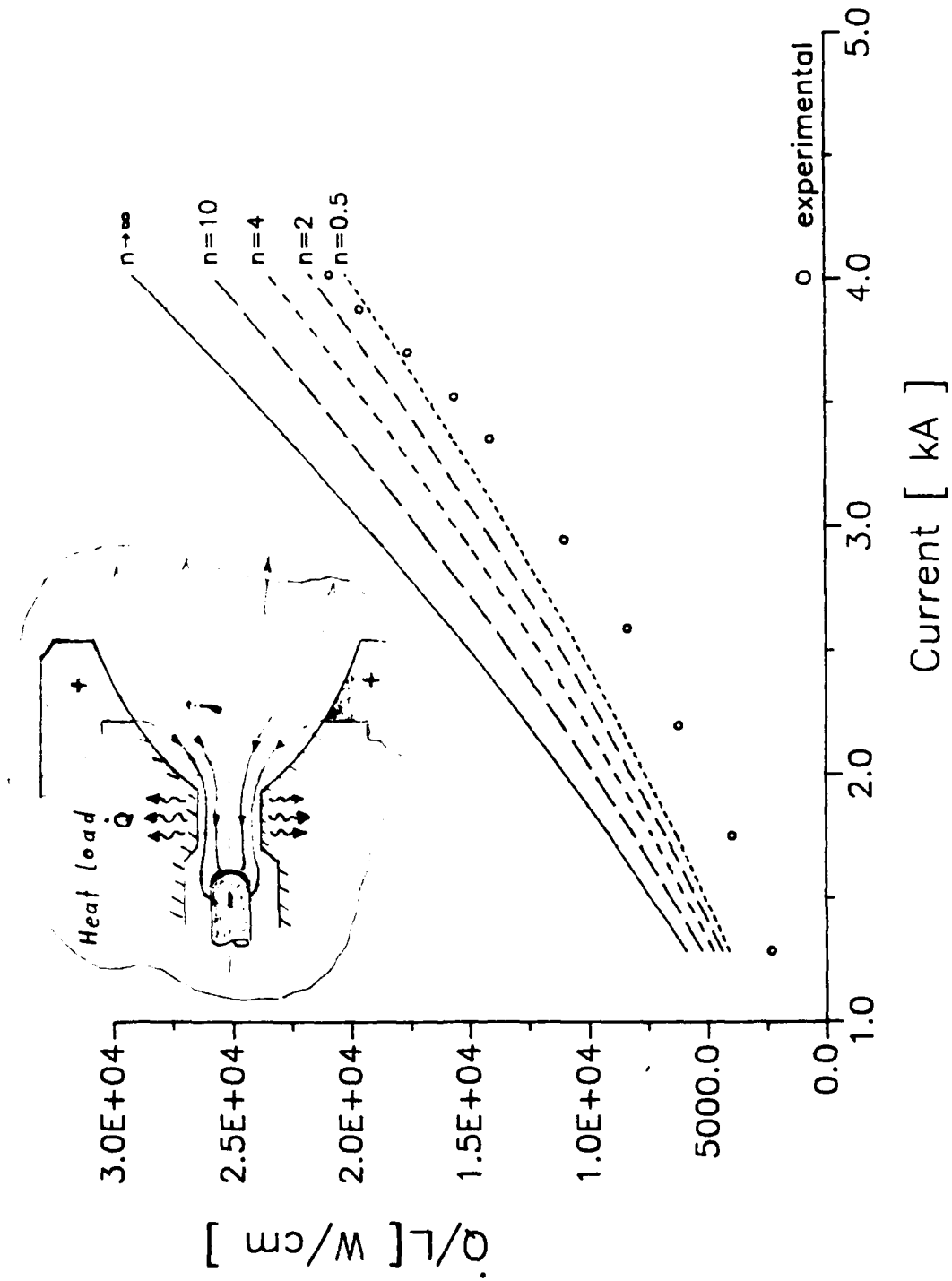Grant 82-0298, Jan. 1987

Fig. 14 Comparison between calculated and measured radial heat flux per unit axis length within the nozzle throat.

A reevaluation of Hügels onset explanation[6] has been conducted by means of the flow discharge calculations described above. The radial particle density was determined by equalizing the radial Lorentz forces with the pressure gradient, and for a given mass flow rate $\dot{m}$ the arc current was increased until the pressure or particle density at the innermost anode point dropped to zero. Plots of constant particle density lines for which this "plasma starvation" at the anode occurs are shown in Fig. 15a and b for $\dot{m}$ = 0.0006 kg/s with a critical current of I_{crit} = 3600 A and for $\dot{m}$ = 0.0015 kg/s with a critical current of 6020 A, respectively. Comparison between several of these calculations with measured onset conditions[7] show excellent agreement (see Fig. 16).

[6] H.Hügel, "Zur Funktionsweise der Anode im Eigenfeldbeschleuniger", DFVLR Report FB-80-20, 1980

[7] H. L. Kurtz, M. Auweter-Kurtz and H. O. Schrade, "Self Field MPD Thruster Design - Experimental and Theoretical Investigations", 18th International Electric Propulsion Conference, AIAA 85-2002, Alexandria, VA, 1985

$$\rho_{max} = .311 \cdot 10^{-3} \left[\frac{kg}{m^3}\right]$$

(a)

$\dot{m} = 0.0004$ [kg/s]
$I = 3100$ [A]

$$\rho_{max} = .114 \cdot 10^{-2} \left[\frac{kg}{m^3}\right]$$

(b)

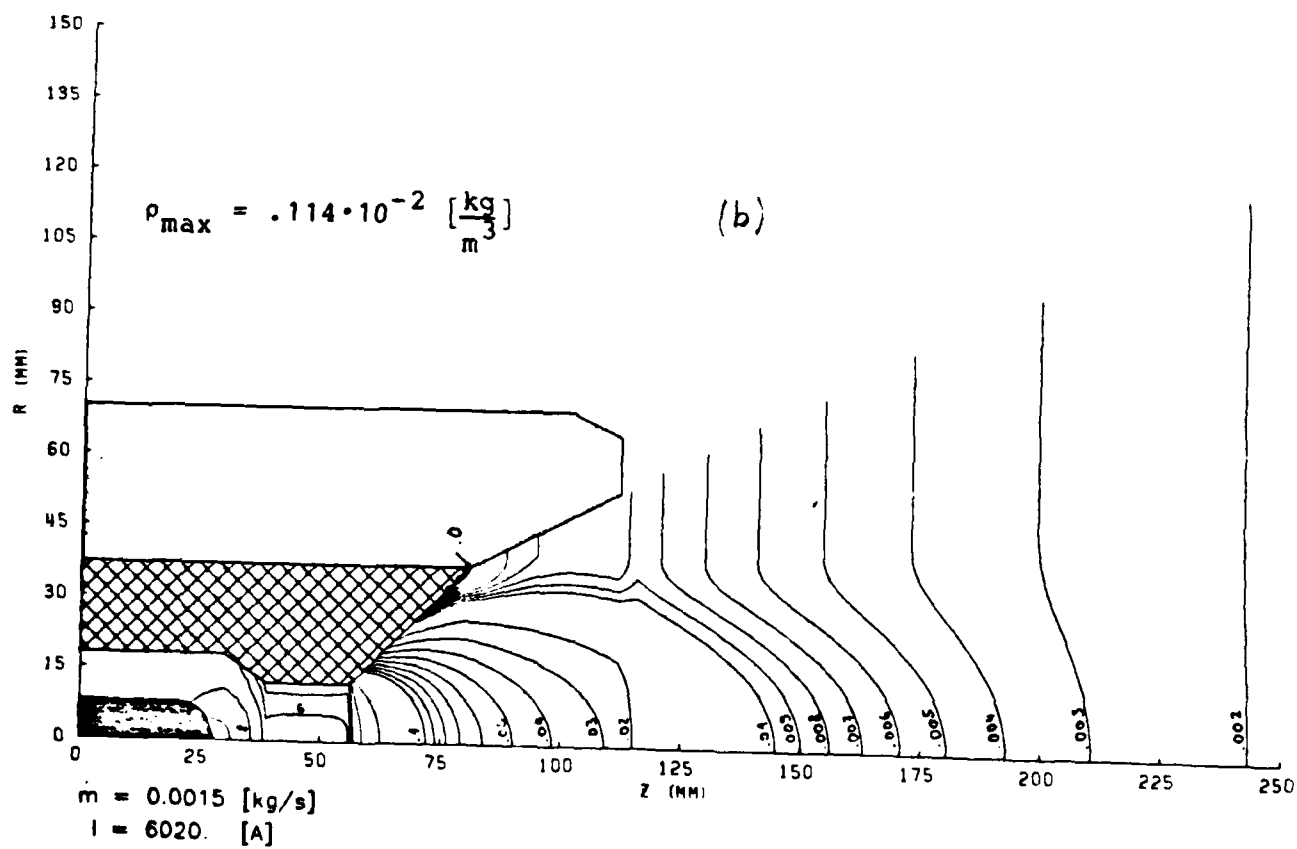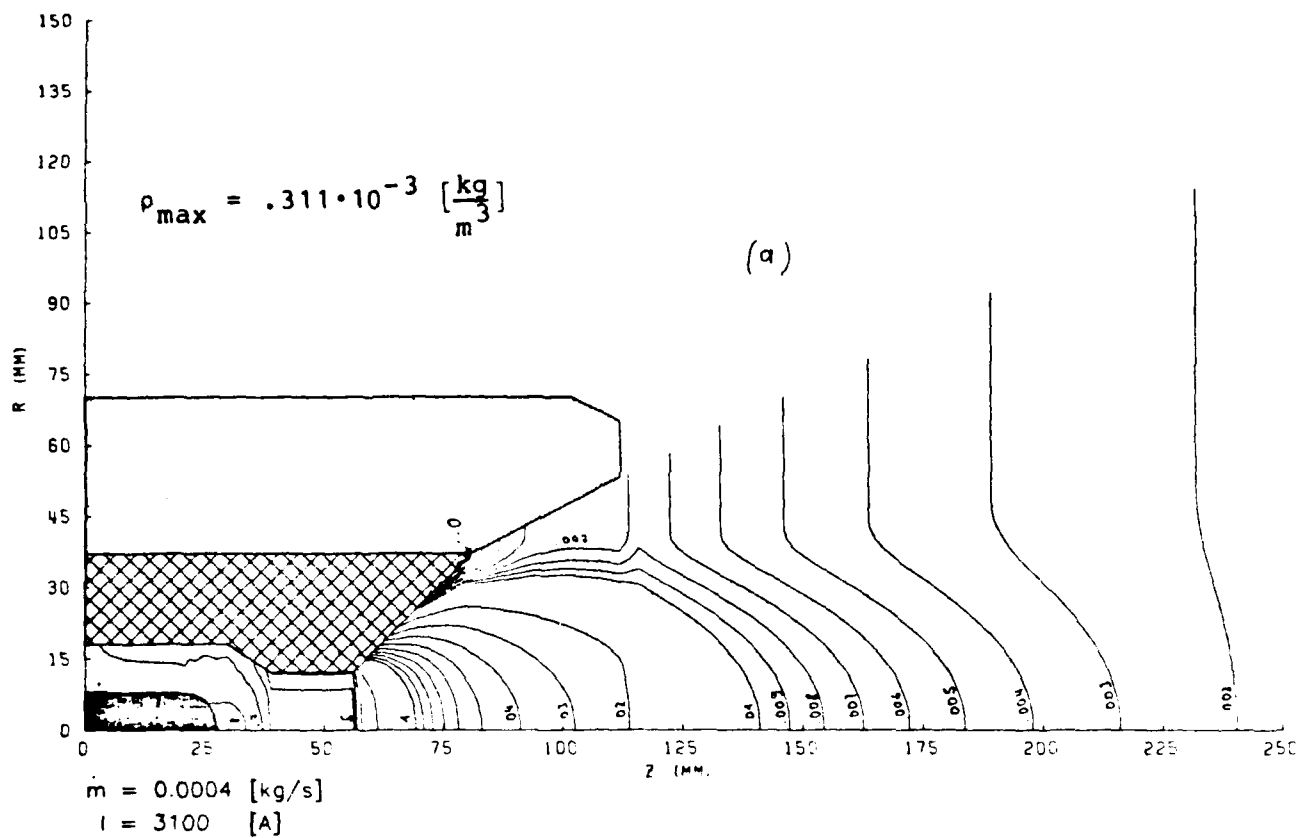$\dot{m} = 0.0015$ [kg/s]
$I = 6020$ [A]

Fig. 15 Lines of constant particle density at critical conditions.
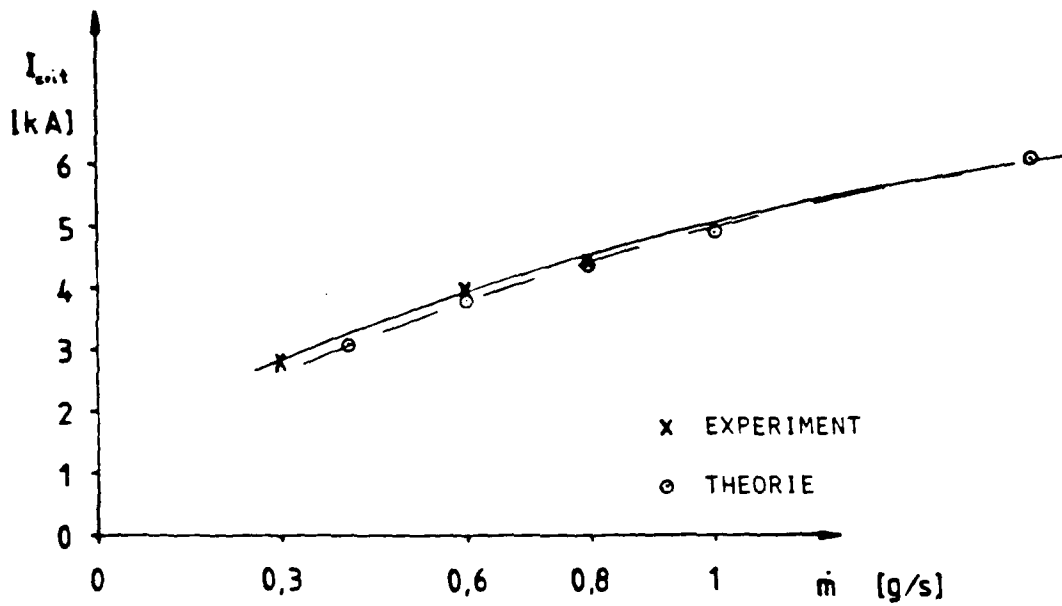
Onset Condition

Fig. 16 Comparison between Experiment and Theoretical Approach.

3.2 Cylindrical Thruster

In addition to the steady state nozzle type thruster calcula-
tions, a time dependent, fully two-dimensional, cylindrical MPD
channel flow calculation has been conducted. This numerical
treatment, which assumes rotational symmetry, friction free
flow, no azimuthal current or velocity and the electric field
perpendicular to the lengthwise limited coaxial electrodes (see
Fig. 17) has been described in Appendix III. Besides the example
already shown there, another one with a shorter current rise
time ($\sim$ 10 μs instead of 200 μs) and a lower mass flow rate
($\dot{m}$ = 5 g/s instead of 20 g/s) has been conducted and is presen-
ted here.

Based on the time dependent current profile as shown in Fig. 18,
the current contour lines and the pertinent plasma properties
like pressure, temperature and velocity were calculated as a
function of r and z for argon as propellant. At begin (t = 0)
the current was assumed strictly radial and homogeneously dis-
tributed across the electrode surfaces and the axial flow field
correspondingly homogeneously distributed across the cylindrical
tube cross section. The initial temperature and the Mach number
of the flow were taken T(t=0) = 10000°K and M_a(t=0) = 1.5, re-
spectively. In Fig. 17 the current contour lines are shown after
60 μs; the temperature, pressure and density fields after 10 μs
and after 60 μs each are plotted in Figs. 19, 20 and 21, respec-
tively. The axial velocity v_z, the Mach number and the magnetic
netic induction field are given in Figs. 22, 23 and 24, respec-
tively.

Interesting to note is the fact that the current contour lines
show a compression not only on the downstream side but faintly
also on the upstream side of the cathode. This effect could not
be observed in the previous example (Appendix III). The tempera-
ture and the pressure field show peaks on both ends of the cath-
ode during the current rise period. These peaks, however, flat-
ten out with time indicating more likely a certain insufficiency
in the initial conditions and/or in the computer code than in a

···   initial distribution

———   steady state condition
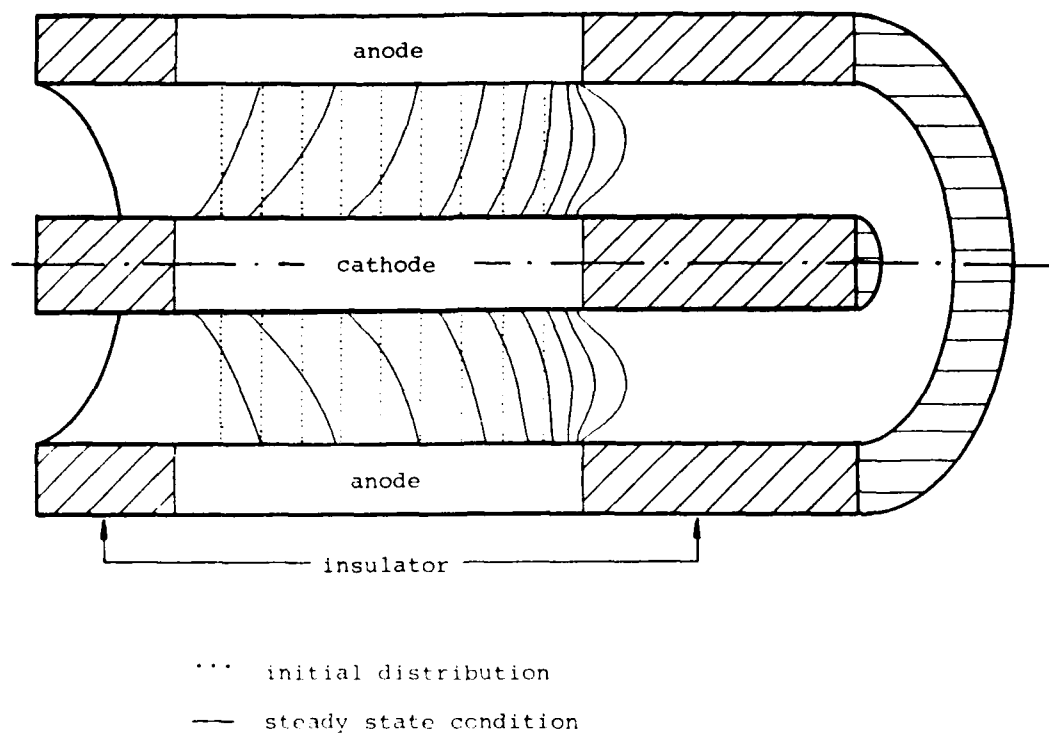
Fig. 17:   Current contour lines of a cylindrical MPD thruster.
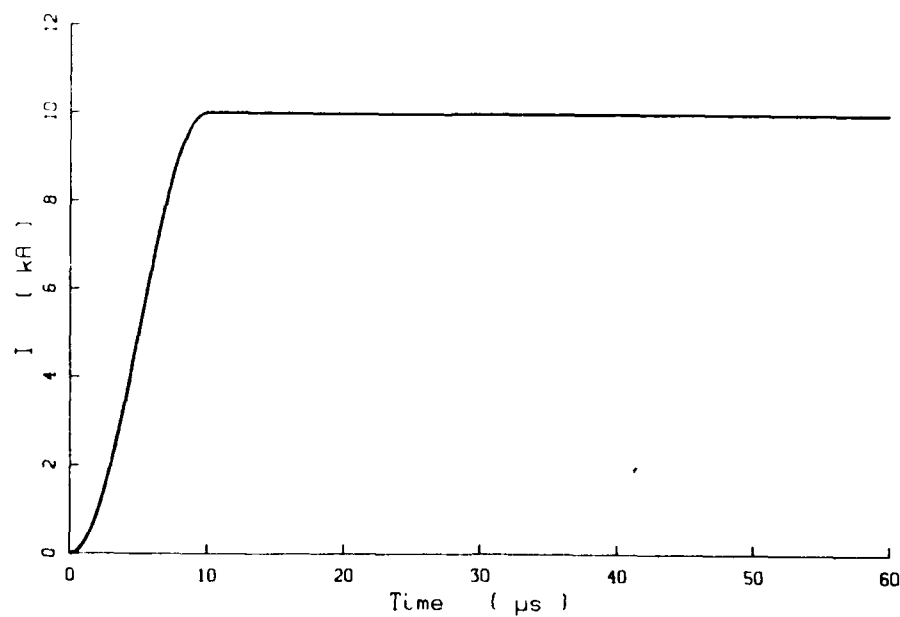
Fig. 18:   Current curve versus time.
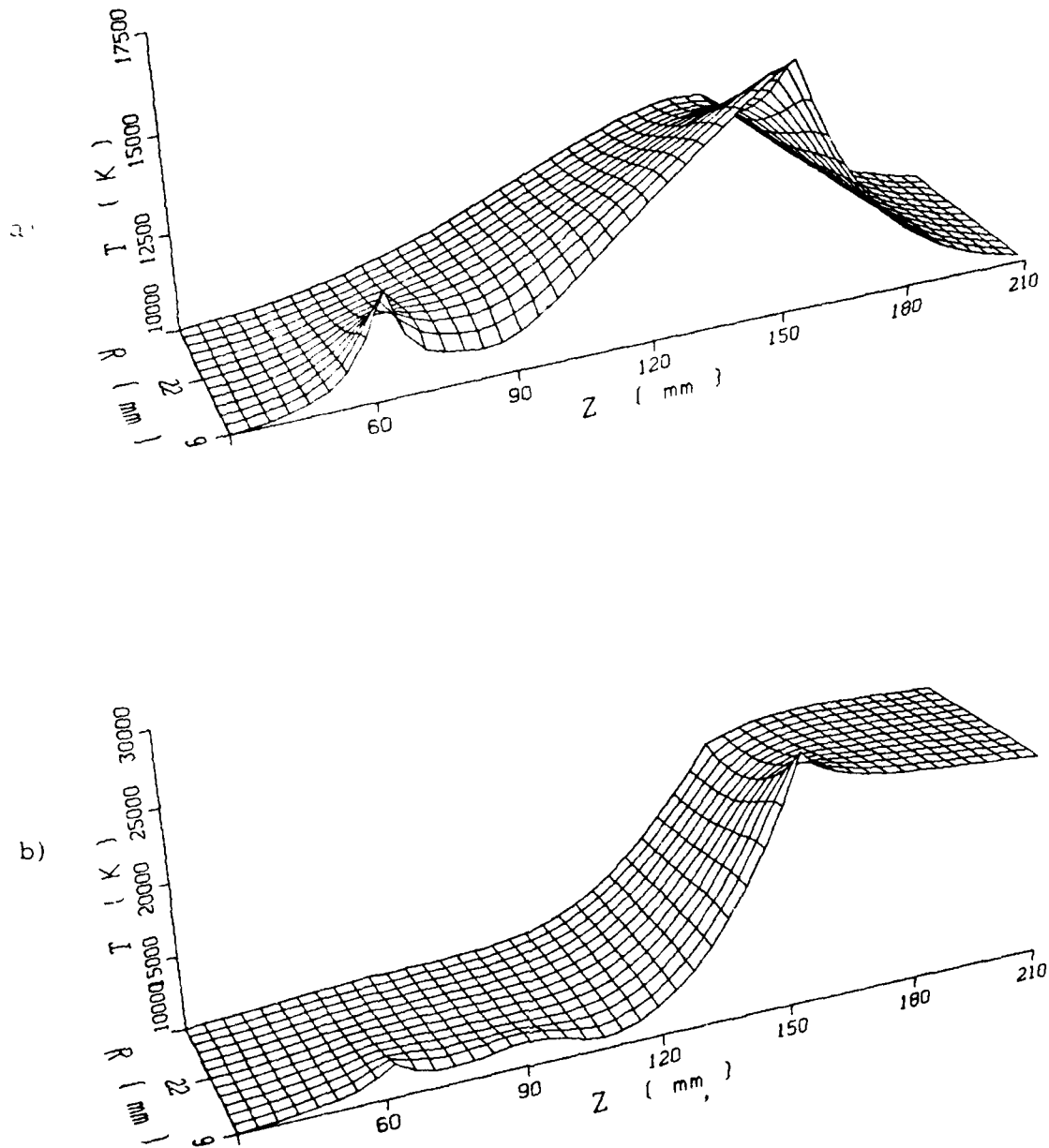
Fig. 19:   Temperature distribution within the channel at
           a) 10 μs,   b) 60 μs.
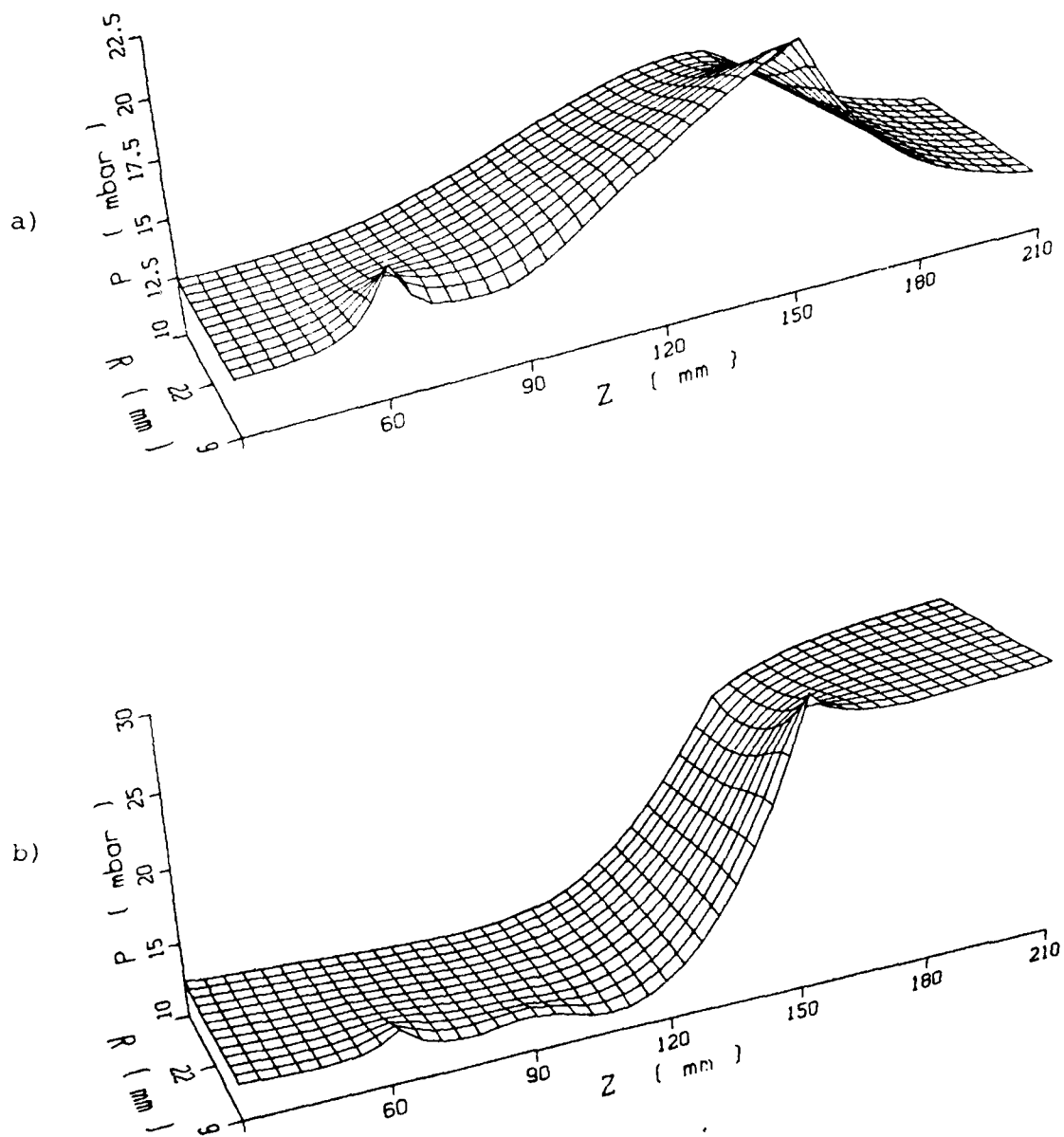
Fig. 20: Pressure distribution within the channel at
a) 10 µs, b) 60 µs.
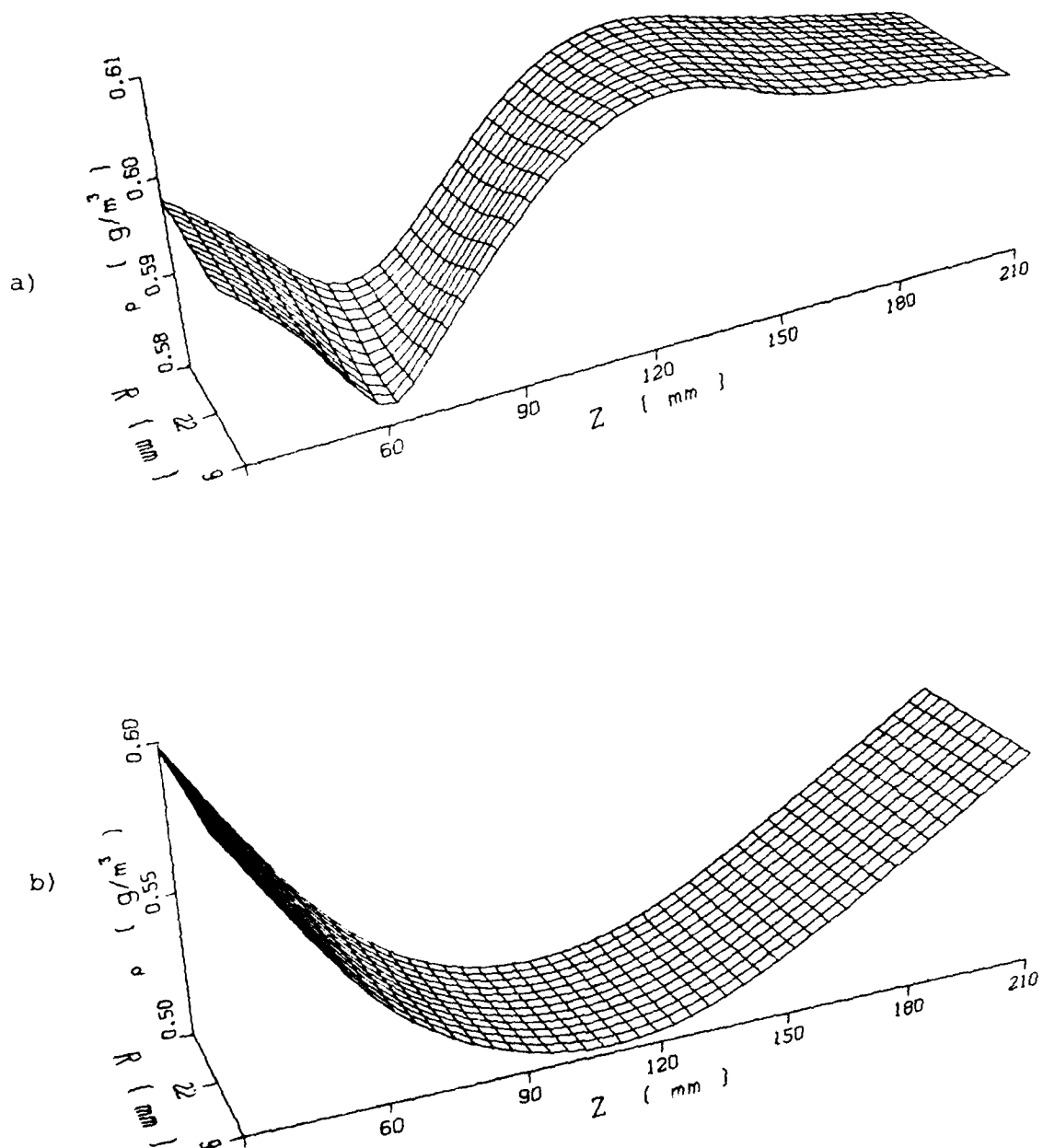
Fig. 21:   Density distribution within the channel at
a) 10 µs,   b) 60 µs.
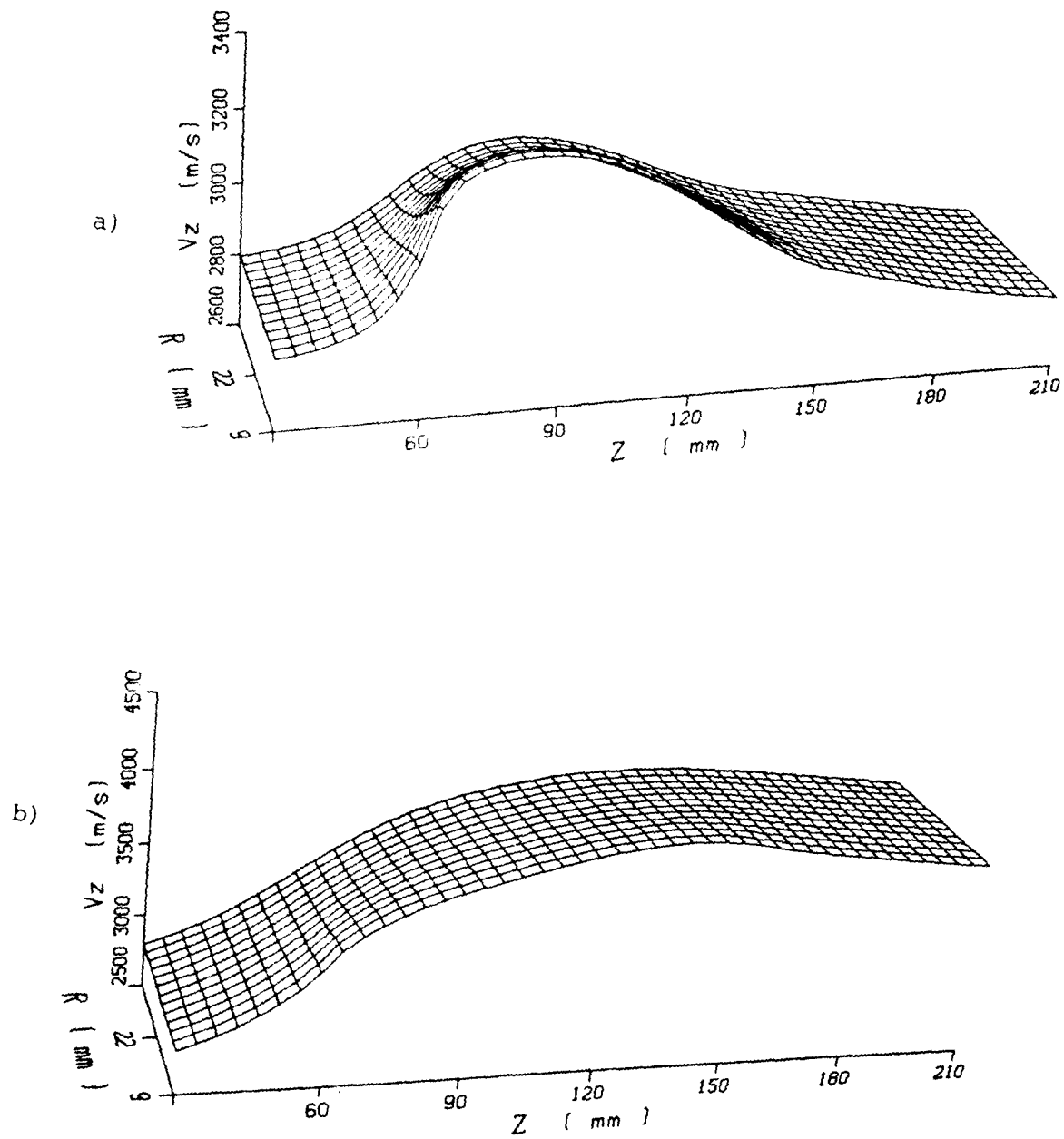
Fig. 22: Axial velocity distribution within the channel at
a) 10 µs, b) 60 µs.
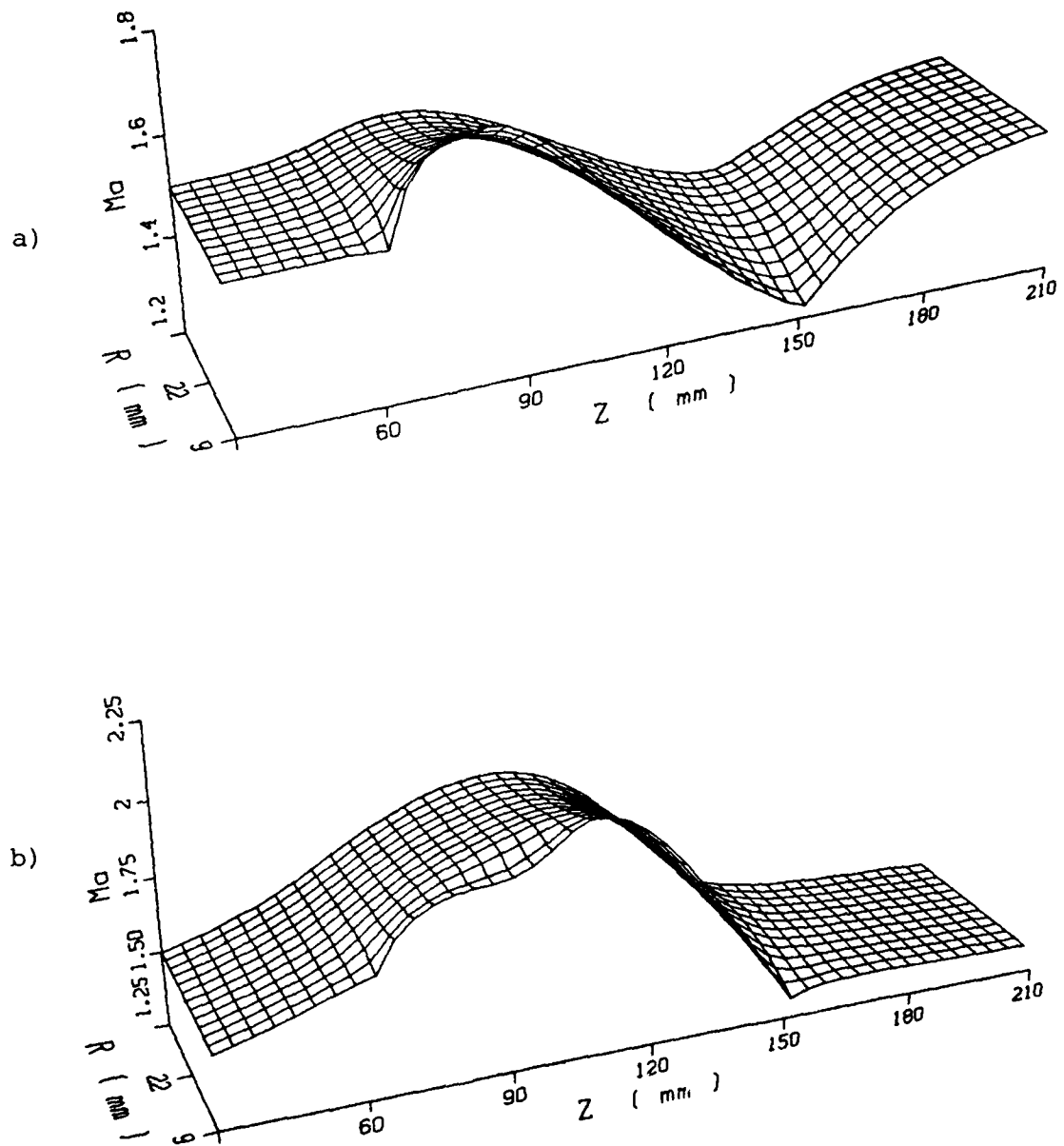
Fig. 23: Mach number distribution within the channel at
a) 10 µs,   b) 60 µs.
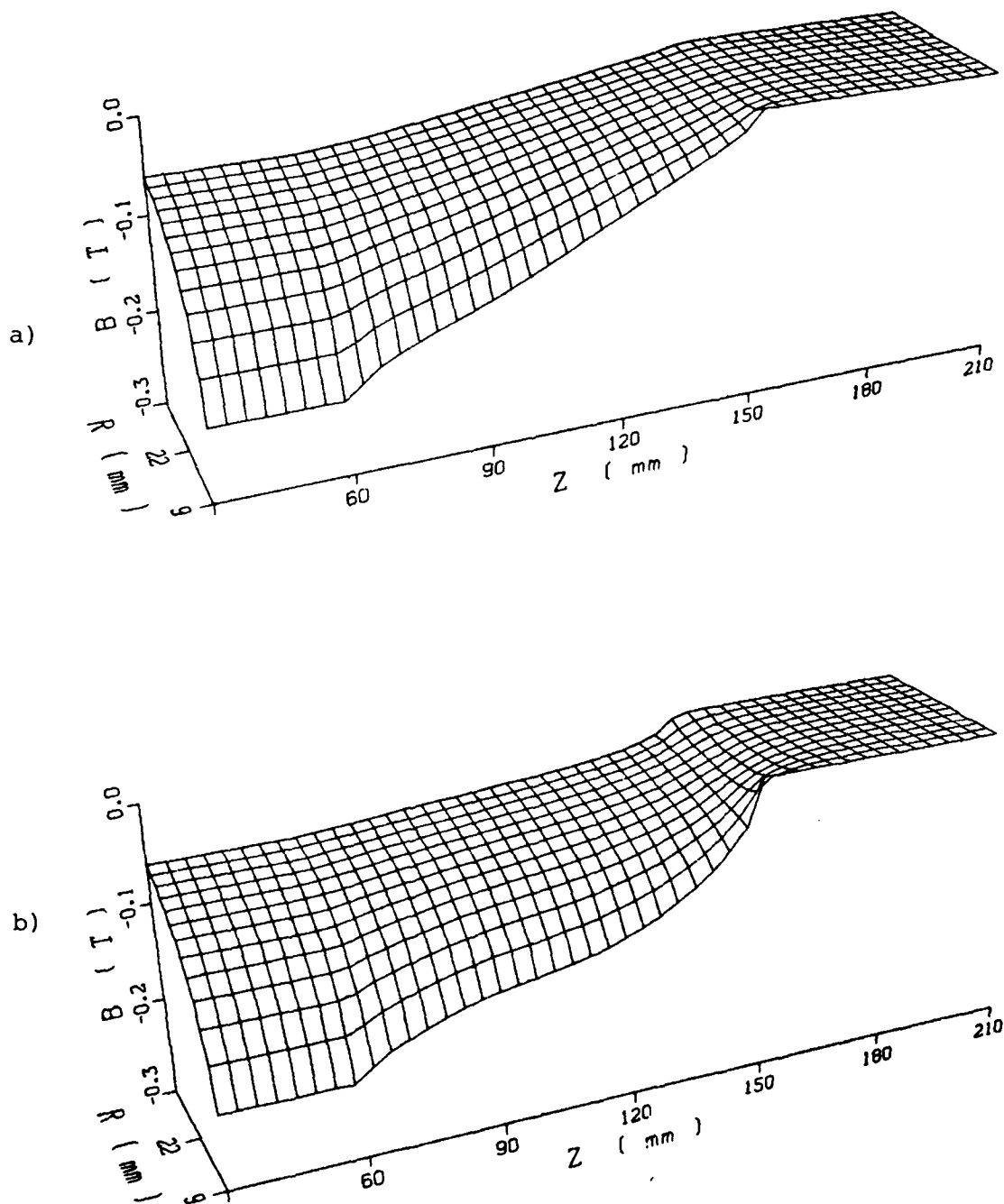
Fig. 24: Magnetic induction distribution within the channel at
a) 10 µs, b) 60 µs.
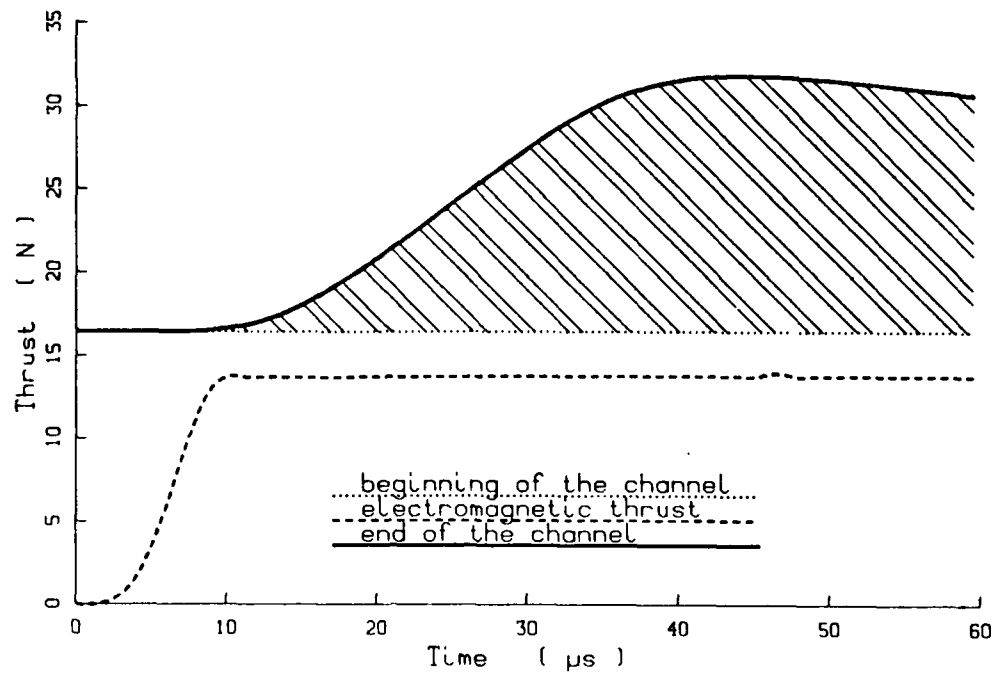
Fig. 25: Thrust versus time.
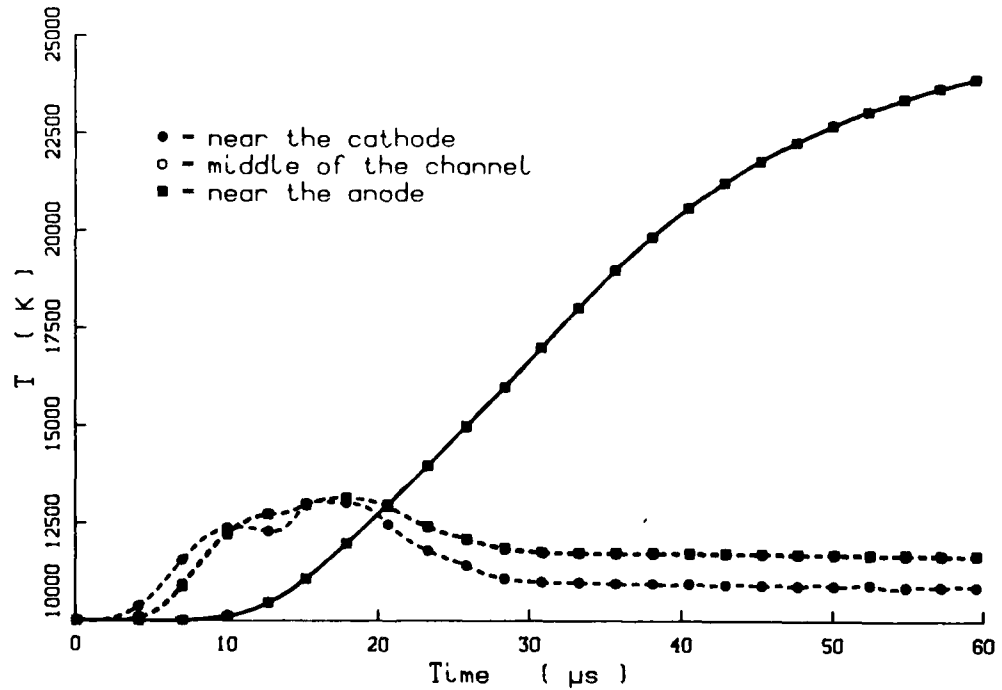
Fig. 26: Temperature versus time. Solid line: end of the chan-
nel. Dashed line: middle of the electrodes.
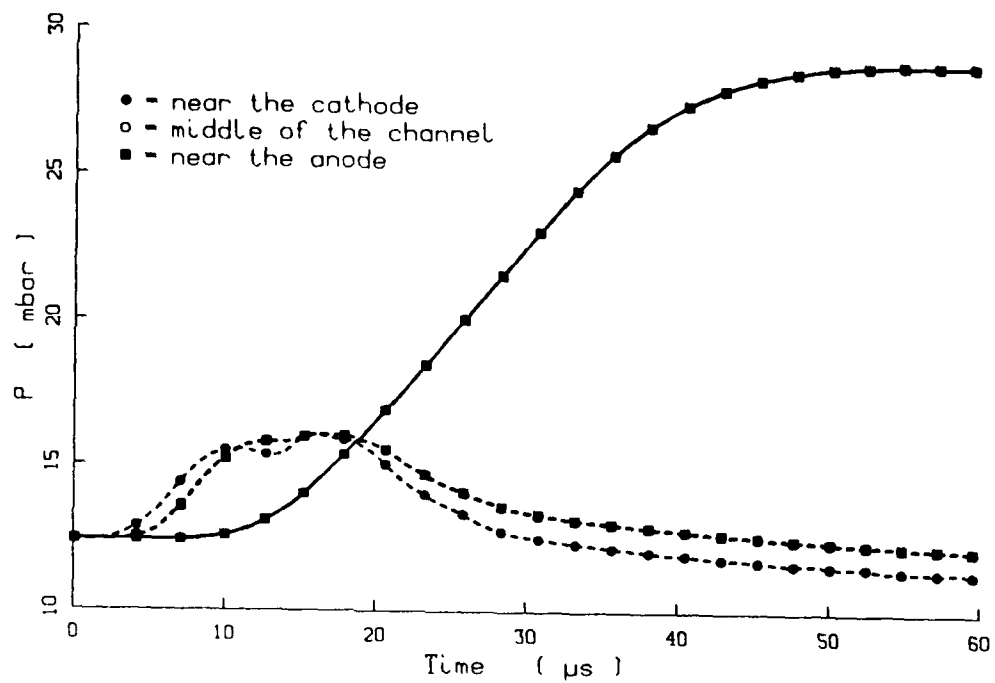
Fig. 27:   Pressure versus time. Solid line: end of the channel.
           Dashed line: middle of the electrodes.
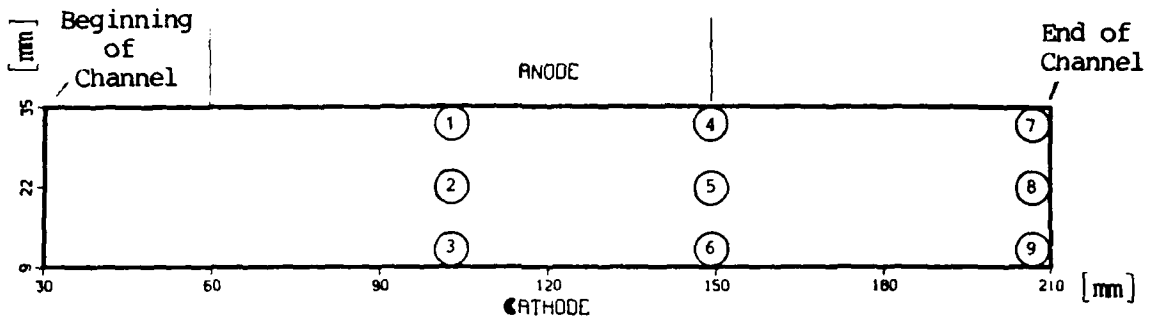
Electrode Region

①	-	middle of electrodes;	near anode
②	-	middle of electrodes;	middle of the channel
③	-	middle of electrodes;	near cathode
④	-	end of electrodes;	near anode
⑤	-	end of electrodes;	middle of the channel
⑥	-	end of electrodes;	near cathode
⑦	-	end of channel ;	near anode
⑧	-	end of channel ;	middle of the channel
⑨	-	end of channel ;	near cathode

Fig. 28 Localization of the different positions for the time
dependent considerations (Figs. 25, 26, 27).

real effect. Nevertheless, the computations so far yield reasonable overall results as shown by the thrust versus time curves in Fig. 25 and by the temperature and pressure versus time plots in Figs. 26 and 27. In these last three figures the differences in temperature and in pressure at the middle position and the near anode position are negligible; therefore, they lie for both positions on one curve, respectively. The localization of the different positions is shown in Fig. 28.

The thrust as plotted in Fig. 25 is defined by

$$Th = 2\pi \int_{r_c}^{r_a} (\rho v_z^2 + p)\, r\, dr$$

It is interesting to note that after about 40 μs the thrust at the end of the channel reaches a value which is a little higher than the sum of the gas dynamic and electromagnetic thrust. After that it decreases slowly and will reach this value (of gas dynamic and electromagnetic thrust) beyond 60 μs. During the current rise period (0 - 10 μs) the thrust at the channel end does not change, and only after more than about 60 μs does the thrust adjust to its constant steady state value.

Similarly, the temperature curve (see Fig. 26) at the end of the channel, which is practically the same curve for all three positions 7,8,9, reaches its steady state constant value only after more than 60 μs. The temperatures at the middle positions 1,2,3 of the electrodes increase at first to about 16000°K and after that drop slowly to about 11000° - 12000°K after again more than 60 μs.

The corresponding pressure curves in Fig. 27 show the same overall trend as the temperature curves. The pressure at the channel end reaches 29 mbar after about 55 μs.

The time τ which elapses after reaching overall steady state conditions con now be estimated by the length of the active channel portion (given by 210 mm - 60 mm = 0.15 m) divided by the average speed of sound (for argon at about 12000°K, $a \simeq 2 \cdot 10^3$ m/s) as

$$\tau = \frac{0.15}{2 \cdot 10^3} = 7.5 \cdot 10^{-5} \text{ s} = 75 \text{ } \mu\text{s}$$

This time is in good agreement with the adjustment times as calculated for the thrust, temperature and pressure according to the two-dimensional, time dependent MPD channel flow calculations presented.

4. List of reports and papers prepared during research period
    (1 August 1986 - 31 July 1987)

The following papers and student theses were prepared which directly relate to the research work of Grant AFOSR 86-0337.

Student Theses (Diplom)

P. Lehninger, "Designing and Building of a Test Pig in Order to Measure Cathode Erosion Caused by an Arc Pulse". IRS, Sept. 1986

A. Isselhorst, "Calculation of the Expansion Process in a Plasma Thruster by Accounting for Electromagnetic Compression". IRS, May 1987

Papers

M. Auweter-Kurtz, H.L. Kurtz, H.O. Schrade and P.C. Sleziona, "Numerical Modeling of the Flow Discharge in MPD Thrusters", 19th International Electric Propulsion Conference, AIAA-87-1091, May 1987

H. O. Schrade, M. Auweter-Kurtz and H. L. Kurtz, "Cathode Phenomnena in Plasma Thrusters", 19th International Electric Propulsion Conference, AIAA-87-1096, May 1987

5. <u>References</u>

[1] H. O. Schrade, M. Auweter-Kurtz and H. L. Kurtz, "Cathode Erosion Studies on MPD Thrusters", 18th International Electric Propulsion Conference, AIAA-85-2019, Alexandria, VA, 1985

[2] A. E. Robson, "The Motion of an Arc in a Magnetic Field", Proceedings of the Fourth International Conference on Ionization Phenomena in Gases, Vol. IIb, p. 346, Aug. 1959

[3] H. O. Schrade, M. Auweter-Kurtz and H. L. Kurtz, "Basic Processes of Plasma Propulsion", Final Scientific Report, AFOSR Grant 82-0298, Jan. 1987

[4] H. O. Schrade, M. Auweter-Kurtz and H. L. Kurtz, "Basic Processes of Plasma Propulsion", Final Scinetific Report, AFOSR Grant 82-0298, Jan. 1987

[5] H. O. Schrade, M. Auweter-Kurtz and H. L. Kurtz, "Stability Problems in magneto Plasmadynamic Arc Thruster", AIAA 18th Fluid Dynamics and Plasmadynamics and Lasers Conference, AIAA-85-1633, Cincinnati, OH, July 1985

[6] H. Hügel, "Zur Funktionsweise der Anode im Eigenfeldbeschleuniger", DFVLR Report FB-80-20, 1980

[7] H. L. Kurtz, M. Auweter-Kurtz and H. O. Schrade, "Self Field MPD Thruster Design - Experimental and Theoretical Investigations", 18th International Electric Propulsion Conference, AIAA 85-2002, Alexandria, VA, 1985

6. Appendices

6.1 Appendix I

Calculation of the Dimensionless Quantity ε

where
$$\varepsilon = \frac{8\pi}{m_0 I^2} \int_{A_z} \rho \, v_z^2 \, dA_z \; - \; [1 + f(n)] \qquad (I.0)$$
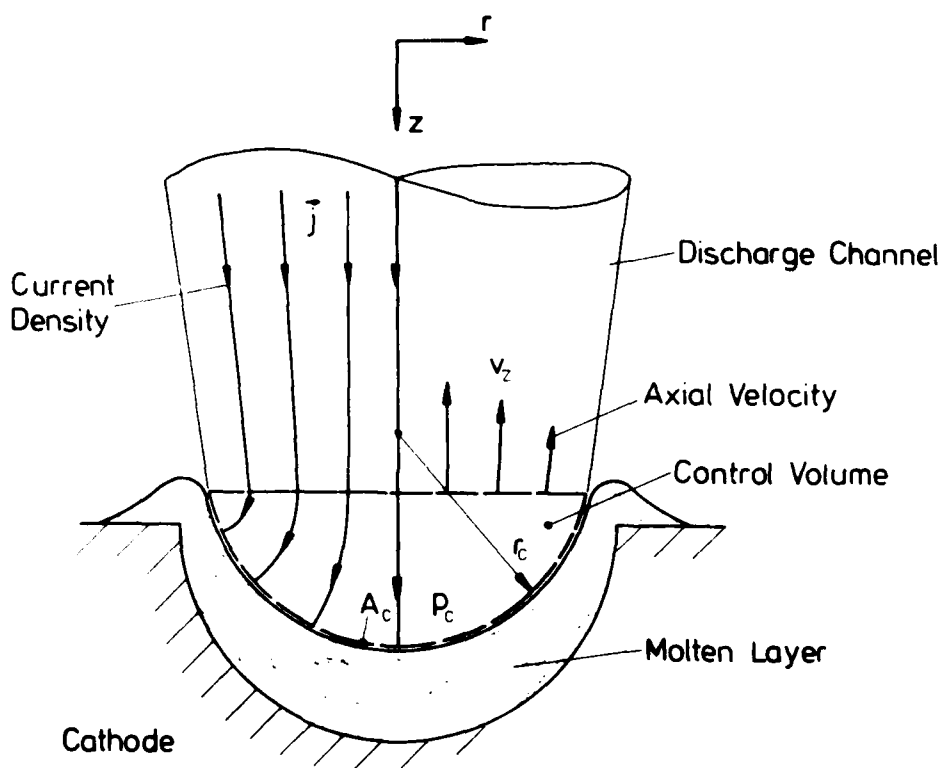

Fig. I1   Illustration of the current density lines and the Axial Velocity within a Spot Discharge

For the high pressure plasma and vapor region within the crater (see dashed control volume in Fig. I.1) the equation of motion follows by

$$\nabla \{\rho \overleftrightarrow{vv} + \overleftrightarrow{P}\} = \vec{j} \times \vec{B} \qquad (I.1)$$

and after integration over the control volume V and applying Gauss' theorem, one obtains

$$\int_A \{\rho \overset{\leftrightarrow}{v}\vec{v} + \vec{P}\}\, d\vec{A} = \int_V \vec{j} \times \vec{B}\ dV \qquad (I.2)$$

The surface integral on the left side can now be split into two terms, the integral over the cross sectional area of the discharge channel at the crater orifice ($A_z = \pi r_0^2$) and the surface integral over the inner spherical crater surface (A_C; see Fig. I.1). For the z component of eq. (I.2) one therefore obtains

$$\int_{A_z} \{\rho \overset{\leftrightarrow}{v}\vec{v} + \vec{P}\}\, d\vec{A}_z \vec{u}_z + \int_{A_C} \{\rho \overset{\leftrightarrow}{v}\vec{v} + \vec{P}\}\, d\vec{A}_z \vec{u}_z = \int_V \vec{j} \times \vec{B}\ dV \cdot \vec{u}_z \qquad (I.3)$$

where $\vec{u}_z$ is the unit vector in the z direction. If one now denotes the vapor and plasma pressure of the inner crater surface by p_C and the pressure and the axial velocity at the orifice by p_z and v_z, respectively, one can replace eq. (I.3) by

$$- \int_{A_z} \{\rho v_z^2 + p_z\}\, dA_z + \int_{A_C} \{p_C\} \cdot (d\vec{A}_C \cdot \vec{u}_z) = \int_V \vec{j} \times \vec{B}\ dV \cdot \vec{u}_z \qquad (I.4)$$

Herein the negation sign of the first integral stems from $d\vec{A}_z \vec{u}_z = -dA_z$; one neglects friction effects and assumes that at the inner crater surface the average randomized, thermal speed of the particles prevails over their convective velocity. Since now

$$d\vec{A}_C \cdot \vec{u}_z = + dA_z = + r\, dr d\theta \qquad (I.5)$$

where θ is the azimuth angle of the cylinder coordinates r, θ, z, it follows for the z component of the force balance eq. (I.3)

$$\int_{A_z} \rho v_z^2\, dA_z = \int_{A_z} (p_C - p_z)\, dA_z - \int_V \vec{j} \times \vec{B}\ dV \cdot \vec{u}_z \qquad (I.6)$$

The pressure p_C is now taken as constant, and by accounting for the magnetic or pinch pressure within the cross sectional

area A_z [8] and by denoting the ambient pressure through p_∞, one obtains

$$\int_{A_z} \rho v_z{}^2 \, dA_z = (p_c - p_\infty) \cdot A_z - \frac{\mu_0}{8\pi} \cdot I^2 - \int_V \vec{j} \times \vec{B} \, dV \cdot \vec{u}_z \qquad (I.7)$$

In order to calculate the volume integral over the electromagnetic forces in eq. (I.7), one now assumes that the current density is evenly distributed over the inner crater surface. The shape of the crater shall be approximated by a spherical segment which can be characterized by the angle ϕ_0 and the radius $r_0 = r_c \sin\phi_0$ (see Fig. I.2). By introducing the Maxwell's stress tensor $\overleftrightarrow{\tau}_{Maxwell}$, one now obtains for the volume integral

$$\int_V \vec{j} \times \vec{B} \, dV = \int_A \overleftrightarrow{\tau}_{Maxwell} \cdot d\vec{A} = \frac{1}{2\mu_0} \int \{2\vec{B}\vec{B} - \vec{B}^2 \overleftrightarrow{1}\} \cdot d\vec{A} \qquad (I.8)$$

where the magnetic induction vector $\vec{B}$ is given by the sum of the self field $\vec{B}_s$ and the applied field $\vec{B}_0$

$$\vec{B} = \vec{B}_s + \vec{B}_0 \qquad (I.9)$$

For the integrand, one may write

$$2\vec{B}\vec{B} - \vec{B}^2 \overleftrightarrow{1} = 2\overleftrightarrow{B_s B_s} + 2\overleftrightarrow{B_0 B_0} + 2\overleftrightarrow{B_s B_0} + 2\overleftrightarrow{B_0 B_s}$$

$$- (\vec{B}_s{}^2 + \vec{B}_0{}^2 + 2\vec{B}_s \cdot \vec{B}_0) \overleftrightarrow{1} \qquad (I.10)$$

Since now $\vec{B}_0$ can be considered constant and the vector $\vec{B}_s$ is normal to $d\vec{A}$ over the entire surface of the control volume, the integral (I.8) reduces to

$$\int_V \vec{j} \times \vec{B} \, dV = \frac{1}{2\mu_0} \int \{2\overleftrightarrow{B_s B_0} - (\vec{B}_s{}^2 + 2\vec{B}_s \vec{B}_0) \overleftrightarrow{1}\} \cdot d\vec{A} \qquad (I.11)$$

and the z component of this force to

---

[8] H. O. Schrade, "Magnetoplasmadynamic Effects in Electric Arcs", Interim Scientific Report, Grant AFOSR 82-0298, August 1983, p. 109ff.
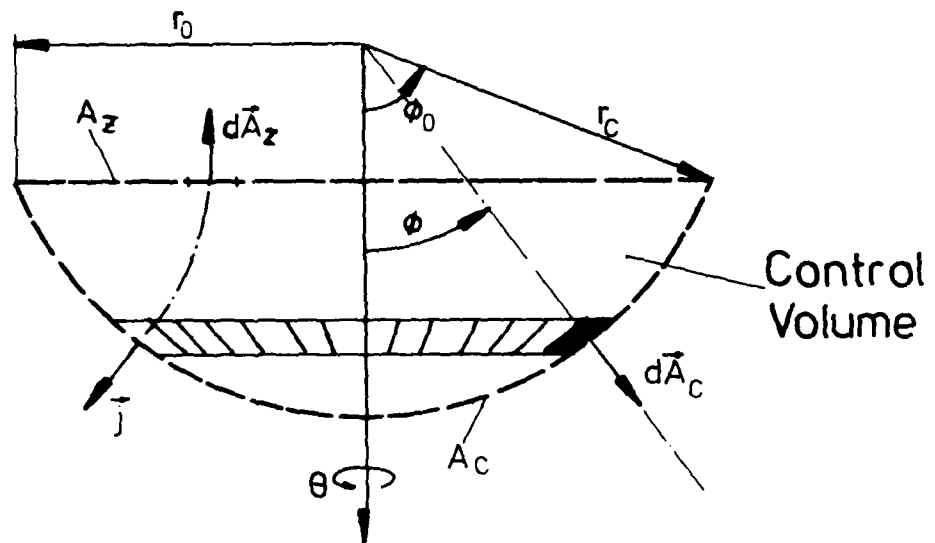
Fig. I.2   Geometry of the High Pressure Spot Zone presented by a spherical segment

$$\int_V \vec{j} \times \vec{B} \, dV \, \vec{u}_z = - \frac{1}{2\mu_0} \int \vec{B}_s^2 (d\vec{A} \cdot \vec{u}_z) \qquad (I.12)$$

The other terms vanish since $\vec{B}_{sz}$ and the divergence of $\vec{B}_s$ are zero. Splitting the surface integral in two parts as before, one obtains

$$\int_V \vec{j} \times \vec{B} \, dV \cdot \vec{u}_z = + \frac{1}{2\mu_0} \left\{ \int_{A_z} \vec{B}_s^2 \, dA_z - \int_{A_c} \vec{B}_s^2 (d\vec{A}_c \cdot \vec{u}_z) \right\} \qquad (I.13)$$

where $\quad dA_z = r \, dr \, d\theta \quad$ and $\qquad\qquad$ (a)

$$\qquad\qquad\qquad\qquad\qquad\qquad\qquad\qquad (I.14)$$

$$(d\vec{A}_c \cdot \vec{u}_z) = r_c^2 \sin\phi \, \cos\phi \, d\phi \, d\theta \qquad\qquad (b)$$

For a straight channel with a current density distribution given by a paraboloid of grade n, one obtains for the integral over the cross sectional area of the crater orifice

$$\frac{1}{2\mu_0} \int_{A_z} B_s^2 \, dA_z = \frac{\mu_0}{8\pi} I^2 \, f(n) \qquad (I.15)$$

with

$$f(n) = \frac{1}{2n^2} \left\{ (n+2)^2 - 16 \frac{n+2}{n+4} + \frac{8}{n+2} \right\} \qquad (I.16)$$

For a flat current density profile with $n = 10$, $f(10) = 0.655$; for a steep profile with $n = 2$, $f(2) = 0.917$.

The second surface integral in eq. (I.13) follows by

$$\frac{1}{2\mu_0} \int_{A_c} B_s^2 (d\vec{A}_c \, \vec{u}_z) = \frac{r_c^2}{2\mu_0} \int_{\theta=0}^{2\pi} \int_{\phi=0}^{\phi_0} B_s^2 \sin\phi \, \cos\phi \, d\phi \, d\theta$$

$$\qquad\qquad\qquad\qquad\qquad\qquad\qquad\qquad\qquad (I.17)$$

Since now the current density is evenly distributed over the inner spherical crater surface it follows according to Maxwell's law

$$B_s = \frac{\mu_0}{2\pi} \frac{I(\phi)}{r_c \sin\phi} \qquad (I.16)$$

where

$$I(\phi) = \int_0^{2\pi} \int_0^{\phi_0} j \, r_c^2 \sin\phi \, d\phi \, d\theta = 2\pi \, r_c^2 \, j \int_0^{\phi_0} \sin\phi \, d\phi$$

$$= 2\pi r_c^2 \, j \, [1 - \cos\phi] \tag{I.19}$$

Since the total current carried by the spot is

$$I = 2\pi r_c^2 \, j \, [1 - \cos\phi_0] \tag{I.20}$$

one obtains

$$I(\phi) = I \frac{1 - \cos\phi}{1 - \cos\phi_0} \tag{I.21}$$

and according to (I.18)

$$B_s = \frac{\mu_0}{2\pi} \frac{I}{r_c} \frac{1}{\sin\phi} \frac{1 - \cos\phi}{1 - \cos\phi_0} \tag{I.22}$$

Introduced into eq. (I.17) yields according to Standard Integral Tables [9]

$$\frac{1}{2\mu_0} \int_{A_c} B_s^2 \, (d\vec{A}_c \vec{u}_z) = \frac{\mu_0}{8\pi} I^2 \frac{2}{(1-\cos\phi_0)^2} \int_{\phi=0}^{\phi_0} \frac{(1-\cos\phi)^2}{\sin\phi} \cos\phi \, d\phi$$

$$= \frac{\mu_0}{8\pi} I^2 \frac{4}{(1-\cos\phi_0)^2} \left\{ 1 + 2 \ln(\cos \frac{\phi_0}{2}) - \cos\phi_0 \right.$$

$$\left. - \frac{1}{4} \sin^2\phi_0 \right\}$$

$$\equiv \frac{\mu_0}{8\pi} I^2 \cdot 2\zeta(\phi_0) \tag{I.23}$$

The dimensionless function $\zeta(\phi_0)$ is plotted in Fig. I.3 for the range $0 < \phi_0 < \pi/2$. The limit angle ϕ_0 is about zero for a flat crater and for a hemispherical crater $\pi/2$. $\zeta(\phi_0)$ varies therfore between 0.250 and 0.114 depending on the shape of the crater.

---

[9] e.g. Samuel M. Selby, "Standard Mathematical Tables", 16th Edition, The Chemical Rubber Co., Cleveland, OH, 1968
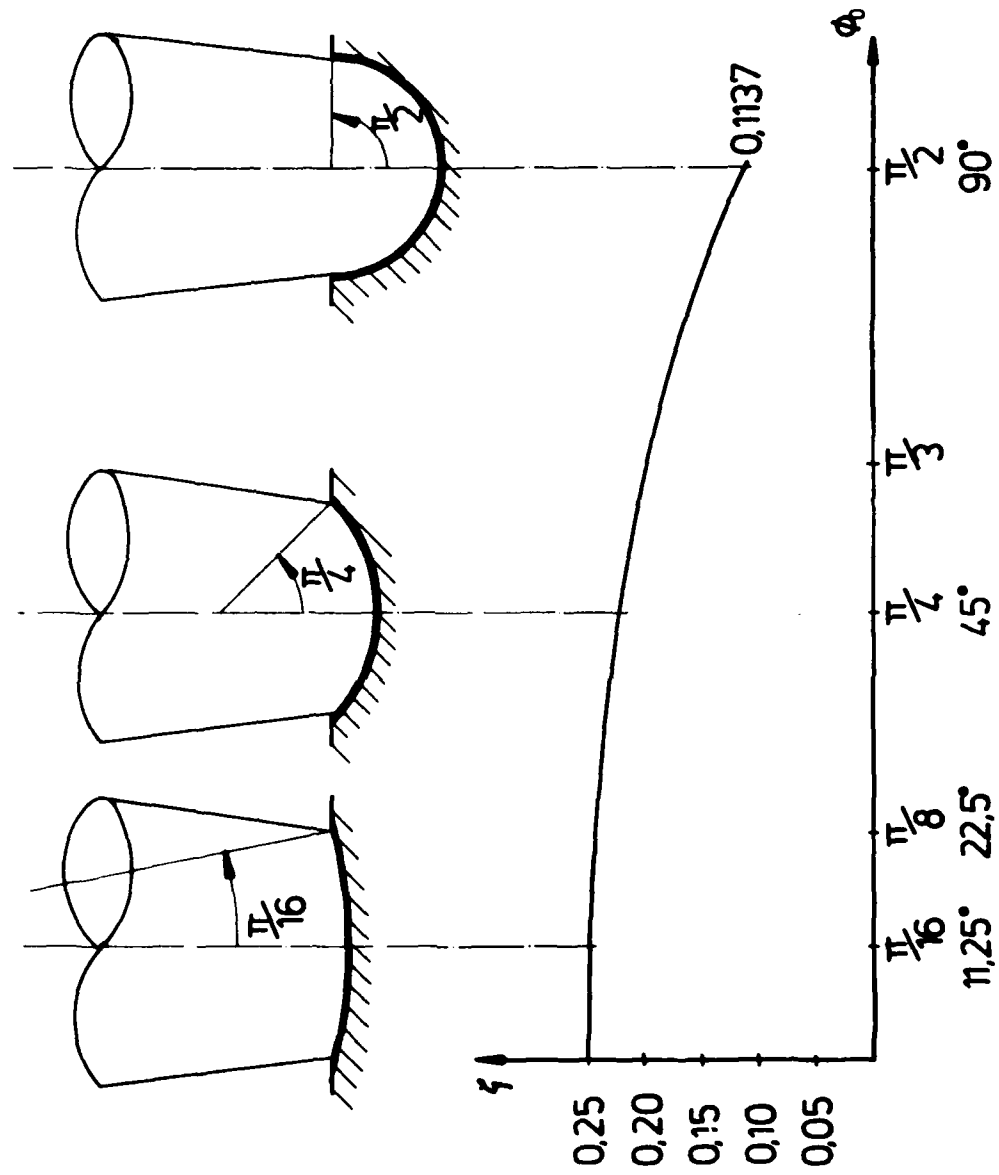
Fig. I.3   Plot of the Function $\zeta(\Phi_0)$

The volume integral over the electromagnetic forces in the z-direction follows now according to eqs. (I.13), (I.15) and (I.23) by

$$\int_V \vec{j} \times \vec{B} \, dV \cdot \vec{u}_z = \frac{\mu_0}{8\pi} I^2 \left\{ f(n) - 2\zeta(\phi_0) \right\} \tag{I.24}$$

This introduced into eq. (I.7) yields

$$\int_{A_z} \rho v_z^2 \, dA_z = (p_C - p_\infty)A_z - \frac{\mu_0}{8\pi} I^2 \left\{ 1 + f(n) - 2\zeta(\phi_0) \right\} \tag{I.25}$$

and hence the dimensionless quantity ε [eq. (I.0)] can be written

$$\varepsilon = \frac{p_C - p_\infty}{\frac{\mu_0}{8\pi} I \, \bar{j}} - 2 \left[1 + f(n) - \zeta(\phi_0) \right] \tag{I.26}$$

$$= \frac{p_C - p_\infty}{\frac{\mu_0}{8\pi} I \, \bar{j}} - 3.3 \tag{I.27}$$

The last approximation is well justified, since $f(n) = 0.8$ ($\pm$ 0.2) and $\zeta(\phi_0) = 0.15$ ($\pm$ 0.04). The factor 3.3 may therefore vary by about $\pm$ 15% depending on n, the grade of the current density paraboloid, and on ϕ_0, which characterizes the crater shape.

6.2 Appendix II

Cathode Phenomena in Plasma Thrusters

AIAA'87

H. O. Schrade, M. Auweter-Kurtz and H. L. Kurtz

Universität Stuttgart, Stuttgart, FRG

AIAA/JSASS/DGLR 19th International Electric Propulsion Conference

May 11-13, 1987 / Colorado Springs, Colorado

CATHODE PHENOMENA IN PLASMA THRUSTERS

H.O. Schrade
M. Auweter-Kurtz
H.L. Kurtz

Institut für Raumfahrtsysteme
Universität Stuttgart
Federal Republic of Germany

Abstract

Processes at the arc cathode attachment decisively determine the entire discharge behavior of almost all arc devices and therefore also of MPD and/or arc jet thrusters. One well known process occuring on spotty arc attachments in a transverse magnetic field is the fact that the cathode spots move or jump in the direction opposite to the Lorentzian rule. In pulsed thruster devices with cold cathodes and very likely also in continuously running thrusters with so-called thermionic, seemingly diffuse attachments of hot surfaces, the arc attachment consists of many high current density spots. These spots can stick or spread upstream and thereby overheat the insulating material of the backplate of the thruster. In this paper an explanation of the phenomena of spot motion is presented.

Introduction

Within pulsed gas-fed plasma thrusters with coaxial electrodes, one often observes that relatively high erosion takes place at the upstream side where the center cathode penetrates the backplate insulator (see Fig. 1).

This fact, together with the arc traces left on the cathode surface, indicate that the arc cathode attachment which consists of many highly instationary hot spots sticks preferably to the cathode base. Scanning electron micrographs of cathode surfaces which were charged by high current pulses of up to 10 kA reveal typical craters of about 1 μm to almost 100 μm in diameter, which confirms the existence of many seemingly statistically distributed hot spots. Any one of these active spots may be characterized by a crater-like pit with an inner molten layer, as shown in Fig. 2.

Within the pit exists a high pressure plasma caused by ohmic heating and heavy evaporation of the electron emitting inner surface layer. This high pressure plasma expands out into the ambient lower pressure gas sphere and forms a plasma jet. Depending on the lifetime of the spot and the size of the molten layer, droplets can also be ejected from such an active site, drastically increasing the surface damage and the erosion rate of such a spotty arc attachment. Since the ejected plasma is electrically conducting, one must also consider that a current-carrying channel emanates from the crater orifice. The current density of the orifice can assume values of up to the order of 10^{12} A/m^2 and possibly even higher[1], and the power density within an active spot correspondingly reaches values of up to about 10^{16} kW/m^3 within a region of a few micrometers.

The arc attachment consists now of many of these spots jumping seemingly statistically over the cathode surface. As shown experimentally in many different arc devices, the first time by Stark[2] and since then by numerous researchers,[1,3,4] the spotty arc attachment moves in the direction opposite to Ampere's law if an applied magnetic field is present and is oriented parallel to the cathode surface. Since its discovery, this well known but still not well understood phenomenon of arc retrograde motion has sparked the imagination of many scientists, stirring them to develop various hypotheses.[5-11] A presentation and scrutiny of all these interpretations would extend beyond the scope of this paper, and a good many have been experimentally refuted and/or do not rest on solid physical foundations. Even the many experimental findings at first did not fully correspond with each other; however, since the scanning electron microscope for the examination of the arc footprints on the cathode surface is available, the experimental results become unequivocal but reveal even more complexity as originally assumed.

An additional phenomenon was observed first by Smith[12] and later by Kesaev[13] in a diverging
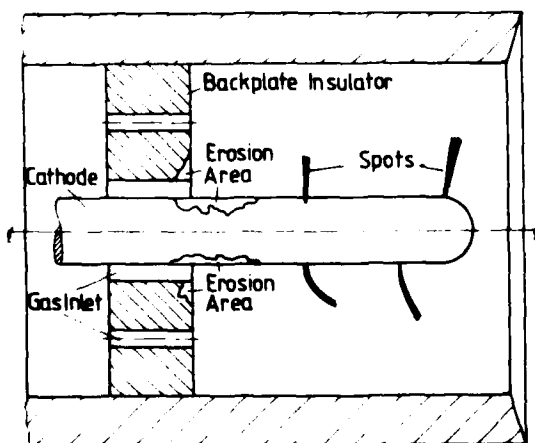

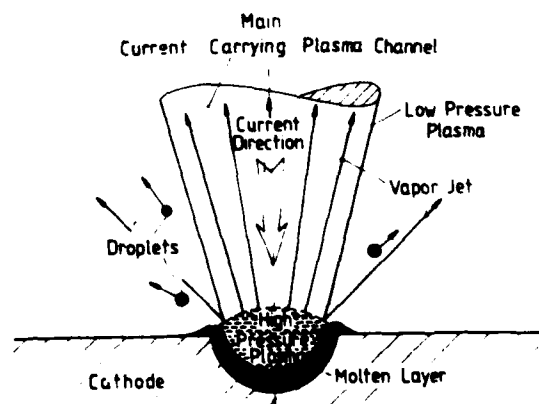Fig. 1 Illustration of the area with relatively high erosion.

Fig. 2 Scheme of a spot discharge with a straight discharge channel.

1

magnetic field and afterwards was experimentally proven to occur also in an inclined constant magnetic field.[14],[15] It shows that if the magnetic field lines are somewhat inclined with respect to the cathode surface, the spots discontinuously drift away from the retrograde direction. This drift motion was extensively investigated by Robson and is therefore named after him.

In this paper an analysis is presented which uniquely explains these strange phenomena. The consequences on the spot behavior in a coaxial plasma thruster are discussed.

Qualitative Explanation

The vapor and plasma jet which proceeds from a superheated cathode spot is electrically conductive and thus contains the intrinsic, current-carrying channel; the latter electrically connects the cathode spot and thus the cathode with the plasma of the interelectrode space and thereby with the anode.

First let us consider an axially symmetrical discharge channel which converges to the electrode, having its origin in the cathode spot. The magnetic field lines of such a current-carrying channel are the concentric circles around the channel axis and, in accordance with the converging lines of the current density vector field, induce an electromagnetic volume force ($[\vec{j} \times \vec{B}]$ force), which has components normal and/or parallel to the axis. If one plots the values of these forces acting radially inward on a cross sectional plane, then one obtains a volcano-like profile, as seen in Fig. 3.

On the basis of this force profile, one obtains a pressure increase in the plasma channel towards the discharge center, which is known as "pinch pressure". The average pressure increase in the channel is calculated as

$$\Delta p_{Mag} = \frac{\mu_0}{8\pi} I\bar{j} \qquad (1)$$

where $\bar{j}$ represents the current density averaged over the cross-sectional area and I is the electric current flowing through the channel ($\mu_0 = 4\pi \cdot 10^{-7}$ Vs/Am magnetic permeability). Actually, this is a well known effect; it shows, however, that in low pressure discharges the magnetic pressure increase can be of a much greater magnitude than the surrounding pressure, and that self-magnetic or rather plasmadynamic effects dominate over electrostatic effects in the quasi-neutral discharge channel.
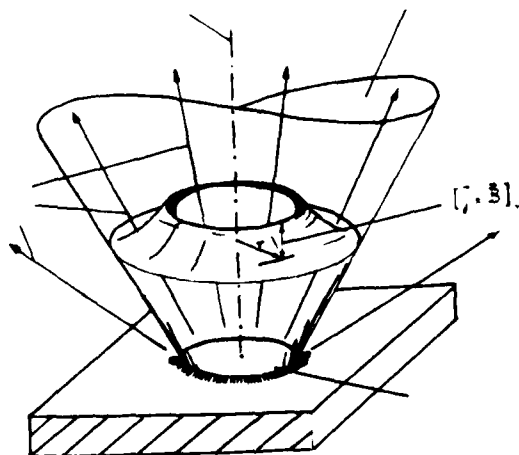

Fig. 3 Rotationally symmetric, straight spot discharge with radial $\vec{j} \times \vec{B}$ force distribution.
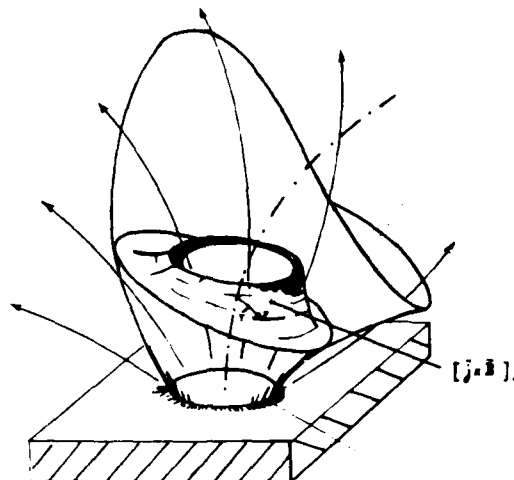

Fig. 4 Curved asymmetric spot discharge with radial $\vec{j} \times \vec{B}$ force distribution.

If this channel is curved (see Fig. 4), then the magnetic field lines on the concave side of the channel are condensed and on the convex side are spread out. This means, however, that the radial $[\vec{j} \times \vec{B}]$ forces on the concave side become larger than on the convex side, and the original, axially symmetrical, volcano-like force profile, distributed over the cross-sectional area of the channel, becomes asymmetrical. This asymmetry has the effect that the cathode vapor plasma, under high pressure and ohmically heated, can now no longer be held together by the magnetic forces; it expands or streams out on the weak-force side of the channel and is thereby diverted off the axial direction. Analogous to the operation of rocket propulsion, in which the repulsion of the outflowing gas produces surface forces on the walls of the combustion chamber and propells it into the opposite direction of the flow, the discharge channel is now driven in the direction opposite to the deflected vapor and plasma beam, and the chamber walls of the rocket engine may be compared with the confining radial $\vec{j} \times \vec{B}$ force configuration. I.e. the axial vapor- and plasma jet flowing out from the cathode spot is deflected in the direction of smaller force fields, while the intrinsic current-carrying channel is deflected in the opposite direction (see Fig. 4).

Under certain conditions, this deflection of the current-carrying channel can become so strong, that it contacts and heats up the cathode surface at a new point neighboring the spot. Cathode material is thereby vaporized also at this point, and ultimately a new electrode contact in the form of a new cathode spot arises (see Fig. 5).

In fact, an electrically conducting plasma-vapor mixture exists outside of the intrinsic current-carrying channel, so that a large part, but not all of the current carried by the spot will flow through the intrinsic current channel. The current density in the intrinsic channel is always much larger, however, than that outside of the channel considered.
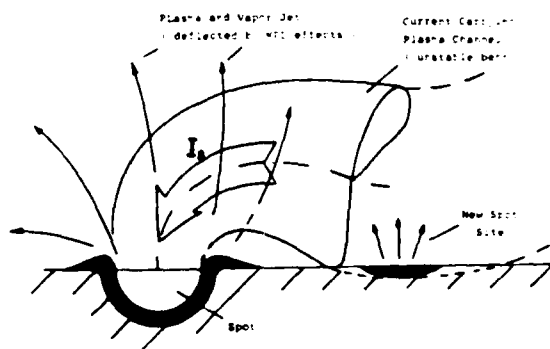
Fig. 5 Spot propagation due to bending of the current channel.

Fixed Coordinate System

Fig. 7 Illustration of the channel bound (x,y,z) and the fixed (x_L, y_L, z_L) coordinate systems with respect to the laboratory frame of reference.

$$\frac{\partial}{\partial t} (\rho \vec{v}_L) + \nabla \{\rho \overleftrightarrow{v_L \vec{v}}_L + \vec{P}\} = \vec{j} \times \vec{B} \qquad (2)$$

$$\frac{\partial}{\partial t} \rho + \nabla(\rho \vec{v}_L) = 0 \qquad (3)$$

$$\nabla \times \vec{B} = \mu_0 \vec{j} \qquad (4)$$

$$\nabla \vec{B} = 0 \qquad (5)$$

where ρ = plasma density

$\vec{v}_L$ = plasma velocity measured within the laboratory frame of reference

$\overleftrightarrow{v_L \vec{v}}_L$ = tensor dyode of $\vec{v}_L$

$\vec{j}$ = electric current density
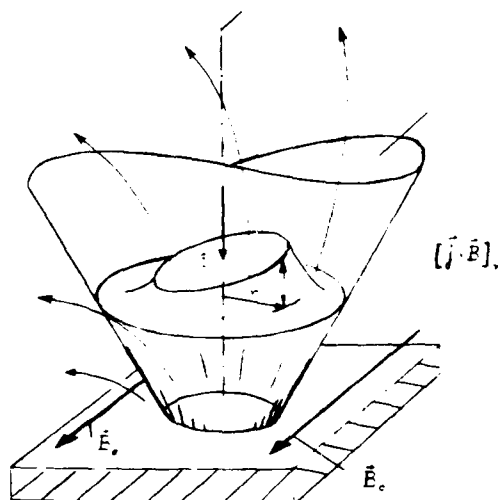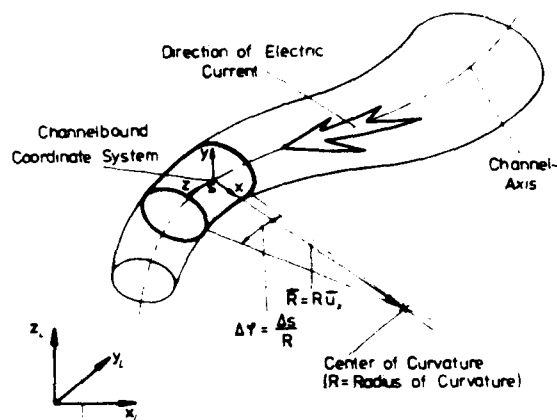
$\vec{B}$ = magnetic induction

Fig. 6 Straight spot in a transverse magnetic field. Plasma jet is deflected in the amperian direction.

If the discharge channel is situated in an external magnetic field running parallel to the cathode surface, the radial $[\vec{j} \times \vec{B}]_r$ force profile can become asymmetrical without additional curving of the discharge channel (see Fig. 6). The effect of this asymmetry, however, as in the case discussed above, is a deflection of the vapor and plasma beam in the amperian direction, while a resulting gas dynamic surface force acts on the current-carrying channel in the opposite (retrograde) direction. It can now be shown that under certain conditions this gas dynamic force in the retrograde direction predominates over the Lorentz force ($\vec{I} \times \vec{B}_0$) in the amperian direction. The channel axis is thereby curved in the retrograde direction until the discharge channel ultimately, as in the previous example (shown in Fig. 5), contacts and heats up the cathode surface. In this way, a new, distinct cathode attachment point arises on the retrograde side of the original spot. The cathode attachment point reproduces itself accordingly in the retrograde direction.

Theory

One considers any arbitrary configuration of a current-carrying channel within a fixed laboratory system $(x_L, y_L, z_L;$ see Fig. 7). The theory starts from the equation of motion, the continuity equation and Maxwell's equation

One now replaces the velocity vector v_L of the fixed system (x_L, y_L, z_L) by

$$\vec{v}_L = \vec{v} + \vec{v}_s \qquad (6)$$

i.e. by the sum of the plasma velocity $\vec{v}$, measured within the channel bound system (x,y,z; see Fig. 7) and the axis velocity v_s which has only transverse components with respect to the channel axis

$$\vec{v}_s = \begin{bmatrix} v_{sx} \\ v_{sy} \\ 0 \end{bmatrix} \qquad (7)$$

After integration of the equation of motion over a channel segment of length Δs (see Figs. 7 and 8) one eventually obtains the force balance for the channel segment in the form

$$(\Delta m) \frac{d\vec{v}_s}{dt} = \vec{X} \Delta s \qquad (8)$$

where $\Delta m = \int_{\Delta V} \rho \, dV$ is the mass of the plasma within the segment of volume ΔV and length Δs
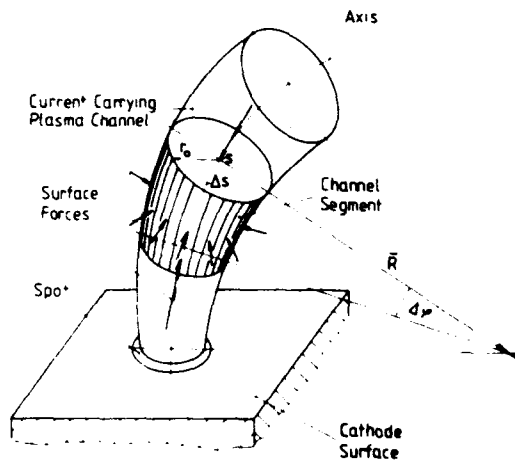
3

Fig. 8 Curved discharge channel segment of length $\Delta s = R\Delta\phi$ ($\vec{R}$ = radius of curvature vector).

$\vec{X} \Delta s$ is the sum of all forces which act on the segment and accounts for

a) all gas dynamic surface forces like propelling, friction, and pressure effects
b) the volume forces due to electromagnetic effects between the current-carrying elements inside and outside the segment and
c) all fictitious forces like Coriolis and centrifugal forces due to an axial flow within a curved and/or twisted current-carrying plasma channel.

This normal force $\vec{X}_\perp$ per unit channel length has now been calculated[16] by modeling the current density distribution within the channel by any "eccentric paraboloid of grade n". Such a distribution follows from a concentric paraboloid through shifting the maximum to a point of the channel cross section with the coordinates (r_M, θ_M) as shown in Fig. 9.

This modeling allows a very good approximation of any real current density distribution by adjusting the grade n and the eccentricity coordinates (r_M, θ_M). This is the more justified since in the
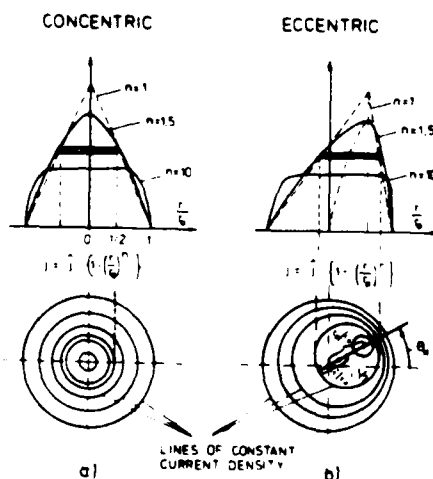

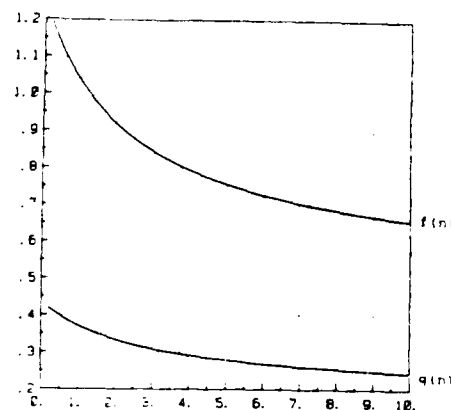Fig. 9 Current distribution modeled by a) a concentric and b) an eccentric paraboloid of grade n.

Fig. 10 Plot of the functions f(n) and g(n).

final expression of the force $\vec{X}_\perp$ the current density j shows up only within the integral expressions

$$\frac{1}{2\mu_0} \int_{A_z(s)} \vec{B}_s^2 \, dA_z = \frac{\mu_0}{8\pi} I^2 \, f(n) \, \{1 + g(n) \, \frac{r_M}{R} \cos\theta_M\} \tag{9}$$

$$\left.\begin{matrix}\alpha\\\beta\end{matrix}\right\} = \frac{1}{I} \int_0^{2\pi} \int_0^{r_0} j \frac{r}{r_0} \left\{\begin{matrix}\cos\theta\\\sin\theta\end{matrix}\right\} r \, dr \, d\theta = \frac{1}{n+3} \frac{r_M}{r_0} \left\{\begin{matrix}\cos\theta_M\\\sin\theta_M\end{matrix}\right\} \tag{10}$$

where $\vec{B}_s$ is the self magnetic field induced by the channel current I and which depends on the current density distribution within the channel; $r \, dr \, d\theta = dA_z$ is a surface element of any cross sectional area of the channel; α, β are measures of the eccentricity of the current density (moments of j in the x- and y- direction); and f(n) and g(n) are functions of the grade n and are plotted in Fig. 10. The transverse force $\vec{X}_\perp$ follows finally in the form

$$\vec{X}_\perp = \{\frac{\mu_0}{8\pi} I^2 \, [1 + f(n) + \frac{r_0}{R} \, (f(n)g(n)(n+3) + 1)\alpha$$

$$+ \frac{3}{4} (\frac{r_0}{R})^2] + \frac{1}{8\pi} \frac{r_0}{R} \, \beta \, \frac{dA_z}{ds} \, (\vec{I} \cdot \vec{B}_0) - \int_{A_z} \rho v_z^2 \, dA_z$$

$$+ R \frac{d\gamma}{ds} \int_{A_z} \rho \, v_z (v_y + v_{sy}) \, dA_z\} \frac{\vec{R}}{R^2}$$

$$+ \{\frac{1}{4\pi} \frac{dA_z}{ds} \, (\vec{I} \cdot \vec{B}_0) \, [1 + \frac{1}{2} \frac{r_0}{R} \, \alpha] - \frac{8\pi}{\mu_0} I^2 \frac{r_0}{R} \, \beta$$

$$+ R \frac{d\gamma}{ds} \int_{A_z} \rho \, v_z \, (v_x + v_{sx}) \, dA_z\} \frac{\vec{I} \times \vec{R}}{IR^2} - \frac{r_0}{R} \, \alpha \, \vec{I} \times \vec{B}_0 \tag{11}$$

where
$A_z = \pi r_0^2$ channel cross section

$\frac{dA_z}{ds} = 2\pi r_0 \frac{dr_0}{ds}$ channel divergence or convergence

$\int_{A_z} \dots dA_z = \int_{\theta=0}^{2\pi} \int_{r=0}^{r_0} \dots r \, dr \, d\theta$ summation over the cross-sectional area

4

$\frac{d\gamma}{ds}$ = channel twist, change of the twist angle along the channel axis

v_x, v_y, v_z = velocity components measured within the channel bound coordinate system

v_{sx}, v_{sy} = transverse velocity components of the channel axis

$\vec{I} = I\,\vec{u}_z$ = current vector in z-direction (along axis)

$\vec{B}_0$ = applied magnetic field vector

This force $\vec{X}_\parallel$ per unit channel length is now among others a function of the local channel geometry like channel radius r_0, axis curvature R, channel twist, convergence or divergence and also a function of the channel orientation with respect to an applied magnetic field $\vec{B}_0$ and/or flow field.

In this calculation one assumes that, inside the discharge channel and in its immediate vicinity, the time derivation of the channel bound impulse density can be neglected, or that flow and pressure field adjust in a relaxation-free manner to the $\vec{j} \times \vec{B}$ forces and vice versa. This assumption, however, is valid as long as the change of the channel diameter $d(2r_0)/dt$ or the motion of the discharge channel $|v_s|$ is small compared to the average speed of sound within the considered channel segment, i.e.

$$\frac{d(2r_0)}{dt} \quad ; \quad |\vec{v}_s| \ll \bar{a} \sim \sqrt{\frac{\bar{R}\,\bar{T}}{\bar{M}}} \qquad (12)$$

The validity of this inequality can be proven from case to case and, as discussed elsewhere,[16] is fulfilled for even extreme conditions.

Based on the knowledge of $\vec{X}_\parallel$ one can now determine "balanced" and "stable" discharge channel configurations.

For a balanced current-carrying plasma channel configuration the transverse force $\vec{X}_\perp$ along the discharge axis must be zero, i.e. the gas dynamic surface forces and all body forces like electromagnetic field and fictitious forces must be mutually balanced. Such a channel configuration for instance has, according to eq. (11), a straight axis with $R = \infty$. Considering now the discharge channel that emanates from a fixed spot crater (see Fig. 11), one can define its orientation with respect to an applied magnetic field $\vec{B}_0$ by the inclination angle ξ. If the channel axis becomes slightly disturbed in any direction ϕ by a small deviation δ off its straight configuration, the axis becomes curved and the deviation or disturbance vector δ points now always in the direction of the radius of curvature vector $\vec{R}$. Disturbances by lateral motion of the electron emitting crater with respect to the discharge channel are disregarded, because any such motion is physically unrealistic, since the discharge channel must be fixed to the electron emitting hot spot. Nevertheless, many explanations of arc motion are based on such a dubious lateral effect.

By definition, such a balanced discharge channel will be called "stable" if any disturbance δ initiates a transverse force $\vec{X} = \vec{X}(\delta) \neq 0$ which acts against δ and drives the channel back in its original balanced configuration. The mathematical requirements for a balanced and stable discharge channel configuration follow therefore by

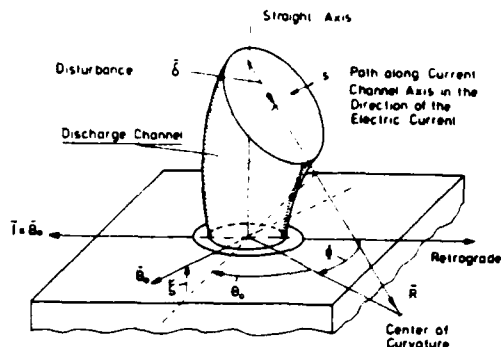$$\vec{X}_\perp \cdot \delta < 0 \qquad (13)$$

Straight Axis

Fig. 11 Illustration of a disturbed current-carrying channel at the cathode surface with inclined magnetic field.

If this requirement is not met, $\vec{X}$ acts in the direction of δ and forces the channel to deviate more and more from its balanced state.
Let us now discuss by means of this stability theory the dynamics of a spot discharge.

Spot Motion

With the introduction of the inclination angle ξ and the disturbance angle ϕ as shown in Fig. 11, the transverse force $\vec{X}_\perp$ which acts on the current-carrying plasma channel of a spot discharge can be replaced by

$$\vec{X}_\perp = -\frac{\mu_0}{8\pi}\frac{\lambda^2}{R}\left\{\varepsilon - \frac{\alpha}{\lambda}\cos\xi\,\cos\phi\right.$$

$$-\frac{r_0}{R}\left[\alpha k + \frac{3}{4}\frac{r_0}{R} - \frac{1}{4}\frac{dr_0}{ds}\frac{\beta}{\lambda}\sin\xi\right]\Big\}\frac{\vec{R}}{R}$$

$$-\frac{\mu_0}{8\pi}\frac{I^2}{R}\left\{\frac{1}{2}\frac{dr_0}{ds}\frac{1}{\lambda}\sin\xi + \frac{\alpha}{\lambda}\cos\xi\,\sin\phi\right.$$

$$+\frac{r_0}{R}\left[\beta + \frac{1}{4}\frac{dr_0}{ds}\frac{\alpha}{\lambda}\sin\xi\right]\Big\}\frac{\vec{I}\times\vec{R}}{\vec{I}\cdot\vec{R}} \qquad (14)$$

where now

$$\varepsilon = \frac{8\pi}{\mu_0}\frac{1}{I^2}\left\{\int_{A_z}\rho\,v_z^2\,dA_z - \frac{\mu_0}{8\pi}I^2\left[1 + f(n)\right]\right\} \qquad (15)$$

$$k = k(n) = (n+3)f(n)g(n) + 1 \qquad (16)$$

$$\lambda = \frac{\mu_0}{8\pi}\cdot\frac{I}{r_0 B_0} = \frac{\text{avg. self magnetic induction field}}{\text{applied magnetic induction field}}$$

Herein one assumes that any disturbance δ leads only to a bent (see Fig. 11) but not to a twisted current-carrying channel. According to eqs. (11) and (14), a straight channel (with $R \to \infty$) is again a balanced one, since $\vec{X}_\perp = 0$. As mentioned before, the direction of any disturbance δ points now in the $\vec{R}$ direction; therefore, a balanced, straight channel is also stable if the braced expression of the $\vec{R}/R$ component of $\vec{X}_\perp$ is larger than zero. Neglecting the higher order terms of r_0/R, one therefore obtains as the stability requirement

$$\varepsilon - \frac{\alpha}{\lambda}\cos\xi\,\cos\phi > 0 \qquad (17)$$

One may now distinguish between the following three cases

5

1. No applied magnetic field, $|\vec{B}_0| \sim \frac{1}{\lambda} = 0$.

2. $\vec{B}_0$ parallel to the cathode surface, $\xi = 0$.

3. $\vec{B}_0$ inclined with respect to the cathode surface, $\xi \neq 0$.

Case 1: $|B_0| \sim \frac{1}{\lambda} = 0$

In this case the stability requirement reduces to

$$\varepsilon > 0 \qquad \text{(stable)} \qquad (18)$$

which is identical with that of the MPD arc in section 3.2. Here the stability criterion does not depend on the direction of the disturbance given by ϕ (see Fig. 11). Within eq. (15) one may now relate the average impulse transport

$$\int_{A_z} \rho v_z^2 \, dA_z$$

along the channel axis with the vapor and plasma pressure p_v of the spot crater and the ambient pressure p_∞. Therefore, the stability requirement (18) can also be expressed in the form

$$P_v - P_\infty > 3.3 \frac{\mu_0}{8\pi} I_s \bar{j}_s \qquad (19)$$

where I_s is the current carried by the spot and $\bar{j}_s$ is the average current density at the crater orifice; the factor 3.3 is valid for a hemispherical crater and changes to about 3.0 for a flat crater.

The pressure difference between the vapor pressure in the spot and the ambient pressure must be therefore more than about three times larger than the average magnetic pressure ($p_M = \mu_0/8\pi \ I_s \bar{j}_s$) in order to maintain a straight, stable spot discharge. If this requirement is no longer fulfilled or if $\varepsilon < 0$, the channel becomes unstable. Any small disturbance will cause the channel to bend more and more, and eventually it will contact the cathode surface at a nearby site off the original spot (see Fig. 5). The new site is heated up and a new spot is created. Again, for this new spot, the stability requirement (18) or (19) must be fulfilled in order to maintain a balanced, stable spot. Since in this case the stability criterion does not depend on the direction of the disturbance, and since one may assume that all possible directions of δ are equally probable, the spots should move or jump statistically over the cathode surface.

Case 2: $\vec{B}_0$ parallel to the cathode surface, $\xi = 0$.

In this case, the stability criterion follows by

$$\varepsilon - \frac{\alpha}{\lambda} \cos\phi > 0 \qquad (20)$$

i.e. the channel stability depends now on the direction of the disturbance (ϕ). Moreover, the force component in the $\vec{I} \times \vec{R}$ direction of eq. (14) becomes unequal to zero in the first order. It is

$$\vec{X}_{\perp \ (\text{in } \hat{I}x\hat{R})} = - \frac{\mu_0}{8\pi} \frac{I^2}{R} \frac{\alpha}{\lambda} \sin\phi \ \frac{\hat{I}x\hat{R}}{\hat{I}\cdot\hat{R}} \qquad (21)$$

For $\alpha > 0$, i.e. the current density maximum is shifted towards the center of curvature, the channel is less likely to be stable for any disturbance towards the retrograde side $-\pi/2 < \phi < +\pi/2$ than for a disturbance towards the amperian side $\pi/2 < \phi < 3\pi/2$ (or $-\pi/2 > \phi > -3\pi/2$) which can be verified by means of criterium (20). For any disturbed or curved channel, there acts now a force in the $\vec{I} \times \vec{R}$ direction [eq. (14)] such that the curved channel always turns into the retrograde direction, i.e. δ points finally in the opposite $\vec{I} \times \vec{B}_0$ direction. The channel therefore becomes preferably un-

stable by bending more and more in the retrograde direction.

For $\alpha < 0$, the current density maximum is shifted away from the center of curvature maximum towards the convex side of the channel. According to criteria (20) and eq. (21), the channel should now bend preferably in the amperian direction. One can, however, show that by accounting for the higher order term $(r_0/R)\alpha k$ in eq. (14), the channel this time assumes a curved, stable configuration. The possible consequence of this behavior shows that the channel does not come in contact with the cathode surface on the amperian side of the spot. This is not the case for a retrograde disturbance with $\alpha > 0$, for which the channel is unstable and bends more and more. Observable current channels should therefore be amperically bent or straight while the observation of a retrograde channel configuration would require high time resolutions.

In conclusion to Case 2, a spot prefers to jump or move either in the retrograde or the amperian direction, depending on whether the current density maximum is shifted towards the concave or the convex side of the discharge channel. Because of the unstable channel behavior during retrograde motion and the stable, bent channel behavior during amperian motion, one may conclude that the average jump distance is smaller and the number of jumps more frequent for the retrograde moving spots than for the amperian moving ones. For large magnetic fields ($\lambda k \ll 1$, which means about $B_0 \gg 1$ Tesla for an experimental value[18] of $I/r_0 = 10^7$ A/m) the mechanisms for amperian and retrograde spot motion are practically identical and therefore in both directions equally probable.

Case 3: $\vec{B}_0$ inclined with respect to the cathode surface, $\xi \neq 0$.

According to eq. (20) the current channel is preferably unstable with respect to a disturbance in the retrograde direction and assumes a bent but stable configuration for an amperian disturbance. The principle difference now is given through the force component in the $\vec{I} \times \vec{R}$ direction, which in the first order of r_0/R follows by

$$\vec{X}_{\perp \ (\text{in } \hat{I}x\hat{R})} = - \frac{\mu_0}{8\pi} \frac{I^2}{R} \left\{ \frac{1}{2} \frac{dr_0}{ds} \frac{1}{\lambda} \sin\xi \right.$$

$$\left. + \frac{\alpha}{\lambda} \cos\xi \ \sin\phi \right\} \frac{\hat{I}x\hat{R}}{\hat{I}\cdot\hat{R}} \qquad (22)$$

and which turns the disturbed or curved channel around its original straight axis either in the retrograde ($\alpha > 0$) or amperian direction ($\alpha < 0$). Now, however, the disturbance δ finally does not point exactly in these directions but deviates or drifts away from that. The drift angle follows from the requirement that for this position the turning force in the $\vec{I} \times \vec{R}$ direction must be zero. From eq. (22) follows therefore

$$\sin\phi_{\text{drift}} = - \frac{1}{2\alpha} \frac{dr_0}{ds} \tan\xi \qquad (23)$$

For a spot motion towards the retrograde side it is $\alpha > 0$, and since the channel in the direction of the current is supposed to converge ($dr_0/ds < 0$), the drift angle ϕ_{drift} is proportional to ξ as long as the angles are small. The retrograde moving spots drift, therefore, under a small angle with respect to the proper retrograde direction towards the right (in the direction of $\vec{B}_0$) if the $\vec{B}_0$ field points upward, and drifts towards the left (opposite to $\vec{B}_0$) if the field vector points downward (see Fig. 12a,b). This spot behavior has been experimentally observed and as mentioned before is known as Robson drift motion.[14,15]
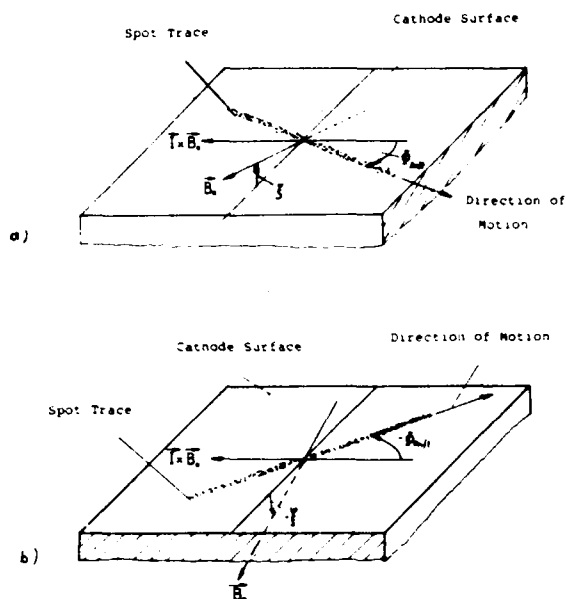
6

Fig. 12 Retrograde spot motion with an inclined $\vec{B}_0$ field.

Discussion

Let us consider the cathode attachment of an MPD arc, consisting of many active spots which are somehow distributed over the cathode surface, as shown for instance in Fig. 13. Any single spot is now affected by all the other ones such that a magnetic field acts on it. Assume now that all the spots are statistically homogeneously distributed around and along the cathode surface. In this case the magnetic induction field is azimuthal and depends on how much current is drawn by the spots downstream of the considered spot.
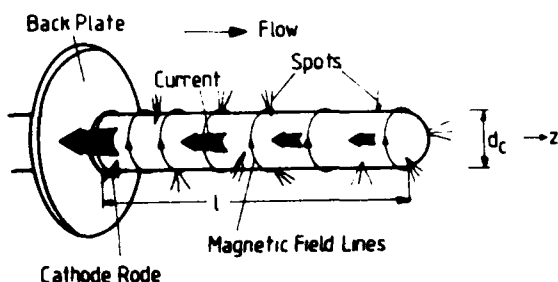

Fig. 13 Scheme of the spotty arc cathode attachment.

For a cathode rod of length 1 and diameter d_c covered statistically by many spots, the current through the rod at any distance z from the backplate follows by

$$I(z) = \frac{I}{1 + \frac{1}{2}\frac{d_c}{l}} \left(1 - \frac{z}{l} + \frac{1}{2}\frac{d_c}{l}\right)$$

where I is the total current, d_c is the cathode diameter, 1 is the length of the rod and z is the distance from the backplate.

Therefore the azimuthal magnetic induction field for a spot at a distance z from the backplate is about

$$B_0 = \frac{\mu_0}{\pi}\frac{I}{d_z}\frac{1 - \frac{z}{l} + \frac{1}{2}\frac{d_c}{l}}{1 + \frac{1}{2}\frac{d_c}{l}}$$

This has the consequence that B_0 decreases downstream. For any spot, therefore, one has to take into account a transverse magnetic field. The consequence of such a field, as shown in the previous section under "Case 2", is a preferred motion of the spots in the retrograde or upstream direction. With increasing magnetic field the quotient λ in eq. (17) decreases, which leads to an enhancement of the instability behavior and therefore to a faster spot motion. Since the crater size of fast moving spots can be expected to be smaller than that of slowly moving ones, the spot size should increase towards the cathode tip. This has been observed[19] in seemingly diffuse cathode attachments and indicates that possibly all attachment mechanisms are spotty and locally highly unstable.[20]

In summarizing the consequences on plasma thruster cathodes the following should be noted.

• A cathode spot is the more stable and sticks preferably to that area where the vapor pressure of the cathode material is high. Since insulator material outgases or evaporates easier than the thoriated tungsten rod cathode, the arc attachment usually sticks to the boundary cathode insulator, or cathode backplate.

• Within a magnetic field parallel to the cathode surface, an individual spot jumps preferably in the retrograde direction, i.e. upstream.

• The jump distances of the retrograde moving spots are smaller than that of the amperian moving ones.

• If the magnetic field lines are inclined with respect to the cathode surface, the spots drift away from the retrograde direction.

• The upstream boundary of a seemingly diffuse arc attachment depends on the conditions under which retrograde arc spot motion ceases. Those conditions are not fully known today.

• While the current-carrying channel of a spot discharge in a transverse magnetic field may bend and eventually move discontinuously in the retrograde direction, the plasma jet is deflected in the amperian direction and may cause a bright layer along the cathode rod. In this layer, evaporated cathode material should be present.

References

[1] Harris, L. P., "Arc Cathode Phenomena," Contribution in "Vacuum Arcs Theory and Application," J. M. Lafferty, ed., John Wiley & Sons, New York, 1980

[2] Stark, J., "Induktionserscheinungen am Quecksilberlichtbogen im Magnetfeld," Zeitschrift für Physik, Band 4, p. 440, 1903

[3] Eidinger, A. and Rieder, W., "Verhalten des Lichtbogens im transversalen Magnetfeld," Archiv für Elektrotechnik, Vol. XLIII, No. 2, p. 94, 1957

[4] Myers, T. W. and Roman, W. C., "Survey of Investigations of Electric Arc Interactions with Magnetic and Aerodynamic Fields," Aerospace Research Laboratory, USAF Technical Report 66-0184, 1966

[5] Ecker, G. and Müller, K. G., "Theorie der Retrograde Motion," Zeitschrift für Physik, Band 151, p. 577, 1958

[6] Weichel, H., "On the Retrograde Motion of a Low Pressure Arc Discharge in a Transverse Magnetic Field," M.S. Thesis, Air Force Institute of Technology, Air University, Dayton, OH, June 1965

[7] Hermoch, V. and Teichmann, J., "Cathode Jets and the Retrograde Motion of Arcs in Magnetic Fields," Zeitschrift für Physik, Band 195, p. 125, 1966

[8] Mailänder, M., Procedures of 11th International Conference on Ionization Phenomena in Gases, p. 81, Prague, 1973

[9] Rakhovskii, V. I., "Experimental Study of the Dynamics of Cathode Spots Development," IEEE – Transactions on Plasma Science Vol. PS – 4, No. 2, p. 81, 1976

[10] Drouet, M. G., "The Physics of the Retrograde Motion of the Electric Arc," Japanese Journal of Applied Physics Vol. 20, No. 6, p. 1027, 1981

[11] Harris, L. P., "Motions at Cathode Spots in Vacuum Arcs," IEEE Transactions on Plasma Science, Vol. PS 11, p. 94, 1983

[12] Smith, C. G., Physical Review, Vol. 69, p. 96, 1946

[13] Kesaev, I. G., Zhurn Tech. Phys., Vol. 29, p. 287, 1959

[14] Robson, A. E., "The Motion of an Arc in a Magnetic Field," Procedures of the Fourth International Conference on Ionization Phenomena in Gases, Vol. IIB, p. 346, August 1959

[15] Hintze, W. and Laux, M., "On the Motion of Unipolar Arcs in a Tokamak," Beiträge aus Plasmaphysik, Band 21, Heft 4, 247, 1981

[16] Schrade, H. O., "Magnetoplasmadynamic Effects in Electric Arcs," Interim Scientific Report, Grant AFOSR 82 – 0298, August 1983

[17] Schrade, H. O., Auweter-Kurtz, M. and Kurtz, H. L. "Analysis of the Cathode Spot of Metal Vapor Arcs," IEEE Transactions on Plasma Science, Vol. PS-11, No. 3, p. 103, 1983

[18] Datlov, J. P., Guile, A. E. and Jüttner, B., "Unipolar Arc Tracks on Stainless Steel," Beiträge aus Plasmaphysik, Vol. 21, p. 135, 1980.

[19] Private Communication: Observations of R. G. Jahn, A. J. Kelly and H. O. Schrade on cathodes of continuously running MPD thrusters.

[20] Schrade, H. O., Auweter-Kurtz, M. and Kurtz, H. L., "Cathode Erosion Studies on MPD Thrusters," AIAA 85-2019, 18th Electric Propulsion Conference, Alexandria, VA, 1985

8

6.3 <u>Appendix III</u>

Numerical Modeling of the Flow Discharge in MPD Thrusters

AIAA'87

AIAA-87-1091

Numerical Modeling of the Flow Discharge in MPD Thrusters

M. Auweter-Kurtz, H. L. Kurtz, H. O. Schrade and P. C. Sleziona

Universität Stuttgart, Stuttgart, FRG

AIAA/JSASS/DGLR 19th International Electric Propulsion Conference

May 11-13, 1987 / Colorado Springs, Colorado

NUMERICAL MODELING OF THE FLOW DISCHARGE IN MPD THRUSTERS

M. Auweter-Kurtz, H. L. Kurtz, H. O. Schrade and P. C. Sleziona

Institut für Raumfahrtsysteme
Universität Stuttgart
Federal Republic of Germany

Abstract

Two theoretical models for calculating the current
and flow distributions in self-field MPD thrusters
are being developed and will be applied to evaluate
the effects of geometry, propellant type, scale and
other parameters on the thruster performance.

1) For continuous thrusters, a stationary code is
being developed. The extended Ohm's law is used
to calculate the current contour lines, and a
one-dimensional, two-component expansion flow
model is used to obtain the velocity, tempera-
ture and pressure distributions for calculating
the gas properties, which are again used in
Ohm's law. The differential equation is solved
by means of a finite difference method for tne
geometry of the nozzle-type plasma thruster DT2,
which has been investigated at IRS in a steady
state as well as in a quasi-steady state mode.

An integration over the volume and thermal
forces equals to the thrust. The calculated cur-
rent density distribution and the computed
thrust are compared with experimental results.

2) For tne starting phase of the steady state MPD
thrusters as well as for pulsed thrusters, a
time dependent, fully two-dimensional code is
being developed. It uses a modified McCormack FD
method in cylindrical coordinates to calculate
the time dependent flow, temperature and pres-
sure fields. The current and magnetic contour
lines, which must be known for the energy and
impulse input in this code, are calculated with
an instationary Ohm's law solved in a manner
similar to the computer code for continuous
thrusters. This code is used for a simplified
cylindrical thruster model.

For both methods the results are discussed.

1. Introduction

The increase in onboard electrical power in the
near future is again raising interest in self-field
MPD thrusters. Despite their simplicity in design
and power conditioning, they are handicapped even
today by the shortcomings of low efficiency and a
performance limit known as "onset" which restricts
the flow rate at a given current value. Therefore,
since the beginning of the design and investigation
of self-field MPD thrusters at the end of the six-
ties, effort has been made to unterstand the phys-
ics of the MPD discharge and the development of ap-
propriate codes. But the MPD problems cannot be
solved easily, because in contrast to the hardware
simplicity of these devices, the physics involved
are of extreme complexity. To mention only a few:
real gas effects, i.e. cold propellant is heated up
in an arc and the gas has to be dissociated and
ionized; the problems related with the electrodes
are only partly known or solved; the plasma is in a
thermal non-equilibrium; because of the low densi-
ties and high temperatures the Reynold's numbers
are low and the friction cannot be neglected; the
magnetic Reynold's number is too high to separate
flow and discharge; etc. This list is by no means a
complete one. Added to these physical complexities
are numerical difficulties: the necessary coupling
of different partial differential equation systems,

namely elliptical and hyperbolic ones; non-linearí-
ties; steep gradients; and so on. And let us not
forget difficult geometries. Therefore, due to the
great complexity of the physical conditions, for
all codes established to solve at least parts of
these problems, many and great simplifications must
be made. The resulting codes include for example
one-dimensional[1,2], quasi-two-dimensional and sim-
plified two-dimensional ones[3,4].

In this paper, two further approaches are present-
ed: first, a partly two-dimensional one. The sim-
plified, two-dimensional electromagnetic calcula-
tion follows from Ohm's law, similar to Ref. 5, and
the flow is modeled by a one-dimensional, non-equi-
librium expansion. The equations are solved only
for the steady phase. The second approach uses com-
parable electromagnetic equations, but models the
flow actually two-dimensionally with a modified
MacCormack code. Both approaches neglect electrode
effects and friction.

2. Steady-State MPD Thruster Investigations

In order to predict the overall performance of con-
tinuously running, self-field MPD thrusters, a
semi-two-dimensional model calculation and computer
program has been developed.[8,9] In a first step this
program has been used to investigate the current
contour lines and the thrust within the nozzle-type
thruster DT2 (Fig. 2.1), which is being developed
at this institute.[10]

2.1 Current Contour Lines

In this approach, the current contour lines are
calculated in r- and z- dependence while the flow
field is taken as a one-dimensional, frictionless
expansion flow, assuming isothermal behavior for
the electron component and isentropic expansion for
the heavy particles like ions and neutrals. This
assumption is justified, since primarily the elec-
tron component is heated by Ohmic energy input, and
since within the nozzle expansion flow the energy
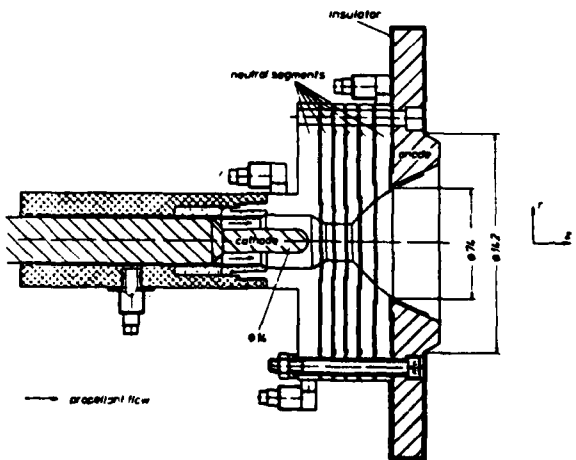exchange between the lightweight electrons and the

Fig. 2.1 Self-field nozzle-type MPD thruster DT2
(capacity about 5 kA or 15 N thrust with argon).

heavy particles like ions and neutrals is fairly weak. Therefore, reaction collisions (ionization and recombination processes, etc.) are neglected. Hence, the model approach distinguishes between electron and heavy particle temperatures and assumes a frozen flow from the nozzle throat on downstream.

Within the nozzle throat, one assumes a "fully developed" arc flow regime, i.e. the gas and plasma velocity and the current density vector have only an axial component and the arc column is defined by only radial heat transfer (and possibly by radial radiation) losses. Moreover, from the nozzle throat on upstream, one no longer distinguishes between electron and heavy particle temperatures, since within this higher pressure regime a tight coupling between all components is more likely to be established than in the low pressure downstream nozzle regime. In spite of the neglect of the radial dependency of the flow and species temperatures, however, this model approach turns out to be an effective tool for predicting the current contour lines within and the thrust and specific impulse of a nozzle-type self-field MPD thruster.

Assumptions:

- steady state conditions
- rotational symmetry
- no azimuthal current
- singly ionized, quasi-neutral plasma
- electric current density normal to electrode surfaces
- from cathode to nozzle throat: thermal equilibrium
- within the nozzle: frozen flow, ambipolar expansion flow without friction, electrons: isothermal, ions: adiabatic
- outside the nozzle: hyperbolic expansion flow, electrons and ions adiabatic

Basic Equations:

Maxwell's eqs.:

$$\vec{\nabla} \times \vec{B} = \mu_0 \vec{j} \qquad 2.1$$

$$\nabla \times \vec{E} = -\frac{\partial \vec{B}}{\partial t} = 0 \qquad 2.2$$

$$\nabla \cdot \vec{B} = 0 \qquad 2.3$$

$$\nabla \cdot \vec{E} = 0 \qquad 2.4$$

Ohm's Law:

$$\vec{j} = \sigma \{ \vec{E} + \vec{v} \times \vec{B} \} - \frac{\omega \tau}{B} [\vec{j} \times \vec{B}] \qquad 2.5$$

Equation of State:

$$p = \rho \frac{k}{m_0} T_t \left\{ 1 + \left(\frac{\rho}{\rho_t} \right)^{\kappa-1} \right\} \qquad 2.6$$

Continuity Equation: $\rho v A = \rho_t A_t v_t = \dot{m}$ 2.7

Expansion Relation:

$$\left(\frac{v}{v_t} \right)^2 = 1 + \ln \left| \frac{A}{A_t} \frac{v}{v_t} \right|$$

$$+ \frac{\kappa}{\kappa-1} \left[1 - \left(\frac{A_t}{A} \frac{v_t}{v} \right)^{\kappa-1} \right]$$

$$+ \frac{2}{\dot{m} v_t} \int_{z_t}^{z} \left(\frac{v}{v_t} \right) (\vec{j} \times \vec{B})_z A\, dz \qquad 2.8$$

Nozzle Throat Conditions:

$$v_t^2 = \left(\frac{\partial p}{\partial \rho} \right)_{t,isoth} = 2 \frac{k}{m_0} T_t \qquad 2.9$$

$$T_t = T_e = f \cdot \left(\frac{I}{r_t} \right)^{2/5} \qquad 2.10$$

where f is a slowly varying function depending on current distribution.

The last three equations are derived in detail under the above assumptions in Ref. 8.

Rewriting Ohm's Law by means of Maxwell's equations, one obtains a vector equation for the magnetic induction vector $\vec{B}$ in the form

$$-\frac{\partial \vec{B}}{\partial t} = \frac{1}{\mu_0} \text{rot} \left(\frac{1}{\sigma} \text{rot}\, \vec{B} \right) - \text{rot}\, [\vec{v} \times \vec{B}]$$

$$+ \frac{1}{\mu_0} \text{rot}\, [\beta\, (\text{rot}\, \vec{B}) \times \vec{B}] = 0 \qquad 2.11$$

with $\quad \beta = \frac{\omega \tau}{B \sigma} = \frac{1}{e n_e} \qquad 2.12$

For a stream function

$$\Psi = r B_\theta$$

with respect to the rotational symmetry and the zero azimuthal current, the elliptic, partial differential equation of 2nd order follows from eq. 2.11 in the form

$$\frac{d^2 \Psi}{dr^2} + \frac{d^2 \Psi}{dz^2} - \frac{d\Psi}{dr} \left(\frac{1}{r} + \frac{1}{\sigma} \frac{d\sigma}{dr} - \frac{\sigma \Psi}{r} \frac{d\beta}{dz} + \sigma \mu_0 v_r \right)$$

$$- \frac{d\Psi}{dz} \left(\frac{1}{\sigma} \frac{d\sigma}{dz} + \frac{\sigma \Psi}{r} \frac{d\beta}{dr} - \frac{2\sigma\beta\Psi}{r^2} + \sigma \mu_0 v_z \right)$$

$$- \sigma \mu_0 \Psi \left(\frac{dv_r}{dr} + \frac{dv_z}{dz} - \frac{v_r}{r} \right) = 0 \qquad 2.13$$

The function $\Psi(r,z) = \text{const.}$ represents now a current contour line, since $B = B_\theta \sim I(r)/r$ and $I(r)$ is the electric current carried through a cross sectional area of πr^2. The proper boundary conditions for Ψ follow from the geometry of the thruster walls and electrodes.

A solution of the equation system 2.1 – 2.13 requires as input data:

- Geometry of Thruster $A(z)$
- Mass Flow Rate $\dot{m}$
- Electric Current I

and yields the following results:

- Current Contour Lines
- Thrust, $\vec{T}$
- Specific Impulse, I_{sp}

Step 1: By setting the integral

$$\int_{z_t}^{z} \left(\frac{v}{v_t} \right) (\vec{j} \times \vec{B})_z A\, dz$$

in the expansion relation eq. 2.8 to zero, one obtains together with the nozzle throat conditions 2.9 and 2.10 a first approximation of $v(z)$, $p(z)$, $\rho(z)$ and $n_i(z) = n_e(z)$ within the nozzle. Outside the nozzle one assumes a hyperbolic expansion flow, which means $v_t \neq 0$ (Fig. 2.2).

With the knowledge of the flow and plasma properties (in first approximation), σ, β and v are also known, as well as their
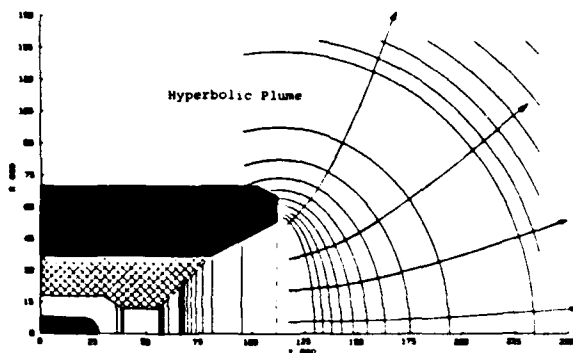
2

Fig. 2.2 Scheme of the density model.
Inside the nozzle: one-dimensional.
Outside the nozzle: elliptical.

derivatives. With these quantities one now solves the differential equation 2.13 by means of a finite differential method (Gauss-Seidel) for the current contour lines in first approximation. In Fig. 2.3 the current contour lines are shown for different currents between 1.3 and 4 kA. According to Maxwell's equation, one also obtains from ∇ the current density and the $\vec{j} \times \vec{B}$ force configuration within the discharge.

Step 2: One solves the expansion relation (eq. 2.8) numerically by taking $(\vec{j} \times \vec{B})_z$ within within the integral from Step 1. With that the velocity v(z) and the quantities p(z), $\rho(z)$, $n_e(z)$ are calculated in second order approximation and from that the new quantities for σ, β and v with their derivatives.
With these new quantities, one now solves the differential equation 2.13 for the current contour lines by means of the same numerical method as in Step 1. Repeating Step 2 yields an iterative solution of the equation system 2.1 - 2.10.
The calculation shows that after two steps the current contour lines with I = 4 kA do not change anymore and even a first step approach gives good results. For lower current rates the deviation is even smaller.

A comparison between calculated and measured current pattern (Fig. 2.4) shows a fairly good agreement. The fact that in the measured case the anode attachment is more concentrated downstream of the nozzle end than in the calculated case may be attributed to the theoretical model which neglects the boundary layer along the nozzle and anode walls.

2.2 Thrust

According to the known $\vec{j} \times \vec{B}$ force configuration and the flow conditions, one can now calculate the thrust.
The thrust of a self-field MPD accelerator is composed of two effects; first the sum of all gas-dynamic surface forces on the inner plenum chamber and on the inner nozzle wall, and second the sum of all volume effects given by the magnetic field forces which act between the current-carrying plasma and the entire power circuit, including the coaxial electrodes. Hence it is

$$\vec{T} = \int_{A_s} (\rho \vec{v}\vec{v} + \vec{P}) \cdot d\vec{A} - \int_V \vec{j} \times \vec{B}\, dV \qquad 2.14a$$

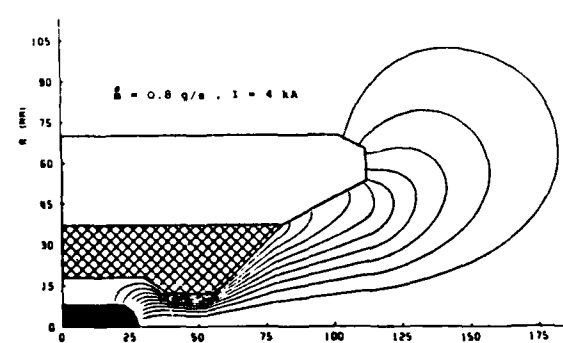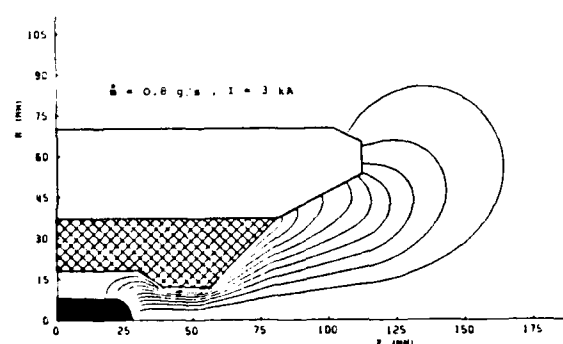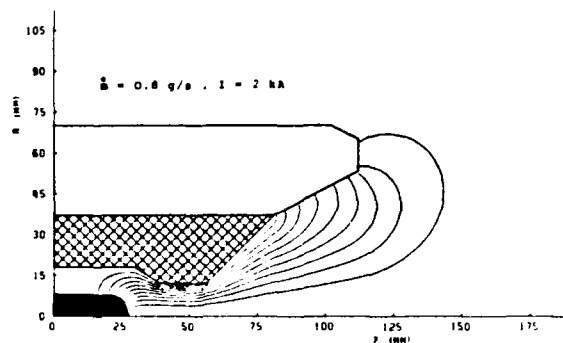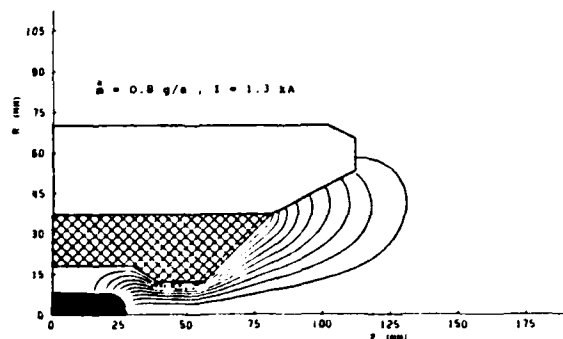$$= c_T \, p_0 A_t - \int_V \vec{j} \times \vec{B}\, dV \qquad 2.14b$$

Fig. 2.3 Current contour lines for different currents with a mass flow of 0.8 g/s.

where $(\rho \vec{v}\vec{v} + \vec{P})$ is the gas dynamic force per unit area; A_s represents the surface of all internal walls like plenum chamber with the gas inlet cross sections, the cathode surface and the inner solid wall of the nozzle; V is the current-carrying volume. The second term is the sum over all $\vec{j} \times \vec{B}$ forces which act between the current-carrying solid leads of the electric power circuit and the current-carrying plasma; in the second equation p_0 is the chamber pressure, A_t the nozzle throat area and c_{Th} the thrust coefficient matching the gas dynamic effects. It is by definition
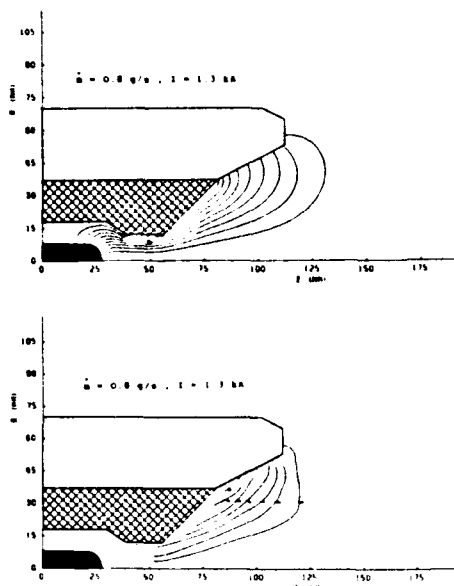
3

Fig. 2.4 a) Calculated and b) measured current contour lines of the MPD discharge in the nozzle type DT2-IRS thruster for I = 1,3 kA and m = 0.8 g/s argon.

$$c_T = \frac{1}{\rho_0 A_t} \int_{A_s} \{\rho \vec{v}\vec{v} + \overset{\leftrightarrow}{P}\} \cdot d\vec{A} \qquad 2.15$$

The calculated thrust, based on the current density and magnetic field determined with the procedure as described in section 2.1, is now compared with the experimental results in Fig. 2.5.
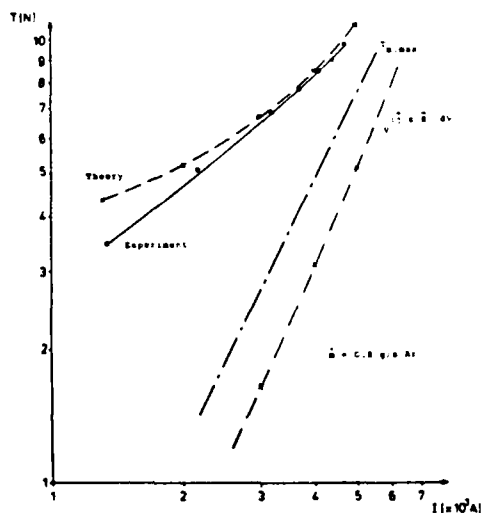

Fig. 2.5 Comparison between calculated and measured thrust of the DT2-IRS thruster. $T_{m,max}$ is the maximum possible electromagnetic thrust.

They show excellent agreement for $c_T = 1$ with the experimental measurements in the upper current range (I > 3000 A), and even down to 1300 A the deviation is less than 30%. The pure electromagnetic thrust is given by the lower curve in Fig. 2.5. One can see that the electromagnetic thrust reaches about 50% of the total thrust at a current of about 4500 A.

3. Time Dependent, Two-Dimensional MPD Thruster Investigations

In addition to the steady state MPD theory, a real two-dimensional numerical code has been developed.[11] This code allows the calculation of the time dependent plasma properties during the starting phase of steady state MPD thrusters, as well as for pulsed mode thrusters. The numerical solution is done in a manner similar to that of Jacobi[12] for laser applications. In a first approach, this MPD code was applied to the cylindrical MPD thruster ZT1 being developed at this institute.[10] Fig. 3.1 shows the drawing of ZT1, and Fig. 3.2 shows the corresponding simplified scheme for the calculation.
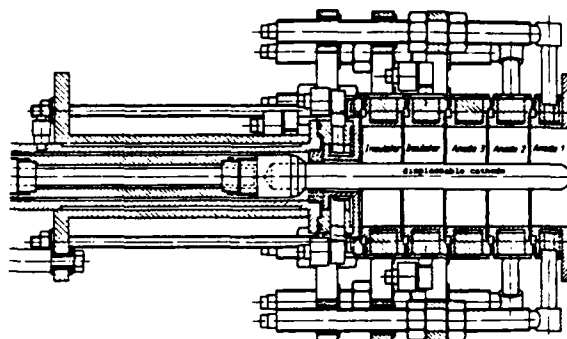

Fig. 3.1 Cylindrical continuous MPD thruster ZT1-IRS.
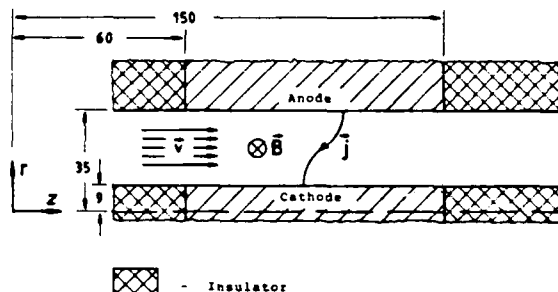

$\boxtimes$ - Insulator

Bild 3.2 Simplified scheme used for the calculation.

The geometrical configuration on which the computation is based was chosen as close as possible to the experimental device. The radii of cathode and anode are taken according to the dimensions of the real device; however, the length of the cathode is assumed to be of the same length as the anode and it matches the length of the three anode segments (see Fig. 3.1). The model is assumed to be an infinite tube of an insulator with a central insulating rod, only the electrodes will be of zero resistance.

For the time dependent calculation of the MPD flow, two independent codes were correlated to determine flow field, current and magnetic field distribution. These two codes are connected in the following manner: for a given flow field, the current, and hence the magnetic field distribution, was determined. With these results the flow field equations were integrated. In the next time step, this new flow field and the new distribution of the thermal properties were taken to calculate the new electromagnetic field distribution, and so on.

As input data the two codes require:
• geometry of the thruster
• mass flow rate
• electric current as a function of time

and at the starting point:
- temperature field
- Mach number.

This yields the following time dependent results:
- flow
- temperature
- pressure
- Mach number
- magnetic field
- current density distribution within the channel
- electrothermal thrust.

3.1 Electromagnetic Code

The electromagnetic properties are obtained in a similar manner as from the steady state thruster code, using the following assumptions:
- rotational symmetry
- no azimuthal current
- electric field normal to the electrode surfaces.

One solves Ohm's law with respect to Maxwell's equations; this means one must solve the elliptic partial differential equation 2.13.

The boundary conditions are as follows:
On the insulator surface and at the boundary of the integration area, the stream function Ψ equals zero for the case of the downstream insulator and equals Ψ_{max} for the upstream insulator. At the electrodes the boundary condition follows from the requirement that the electric field E must be perpendicular to the surface. This means for a cylindrical channel as considered here that at the electrode surfaces E_z equals zero. Therefore, the boundary condition follows to

$$\frac{1}{\sigma\mu_0 r}\frac{\partial\Psi}{\partial r} - v_r\frac{\Psi}{r} - \frac{\beta\Psi}{\mu_0 r^2}\frac{\partial\Psi}{\partial z} = 0 \qquad 3.1$$

With this closed boundary condition, the computation has been done with a Gauss-Seidel code and yields as a result the magnetic field and the current density distribution within the channel.

3.2 Flow Field Code

For the description of the time-dependent, two-dimensional, supersonic, ohmically heated flow the conservation equations for mass, impulse and energy were used with the following assumptions:
- friction free flow
- rotational symmetry
- no azimuthal current and velocity
- supersonic flow within the channel

The conservation theorem formulation was chosen in order to satisfy the Rankin-Hugoniot shock conditions implicity; hence the description of shock depth and shock velocity are very good. These considerations yield the following non-linear hyperbolic differential equation system with cylindrical coordinates

$$\begin{vmatrix}\rho \\ \rho v_r \\ \rho v_z \\ e\end{vmatrix}_t + \begin{vmatrix}\rho v_r \\ p + \rho v_r^2 \\ \rho v_r v_z \\ (p+e)v_r\end{vmatrix}_r + \begin{vmatrix}\rho v_z \\ \rho v_z v_r \\ p + \rho v_z^2 \\ (p+e)v_z\end{vmatrix}_z + \begin{vmatrix}\rho v_r/r \\ \rho v_r^2/r - j_z \times B_\theta \\ \rho v_r v_z/r - j_r \times B_\theta \\ (p+e)\frac{v_r}{r} - j^2/\sigma\end{vmatrix} = 0$$

$$3.2$$

where the indices $||_t$, $||_r$, $||_z$ indicate the partial differentiation with respect to time and to the r- and z-directions.

Boundary Conditions:

upstream: at that boundary all flow parameters are assumed to be constant and must be set.

downstream: here the flow parameters are extrapolated because of the calculated field parameters.

at the side: no normal velocity; normal differentiations equal zero.

Initial conditions:
At $t = 0$ the flow parameters equal the undisturbed parallel flow; uniform current density; Mach number and temperature must be set.

For the numerical solution a modified MacCormack code was used; this is an explicit code of second order which uses the shock capturing method. It allows a fairly high energy input into the flow due to ohmic heating and a steep rise in the impulse due to $j \times B$ forces. Because of instabilities at the starting phase caused by initial and boundary conditions on the upstream boundary, the initial conditions will be restricted for the moment to values which result in cowling numbers smaller than 1.5 in the middle of the electrodes.

For the example presented, the calculation is based on the following initial values: $T(0) = 8000$ K, $Ma(0) = 1.2$, with a mass flow of 20 g/s argon. The current as a function of time is taken as a sine square function $\sin^2[\pi t/2t_0]$ rising from $I(t=0) = 0$ to $I(t_0=200\mu s) = 12$ kA and is taken as constant from there on.
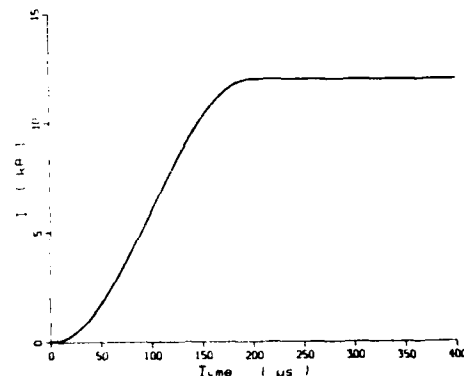

Fig. 3.3 Current curve versus time.

With this input data the computation yields the time dependent current density distribution, as illustrated in Fig. 3.4. Starting with radially parallel and homogeneous current contour lines at $t = 0$, the current is driven more and more downstream--stronger near the anode than at the cathode--and bulges at the electrode ends. The dotted lines are those at 20 μs after starting, and the dashed and solid lines are for 160 μs and 200 μs, respectively.
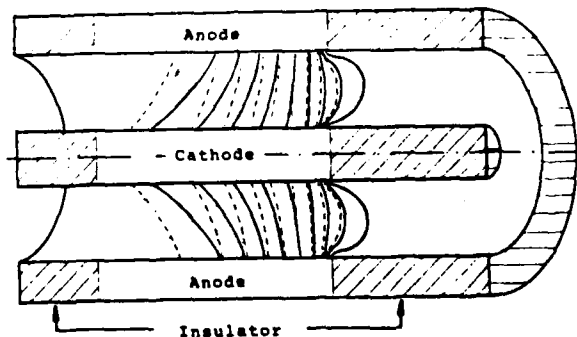

Fig. 3.4 Calculated current contour lines in a cylindrical MPD thruster. Dotted lines at t = 20 μs, dashed after 160 μs and solid after 200 μs.

5

Fig. 3.5 illustrates the temperature distribution 100 μs and 200 μs after starting. The strong rise in temperature near the electrode is caused by ohmic heating due to the relatively high current density there. The disturbance at the cathode end due to discontinuous boundary conditions decreases with time. This fairly marked disturbance at starting is one reason for choosing a high initial temperature.
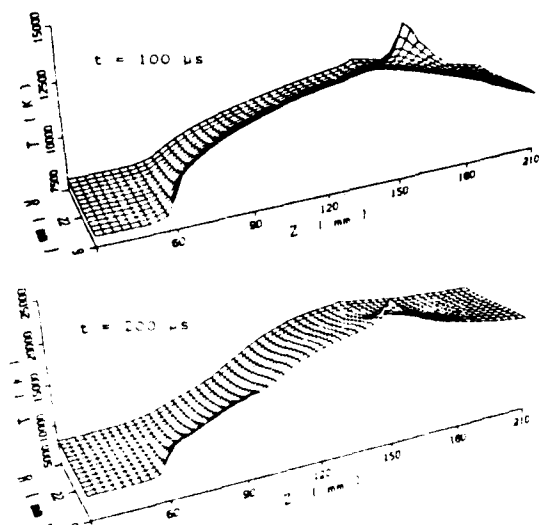
The axial and radial velocity distribution at 200 μs are plotted in Fig. 3.7. At both ends of the cathode there is a steep rise in the radial velocity v_r, while the axial velocity reaches its maximum at the beginning of the cathode. The axial velocity decreases towards the cathode end, with a low rise from this point downstream as well as towards the anode.

Fig. 3.7 Velocity distribution at 200 μs. a) Axial velocity v_z, b) radial velocity v_r.

Fig. 3.5 Temperature distribution within the channel at a) 100 μs, b) 200 μs.

A radial shock front formed at the end of the electrodes moves upstream while lowering its intensity; this is demonstrated in Fig. 3.6.
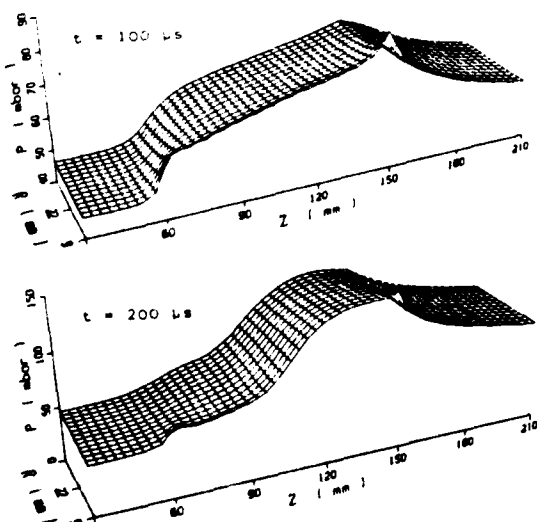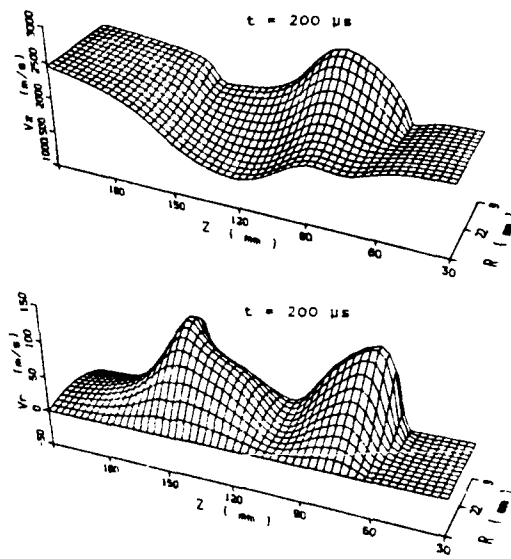
The relationship of the Mach number distribution to the temperature and velocity distribution at 200 μs is shown in Fig. 3.8. The Mach number set equal to 1.2 at the upstream boundary reaches an initial maximum at the beginning of the cathode, rises again while reaching an interim maximum at about 1/3 of the cathode length and rises once more behind the electrodes. The minimum at the end of the cathode is caused by the temperature instability at that point. It is remarkable that the Mach number is below 1 within a wide range, especially before the end of the electrodes.
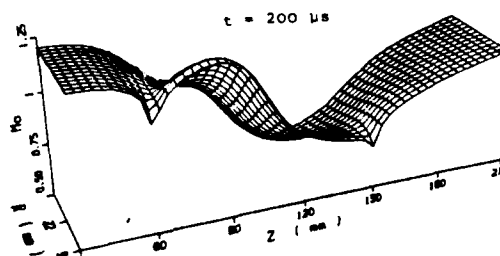

Fig. 3.8 Mach number distribution at 200 μs.

As described in section 2.2, the thrust is composed of an MPD part and a gas dynamic part (see eq. 2.14a). The pure MPD thrust can be calculated by an integration of the $\vec{j} \times \vec{B}$ forces within the entire current-carrying volume; another possibility is to use the well-known formula[13]

$$T_{max} = \frac{\mu_0 I^2}{4\pi} \ln \frac{r_A}{r_c} \qquad 3.3$$

Fig. 3.6 Pressure distribution within the channel at a) 100 μs, b) 200 μs.

6

where r_A/r_C is the anode to cathode ratio. Both have been done for the example described here with a coincidence of within 1%.

In Fig. 3.9 the pure MPD thrust (dashed line) and the total thrust (solid line) are plotted depending on time. The total calculated thrust at 400 µs lies within a 3% deviation from the expected thrust.
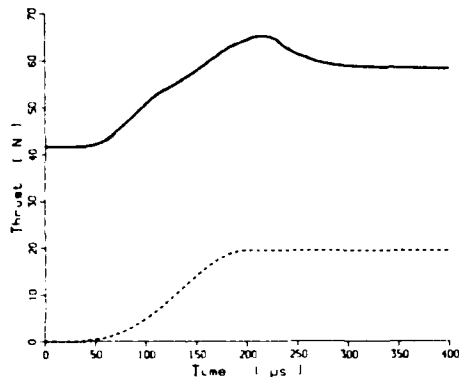

Fig. 3.9 Thrust versus time. Solid line: total thrust. Dashed line: electromagnetic thrust.

Even more troublesome is the fact that the conservation of mass is only valid within a 10% range. Fig. 3.10 shows the mass flow versus time at four different channel cross sections.
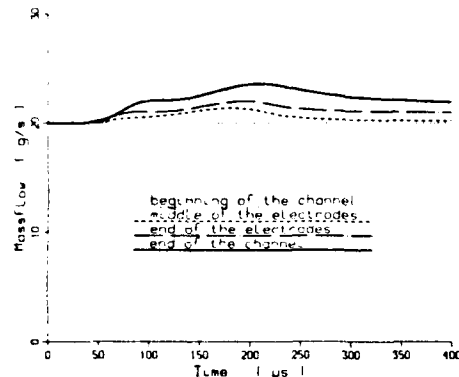

Fig. 3.10 Mass flow versus time at different channel cross sections.

These deviations from the mass conservation law are an inherent attribute of the MacCormack code.

Concluding Remarks

In order to gain a more profound understanding of the fundamental process occuring in MPD thrusters and in order to eventually end up with reliable design criteria and predict thruster performances under various conditions, the two codes described within this paper have been developed.

One was developed for the steady state condition and the other for the time dependent description of MPD thrusters. The first code was tested with the DT2-IRS thruster design, and it produced fairly good results; especially the current density distribution agrees quite well with the measurements. The time dependent code tested with the cylindrical thruster design of the ZT1-IRS thruster produced fairly good results as well. Both codes have weak points, for example the boundary conditions, real gas effects, and geometry modeling. Especially the second code was weak in terms of mass conservation.

In a later research period the physical models must be refined, and other numerical flow field calculation codes will be tested in terms of their qualifications for magnetoplasmadynamic thrusters.

References

[1] Hügel, H., Zur Strömung kompressibler Plasmen im Eigenfeld von Lichtbogenentladungen, DLR-FB-70-13, 1970. Publishing Co.: Wiss. Berichtswesen der DFVLR, Postfach 906058, D-5000 Köln 90

[2] King, D.Q., Magnetoplasmadynamic Channel Flow for Design of Coaxial MPD Thrusters, Ph.D. thesis, Department of Mechanical and Aerospace Engineering, Princeton University, 1981; also available as MAE Report 1552

[3] Hügel, H., Zur Funktionsweise der Anode im Eigenfeldbeschleuniger, DFVLR-Report, DFVLR-FB 80-20, 1980. Publishing Co.: Wiss. Berichtswesen der DFVLR, Postfach 906058, D-5000 Köln 90

[4] Minakuchi, H. and Kuriki, K., Magnetoplasmadynamic Analysis of Plasma Acceleration, 17th International Electric Propulsion Conference, IEPC 84-06, Tokyo 1984

[5] Kimura, I., Toki, K. and Tanaka, M., Current Distribution on the Electrodes of MPD Arcjets, AIAA Journal, Vol. 20, No. 7, P. 889, 1982

[6] Lawless, J.L. and Subramaniam, V.V., A Theory of Onset in MPD-Thrusters, AFOSR-Report 83-0033, 1983

[7] Heimerdinger, D., An Approximate Two-Dimensional Analysis of an MPD Thruster, SSL 9-84, MIT, Cambridge, Mass., June 1984

[8] Schrade, H.O., Auweter-Kurtz, M. and Kurtz, H.L., Basic Processes of Plasma Propulsion, Final Scientific Report, AFOSR 82-0298, January 1987

[9] Isselhorst, A., Berechnung des Expansionsvorgangs in einem Plasmatriebwerk unter Berücksichtigung der elektromagnetischen Kompression, Diplomarbeit, IRS, Universität Stuttgart, IRS-87-S5, 1987

[10] Kurtz, H.L., Auweter-Kurtz, M., Merke, W.D., Schrade, H.O., Experimental MPD Thruster Investigations, AIAA 87-1019, 19th International Electrical Propulsion Conference, Colorado Springs, 1987

[11] Sleziona, P.C., Instationäre Berechnung der elektrischen Stromkontourlinien und des Strömungsfeldes im zylindrischen MPD-Triebwerk, Diplomarbeit, IRS, Universität Stuttgart, IRS-86-S7, 1986

[12] Jacobi, H., Entwicklung eines theoretischen Modells zur Beschreibung der Wechselwirkung zwischen elektrischer Entladung und Überschallströmung eines gepulsten CO-Lasers, DFVLR-FB 84-45, 1984. Publishing Co.: Wiss. Berichtswesen der DFVLR, Postfach 906058, D-5000 Köln 90

[13] Maecker, H., Plasmaströmungen in Lichtbögen infolge eigenmagnetischer Kompression, Zeitschrift für Physik, Bd. 141, pp. 198-216, 1955

7. Acknowledgements

FILMED
58